Investigations of the long term variability of black hole binaries

Untersuchung der Langzeitvariabilität von Doppelsternsystemen mit schwarzen Löchern

Der Naturwissenschaftlichen Fakultät
der Friedrich-Alexander-Universität
Erlangen-Nürnberg

zur

Erlangung des Doktorgrades Dr. rer. nat.

vorgelegt von

Victoria Grinberg

aus Chishinau

Tag der mündlichen Prüfung:

Vorsitzernder der Promotionskomission:	Prof. Dr. J. Barth
Erstberichterstatter:	Prof. Dr. J. Wilms
Zweitberichterstatter:	

Zusammenfassung

Diese Arbeit beschäftigt sich mit der Variabilität von Röntgendoppelsternen mit einem schwarzen Loch als kompaktem Begleiter, also Doppelsternen, in welchen der ursprünglich massereichere Stern auf der letzten Stufe seiner Entwicklung angelangt ist. Durch Sternwinde oder aufgrund der Vergrößerung des Volumens des Begleitestern in späten Phasen der Sternentwicklung kann es dabei zu Akkretion von Materie auf das schwarze Loch kommen, in deren Folge hochenergetische Straglung freigesetzt wird. Das tiefe Gravitationspotential des schwarzen Lochs und die hohen Temperaturen des Plasmas, das akkretiert wird, resultieren in einem komplexen Zusammenspiel quantenmechnischer und relativistischer Effekte, das durch die Anwesenheit von Magnetfeldern zusätzlich verkompliziert wird und bis heute nur in Ansätzen verstanden ist.

Typische Kombinationen beobachteter spektraler und Zeitreiheneigenschaften solcher Objekte werden als Zustände (vor allem weicher, harter und Zwischenzustand) bezeichnet und entsprechen wahrscheinlich verschiedenen Anordnungen von Akkretions- und Auswurfströmen, also von Akkretionsscheibe, Korona, Akkretionsscheibenwinden und Jets. In der vorliegenden Arbeit wird ein empirischer Ansatz gewählt, um die Langzeitänderungen verschiedener Parameter zu klassifizieren, die die spektralen und Zeitreiheneigenschaften der Quellen beschreiben, und um so eine Grundlage für den Vergleich mit theoretischen Modellen zu schaffen. Der Schwerpunkt liegt dabei auf den Unterschieden zwischen den Zuständen und auf der Beschreibung der Zustandsübergänge.

Nach einer Darstellung des heutigen Wissensstandes und besonders der Vielzahl der offenen Fragen, werden ein Überblick über die verwendeten Instrumente (verschiedene Teleskope auf den Satelliten RXTE, INTEGRAL, Swift und Fermi und auf der international Weltraumstation ISS, sowie das Ryle/AMI Radio Teleskop) sowie eine Einleitung in die verwendeten Analyseverfahren, vor allem Verfahren der Zeitreihenanalyse im Fourierraum, gegeben. Es folgt die Analyse einzelner Beobachtungen der Röntgendoppelsterne Cygnus X-1 und H1743−322, die als Beispiel dafür dient, wie Zustände und Zustandsübergänge anhand von spektralen und Zeitreiheneigenschaften klassifiziert werden.

Der erste Schritt in der Unterschunung der Langzeitvariabilität ist die spektrale Analyse von Cygnus X-1 über die gesamten 16 Jahre (1996–2011) der Lebenszeit des RXTE-Satelliten. Bekannten Korrelationen zwischen Bestandteilen einfacher Modelle für die Spektralform werden mit weit besserer Abdeckung verschiedener Quellenzustände als zuvor bestätigt. Bei der Untersuchung des Sternwindes des normalen Begleiters des schwarten Lochs, also des blauen O-Riesen HDE 226868, fungieren das schwarze Loch und die in seiner unmittelbarer Nähe erzeugte Röntgenstrahlung als Sonde für den Wind. Es wird qualitativ gezeigt, dass die beobachtete orbitale Modulation des Windes mit Modellen eines stark geklumpten Windes, das zum schwarzen Loch hin fokussiert ist, in Übereinstimmung ist.

Hierauf schließt sich die statistische Analyse von Beobachtung von Cygnus X-1 mit Himmelsmonitoren im Röntgenbereich, die insgesamt einen Zeitraum von 17 Jahren umfassen, in welchen die Quelle zahlreiche Zustandsübergänge sowie Phasen verschiedener Aktivität gezeigt hat. Dafür wird auf der Grundlage einzelnen höher aufgelöster Beobachtungen mit den RXTE-PCA und RXTE-HEXTE Instrumenten ein Zustandsklassifizierungsschema für niedrig aufgelöste aber sehr häufige Beobachtungen mit Himmelsmonitoren entwickelt. Dieses Schema erlaubt die Analyse von Zuständen und Zustandsübergängen mit einer Zeitauflösung von unter einem Tag über den gesamten 17-jährigen Zeitraum und zeigt, dass der Zwischenzustand viel weniger stabil ist als harte und weiche Zustände. Die detaillierte Darstellung der Entwicklungsschritte der Zustandsklassifikation bietet zudem eine Vorlage für ähnliche Vorgehensweise für andere Quellen und Quellenarten.

Weiter werden Anwendungen dieser Zustandsklassifikation als Hilfsmittel für höchstaufgelösten Beobachtungen im weichen Röntgenbereich und als Grundlage für zustandsaufgelöste Polarisationsanalyse von Gammastrahlung beleuchtet. So ist zum Beispiel die Zuordnung von XMM Beobachtungen dem Zwischenzustand entscheidend für die Interpretation der spektroskopischen Besonderheiten der Beobachtungen.

Die hohe Zeitauflösung der RXTE-PCA Beobachtungen von 2 ms ermöglicht im nächsten Schritt eine Zeitreihenanalyse von über 1900 einzelnen im Schnitt dreißigminütigen Beobachtungen von Cygnus X-1, die insgesamt einen Zeitraum von über 13 Jahren umspannen. Dabei werden klare Zusammenhänge zwischen der spektralen Form der Quelle und den Fouriergrößen (den Periodogrammen sowie den Zeitverzögerungen und der Kohärenzfunktion), eine Abhängigkeit der Form der Periodogramme von dem betrachteten Energieband, sowie Korrelationen zwischen den Strukturen in den Periodogrammen und in den frequenzabhängigen Zeitverzögerungen und der Kohärenzfunktion gezeigt. Die Ergebnisse sind ein klarer Hinweis, dass die maßgebliche Kurzzeitvariabilität in verschiedenen Zuständen ihren Ursprung in verschiedenen Bestandteilen der Akkretions- und Ausstroßströme hat, und dass keines der heutigen theoretischen Modelle, die sich zum Teil stark in der Grundnanahmen, z.B. dem Ursprung der Röntgenstrahlung in der Korona oder in Jets, unterscheiden, alle Parameter und ihre Wechselwirkung erklären kann.

Insgesamt zeigt diese Arbeit die Wichtigkeit von systematischen Langzeitanalysen auf, die viele Fragen beantworten können, an denen die Untersuchung einzelner Beobachtungen, auch hoher Qualität, scheitern, wenn der Kontext der Beobachtung nicht berücksichtigt wird. Die hier entwickelten Methoden und Darstellungsformen können leicht auf anderen Quellen übertragen werden, während die vorgestellten Ergebnisse für den Fall von Cygnus X-1 starke Bedingungen an physikalische Modelle für die Akkretions- und Ausstoßströme stellen und die Wichtigkeit einer möglichst modellunabhängigen Herangehensweise betonen, die vor einer Überinterpretation einzelner Beobachtungen außerhalb des Langzeitzusammenhangs schützt.

Abstract

This work considers the variability of X-ray binaries with black holes as the compact objects, i.e., binaries, where the originally more massive star has reached the final stage of its evolution. Matter can be accreted onto the black hole either through stellar winds of because of the increasing volume of the companion in the late stages of stellar evolution, and lead to high energy emission. The deep gravitational well of the black hole and the high temperatures of the accreted plasma results in a complex interplay of quantum mechanical and general relativistic effects that are further complicated by the presence of magnetic fields and, until today, hardly understood.

Typical combinations of observed spectral and timing characteristics of such objects are called states (mainly soft, hard and intermediate states) and likely correspond to different configurations of accretion and ejection flows, i.e., accretion disk, corona, accretion disk winds and jets. In the presented work we choose an empirical approach to classify the long term changes of different parameters that describe spectral and timing features of the source and to create a basis for comparison with theoretical models. The emphasis is on the differences between the states and on the description of state transitions.

After presenting the state of knowledge and especially the multitude of open questions of black hole binary research, we give and overview over the instrumentation we used (telescopes on board the satellites RXTE, INTEGRAL, Swift and Fermi and on the International Space Station ISS, as well as the Ryle/AMI radio telescope) and an introduction to the analysis techniques, especially the Fourier-bases timing analysis. We follow with an analysis of individual observations of the black hole binaries Cygnus X-1 and H1743−322 that serves as an example for how states and state transitions are classified based on spectral and timing features.

The first step in the investigation of the long term variability is the spectral analysis of Cygnus X-1 over the whole 16 years (1996-2011) of the RXTE lifetime. Known correlations between the parameters of simple models for the spectral shape are confirmed with a much better coverage of different source states than previously. The black hole and the X-ray radiation created in its immediate surroundings serve as a probe for the investigation of the stellar wind of the normal companion of the black hole, the O-type super giant HDE 226868. We show qualitatively that the observed orbital modulation of the wind is consistent with models of a clumpy stellar wind focused towards the black hole.

We continue with a statistical analysis of Cygnus X-1 observations with X-ray all sky monitors that span a total of 17 years, in which the source has shown numerous state transitions and periods of different activity. For this purpose, we develop a classification scheme for low spectral resolution but high cadence observations with all sky monitors that is based of higher resolved but much more infrequent observations with RXTE-PCA and RXTE-HEXTE. This scheme allows us to analyze states and state transition with a time resolution below a day over the whole 17 years and shows that the transitional state is much less stable than the hard and soft states. The detailed display of the development of this state classification offers a stepping stone for similar approaches for other sources and source types.

We highlight applications of this classifications as additional resources in high resolution observations in soft X-rays and as a basis for state-resolved polarization analysis in the γ-rays. Attributing XMM observations to the intermediate state is, for example, crucial for the interpretations of spectroscopic peculiarities of these observations.

The 2 ms high time resolution of RXTE-PCA allows us to take the next step and conduct a timing analysis of over 1900 individual, on average thirty minutes long, observations of Cygnus X-1 that span a total of over 13 years. We can show the presence of clear relationships between the spectral shape of the source and Fourier-based quantities (power spectra, time lags and coherence function), a dependency of the shape of the power spectra on the considered energy band and correlations between structures in the power spectra and in the frequency-dependent time lags and coherence function. These results imply that the dominant short term variability in the different states originates in different parts of the accretion and ejection flows and that none of today's models, which partly strongly differ in their basic assumptions, e.g., in the source of the X-ray emission in corona or in the jets, can explain all parameters and their interplay.

This work shows the importance of long-term analyses that can answer questions that single observations, even if they are of high quality, fail to answer if the context of the observations is not taken into account. The methods developed in this thesis can be easily transferred to other source, while the presented results for the case of Cyg X-1 put strong constraints on physical models of accretion and ejection flows and emphasize the significance of model-independent approaches, which guard from an overinterpretation of individual observations outside of their long-term context.

Contents

> Only kings, presidents, editors, and people with tapeworms have the right to use the editorial 'we'.[1]
>
> *(Mark Twain)*

1 Introduction

BLACK HOLES are perhaps the most mind-boggling objects ever conceived by physicists – at least among the actually observed objects, as there are, of course, yet purely theoretical concepts such as the multiverse (Tegmark, 2007, *not* the one of Moorcock et al. 1999).

They are basic for the evolution and the very working of our universe.[2] To name just two examples: radiation from accreting black holes could have strongly contributed to the re-ionization of the universe (Mirabel et al., 2011), and active galactic nuclei (AGN; accreting black holes in the centers of galaxies) are key ingredients in galaxy evolution, as obvious from the tight correlation between the black hole mass and velocity dispersion in the bulges of galaxies (Gebhardt et al., 2000; Ferrarese & Merritt, 2000). Notwithstanding their importance, black holes are simple objects: they are characterized by mass and angular momentum only (and charge, which, however, is not important for astrophysical black holes)[3] and all they can do is to convert gravitational energy into radiation and kinetic energy that are then fed back into the surroundings (Fender, 2010). Yet, we are far from understanding this seemingly simple process that, once scrutinized, involves complex questions from (almost) all areas of physics, from quantum mechanics to general relativity, from atomic physics to magnetohydrodynamics.

A starting point for everything black hole related is the nicely compiled (although not all-encompassing, which would be impossible) reference list of Gallo & Marolf (2009).

---

[1] In spite of this very true statement of Mark Twain's, this is exactly what I will be doing throughout this thesis, which is for the greatest part based on published scientific papers, where 'we' is the usual pronoun of choice. Using 'we' everywhere else is then only consistent. Whether the reader interprets it as a *pluralis majestatis* or as an inviting 'we – you and I, my dear reader' is entirely her own choice.

[2] Although, unfortunately, fun ways to use black holes – comparable to the use of Cepheids as a Galactic Internet (Learned et al., 2008) or of pulsars as a interstellar GPS (Becker et al., 2013) – are yet lacking to our knowledge.

[3] While the name 'no hair theorem' was clearly coined by John Archibald Wheeler, tracing the very first publication theoretically establishing this idea is not easy, see Israel (1967, 1968), Carter (1971), and Hawking (1972).

In this work, we concentrate on galactic black hole binaries (BHBs), i.e., black holes in binary systems with a 'normal' star that has not yet reached a stadium when the burning processes in its core stopped. The high X-ray flux of these objects enables us to detect clear signals in the spectral, timing and polarization domains. This thesis mainly concerns itself with the X-ray spectral and timing studies of the BHB Cygnus X-1 (Cyg X-1) and maps a pathway towards more detailed polarization studies in the γ-rays than possible to date.

1.1 Black hole binaries

Up to this date, there are $\sim$20 confirmed black holes binaries, i.e., binary systems with a compact object where the mass of the compact objects is larger than the $\sim$2–$3M_\odot$ of the Oppenheimer-Volkoff mass limit for neutron stars (Tolman, 1939; Oppenheimer & Volkoff, 1939), with even more good candidates (McClintock & Remillard, 2006). The total number of stellar mass black holes in our galaxy is, however, estimated to be $> 10^8$ (Shapiro & Teukolsky, 1983), i.e., $\sim$35000 within the closest 250 pc (Fender et al., 2013).

Stellar evolution and its remnants are treated in detail in any introductory book into astrophysics, e.g., Carroll & Ostlie (2007), to name a personal favorite. Postnov & Yungelson (2006) give a detailed introduction into the formation and evolution of compact binary systems containing compact objects (white dwarfs, neutron stars, or black holes).

In general three different modes of mass transfer are possible in X-ray binaries:

- in *high mass X-ray binaries* (HMXBs), accretion onto the compact disk feeds from the stellar wind of an early type (and thus high mass) companion star;
- in *low mass X-ray binaries* (LMXBs), matter from a late type companion that has filled its Roche lobe (Roche, 1849, 1850, 1851) can spill over the Lagrange point L_1 (Lagrange, 1772) towards the compact object;
- in *Be-binaries*, the compact object moves on an eccentric object around a fast rotation Be-star with an equatorial disk and accretes material when passing through or close by the disk (for a review on Be-binaries, which, so far, interstingly all contain neutron stars, see Coe, 2000).

In all cases, the observed radiation – the bulk of it in X-rays – arises from a complex interplay of accretion and ejection processes. In case of white dwarfs and neutron stars, the surface of the compact object and its magnetic field complicate the situation. But even in the comparatively simple case of black holes, we are lacking solid empirical and theoretical understanding of the inflows and outflows in these systems. The aim of this thesis is to shed light on some of the observational signatures of these processes and their interconnection.

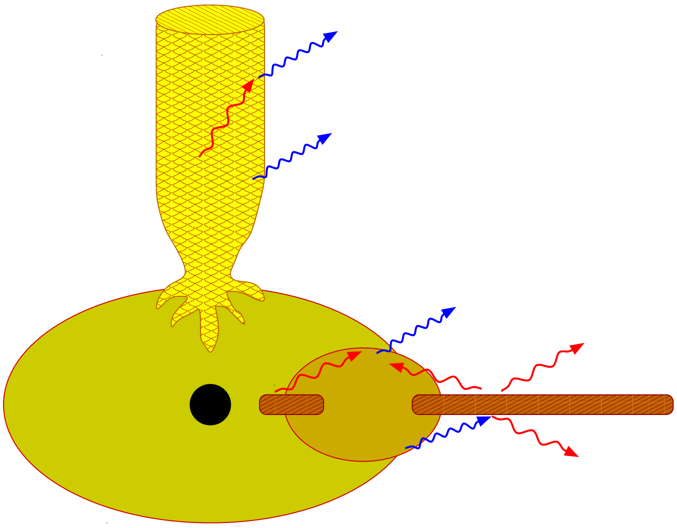

Figure 1.1: 'Toy' sketch of the possible X-ray emission geometry in the hard state: the contribution can come from the accretion disk (possibly truncated, shown in brown), a corona (two geometries are shown: quasi-spherical in lighter yellow and torus in darker yellow), and/or a jet, which can contribute to the X-ray through synchrotron self-Compton and synchrotron emission. Reflection and fluorescent line components arise from reprocessed hard X-rays. Figure from Nowak et al. (2011).

1.2 X-ray emission geometry

We assume that the reader is familiar with the physics of radiation processes (see the book by Rybicki & Lightman, 1979 for the full theory and, e.g., the lecture by Wilms, 2012a for an advanced level introduction) and accretion theory (see Frank et al., 2002) and will therefore rather concentrate on the open questions in the vast and ever-expanding literature on accretion and ejection processes in BHBs than on the basic principles.

Two different X-ray spectral states have been first recognized in Cyg X-1 by Tananbaum et al. (1972). Coe et al. (1976) discovered the same pattern in the transient black hole candidate A0620–00: a 'low' (modern terminology following Fender et al. 2004, 2009 and Belloni 2010, see also Sect. 1.3: *hard*) state with a power law like spectrum and a 'high' (modern terminology: *soft*) state with a more complex spectral shape, later shown to be dominated by the thermal emission of an accretion disk.[4,5] Subsequently, a 'very high state' with intermediate spectral and distinct timing properties was observed (Miyamoto et al., 1991; Kitamoto et al., 1992). The hard state corresponds to times of radio detections of the respective sources, while in the soft state the radio emission is strongly quenched (e.g., Fender et al., 2004, 2009). Together, the different spectral shapes and radio properties that seem common to all BHBs[6] point towards strong changes in the emitting components. The exact behavior of the accretion and ejection flows is a – perhaps even *the* – key question of current BHB research.

---

[4] But see (McClintock & Remillard, 2006) for an alternative terminilogy.

[5] Example spectra for Cyg X-1 are shown on Fig. 4.6 on p. 38.

[6] Even for the perhaps most complex case, GRS 1915 + 105, Rodriguez et al. (2008a,b) conclude that its behavior is compatible with the common behavior shown by other sources as summarized by Fender et al. (2004) and presented here in Sect. 1.3.

The flat to inverted radio (to mm) spectra are associated with synchrotron emission from the jets (see Fender, 2006, and Gallo, 2010, for reviews on jets from BHBs). The disk component is usually assumed to be the standard geometrically thin, optically thick accretion disk of Shakura & Sunyaev (1973)[7] – for more details see the recent overview of theory of black hole accretion flows by Blaes (2013), who discusses radiatively efficient and inefficient models using the α-prescription for turbulence of Shakura & Sunyaev (1973) and the probable origin of this turbulence in magnetorotational instability (MRI; Balbus & Hawley, 1991, 1992; Hawley & Balbus, 1991, 1992). The cut off power law emission component is attributed to Comptonization of lower energy electrons, either in a Comptonization corona or in the base of the jet. Synchrotron emission from the jet may contribute to the X-rays, especially in the hard state (Markoff et al., 2005; Maitra et al., 2009). Reprocessing leads to signatures such as reflection components and fluorescence lines. Additionally, recent results point towards the importance of disk winds in the soft states, detected as highly ionized, often blue-shifted absorbers (see the extensive references list by Neilsen, 2013); such disks are ubiquitous and their mass loss rate can be comparable to the accretion rate. Figure 1.1 sketches a possible X-ray emission geometry in the hard state (see Nowak et al., 2011).

The corona is a region of hot plasma above or within a cooler accretion flow (it was actually dubbed 'two-phase accretion disk model' by Haardt & Maraschi, 1991) close to the black hole, where photons are up-scattered by inverse Compton scattering. The geometry and the nature of the corona are highly debated. Examples of unsolved questions include (see also Nowak et al., 2011; Nowak et al., 2012): Does the corona overlay the accretion disk (e.g., Beloborodov, 1999) or is the disk truncated with the corona in the middle (e.g., Dove et al., 1997), perhaps taking the shape of a multizone hot disk (Veledina et al., 2013)? Or is perhaps a simple slab geometry (Malzac & Jourdain, 2000) the right approach if properly treated? Is the distribution of the electrons in the corona purely thermal (Poutanen & Vurm, 2009) or is there a fraction of non-thermal electrons (Ibragimov et al., 2005)? Or are multi-flow geometries such as the jed emitting disk (Ferreira et al., 2006; Petrucci et al., 2010) the right approach? Additionally, as Markoff (2010) remarks, the inner regions of the accretion flow are threaded by strong magnetic fields that have to be – and in some of the newer models are – taken into account. The step from such magnetized coronae to the inner parts of the jets, e.g., the jet base subsuming the role of the corona as suggested in Markoff et al. (2005), may then be only a small one.

Jets in hard state BHBs are powerful and carry away a significant fraction of accretion luminosity (Fender, 2001, whose sample includes Cyg X-1), although whether and how much they contribute to the X-ray emission is highly debated, in spite of the recent cues towards the jet origin of emission above 400 keV (Laurent et al., 2011b; Jourdain et al., 2012, both for the case of Cyg X-1). The existence of a connection between jets and X-ray emission can be inferred from the so-called fundamental plane of the radio/X-ray correlation that connects hard state BHBs and AGN and that was independently found by Merloni et al. (2003) and Falcke et al. (2004, see Merloni et al., 2006 for both original groups addressing some of the criticism of the discovery, but also Fender et al., 2010 and

---

[7] While the possible importance of the jets for BHBs has only entered most of the literature comparatively recently, jet-like outflows have already been shown on Fig. 9 of this seminal paper!

Coriat et al., 2011 for evidence of two tracks for the correlation). Two main groups of models are proposed for powering jets: in the Blandford-Znajek mechanism (Blandford & Znajek, 1977) the rotational energy of spinning black hole is extracted in a region within ~100 gravitational radii, which is strongly affected by frame-dragging. In the mechanism of Blandford & Payne (1982) the disk and its magnetic field are the only origin for all energy and rotation. Some observational evidence against the spin-powered mechanism in BHBs exist (Fender et al., 2010; Russell et al., 2013a), but what launches, accelerates, and collimates the jets in all their complexity remains a mystery. Markoff (2010) gives an overview of some models, but points out that an exhaustive review is hardly possible given the large number of publications. Generally, today's most fundamental models – whether they follow the jet or the corona paradigm or whether they try to reconcile them – are simulations that require complex (magneto)hydrodynamic codes (e.g., McKinney, 2006; McKinney & Blandford, 2009; Fragile & Meier, 2009; Fragile, 2013, and many others) and cannot yet be directly compared with data.[8]

1.3 State transitions and the q-track

Over the years, different empirical classification have been proposed for states of BHBs (McClintock & Remillard, 2006; Fender et al., 2004, 2009, see also review by Belloni, 2010). Here, we concentrate on the most recent one that represents the current stand of the *phenomenological* understanding of BHBs. It attempts to find a simple, unified pattern and seems the most promising approach to solve the accretion/ejection puzzle, in spite of the yet missing puzzle pieces.

The behavior of BHBs can be well characterized in terms of a hardness-intensity diagram (HID). The hardness is most often represented as the quotient between the count rate in a higher energy band and the count rate in a lower energy band. The intensity is usually the total count rate from a certain instrument or in a certain wide energy band.[9] A direct physical interpretation of the hardness is non-trivial. Does, e.g., a decreasing hardness mean a steeper power law or a stronger disk or a combination of both? Still, a careful choice of the energy bands and a comparison to the results of spectral analysis allow to infer some general behavior of the emission regions from the position and movement of the source in the HID.

The middle panel of Fig. 1.2 shows the typical behavior of a transient BHB in outburst: it follows a q-shaped track on the HID (also known as turtle-head diagram). Each spectral state corresponds to a distinct position on the track, with distinct timing and radio behavior (for a more detailed review, that does not, however, cover cross-spectral quantities such as coherence and lags, see Belloni, 2010):

---

[8] The only current jet-model allowing a comparison with data in the detector space that we are aware of is Sera Markoff's `agnjet` model (Markoff et al., 2005; Maitra et al., 2009, see also Grinberg, 2010).

[9] See also Figs. 5.5, 5.7, and 5.9 (p. 54, p. 58, and p. 60) for example HIDs for Cyg X-1 with RXTE-ASM, MAXI, and Fermi-GBM, respectively.

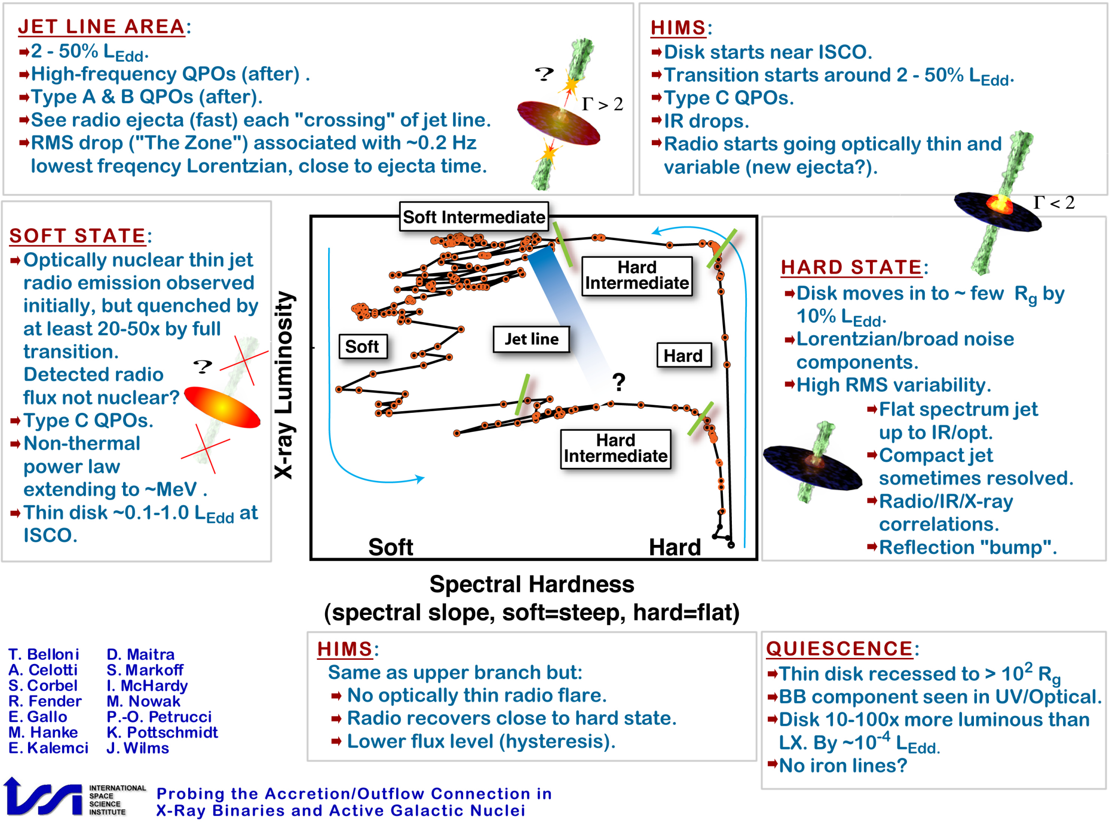

JET LINE AREA:
- 2 - 50% L_{Edd}.
- High-frequency QPOs (after) .
- Type A & B QPOs (after).
- See radio ejecta (fast) each "crossing" of jet line.
- RMS drop ("The Zone") associated with ~0.2 Hz lowest freqency Lorentzian, close to ejecta time.

HIMS:
- Disk starts near ISCO.
- Transition starts around 2 - 50% L_{Edd}.
- Type C QPOs.
- IR drops.
- Radio starts going optically thin and variable (new ejecta?).

SOFT STATE:
- Optically nuclear thin jet radio emission observed initially, but quenched by at least 20-50x by full transition. Detected radio flux not nuclear?
- Type C QPOs.
- Non-thermal power law extending to ~MeV .
- Thin disk ~0.1-1.0 L_{Edd} at ISCO.

HARD STATE:
- Disk moves in to ~ few R_g by 10% L_{Edd}.
- Lorentzian/broad noise components.
- High RMS variability.
  - Flat spectrum jet up to IR/opt.
  - Compact jet sometimes resolved.
  - Radio/IR/X-ray correlations.
  - Reflection "bump".

T. Belloni
A. Celotti
S. Corbel
R. Fender
E. Gallo
M. Hanke
E. Kalemci
D. Maitra
S. Markoff
I. McHardy
M. Nowak
P.-O. Petrucci
K. Pottschmidt
J. Wilms

HIMS:
Same as upper branch but:
- No optically thin radio flare.
- Radio recovers close to hard state.
- Lower flux level (hysteresis).

QUIESCENCE:
- Thin disk recessed to > 10^2 R_g
- BB component seen in UV/Optical.
- Disk 10-100x more luminous than LX. By ~10^{-4} L_{Edd}.
- No iron lines?

Probing the Accretion/Outflow Connection in X-Ray Binaries and Active Galactic Nuclei

Figure 1.2: Summary plot for the current understanding of the q-track as of January 2008; Figure from `http://www.sternwarte.uni-erlangen.de/proaccretion/`.

- starting from *quiescence*, the source enters the *hard state*. As it evolves, it becomes brighter at roughly constant, high hardness. Radio emission is detected. X-ray timing analysis reveals broad noise components. The fractional root mean square (rms) variability is high at ~30–50%. The X-ray time lags are low (e.g., Pottschmidt et al., 2003; Muñoz-Darias et al., 2010) and the coherence is high (see Sect. 7.1.3 for a definitions of X-ray time lags and coherence);
- when the source begins to soften at a roughly constant luminosity, it enters the *intermediate state*, which is further divided into *hard intermediate* and *soft intermediate* states. Radio emission will often show flares. The broad noise components move to higher frequencies and the X-ray time lags increase. The transition between hard intermediate and soft intermediate state is associated with a strong drop in fractional rms variability and may be associated with the so-called jet-line which marks the point where the jet is switched off, although the observational evidence is yet unconclusive (Fender et al., 2009);
- the softest spectra correspond to the *soft state*. The radio emission is strongly quenched or absent. The broad noise components disappear and make space for a power law-like component. The fractional rms is low and the time lags return to

lower values (Pottschmidt et al., 2000);

- the source returns to the quiescence through the same states in reverse order, although generally at lower luminosities, i.e., it shows a hysteresis.

Deviations from this behavior are still consistent within the model: some sources will never enter the soft or even the intermediate state in their outburst (e.g., Swift J174510.8–262411, Tomsick et al., 2012; Belloni et al., 2012; Russell et al., 2013b). The persistent source Cyg X-1 does not show hysteresis between the hard-to-soft and soft-to-hard transitions – however, Cyg X-1 only covers a small range of bolometric luminosities (Cui et al., 1997; Shaposhnikov & Titarchuk, 2006; Wilms et al., 2006, and references therein) and GX 339–4, the canonical q-track source, shows strong dependency of the distance between the two branches on the total luminosity of the outburst. Doubt has been cast on the possible truncation of the accretion disk in the hard and intermediate states, as introduced on Fig. 1.2 – there is observational and theoretical support for the idea that the disk may extend to the innermost stable circular orbit (ISCO) even at very low luminosities (Gallo, 2010, and references therein).

While not originally part of the q-track picture, disk winds have been shown to be ubiquitous in the jet-free soft states (Ponti et al., 2012), i.e. mainly on the soft vertical branch of the HID, although note that they can only be observed in high-inclination systems due to geometrical effects.

The greatest success of the q-track concept is its transferability to other types of systems where accretion/ejection coupling plays a major role, e.g., neutron stars and cataclysmic variables (Körding et al., 2008) and AGN (Körding et al., 2006)[10]. Because of the different mass scales and depths of the potential wells of these objects, the HID has to be transformed into so-called disk-fraction/luminosity diagrams (DFLD; Körding et al., 2006, see also Dunn et al., 2010 for the application of DFLDs to BHBs). That cataclysmic variables, which contain a white dwarf as a compact object, show qualitatively the same behavior as black hole and neutron star binaries, especially the presence of transient jets during eruption, implies that basics of states and jet formation do neither require unique properties of black holes (e.g., the non-existence of a surface) nor the very deep potential well of black holes and neutron stars.

1.4 An example BHB: Cygnus X-1

The high mass X-ray binary Cyg X-1 is one of the prime targets of BHB research – with over 1200 bibliographical entries on ADS[11] with 'Cyg X-1' in the title, an exhaustive review is inexpedient. We therefore give basic information, intended to allow the reader to familiarize herself with the source.

---

[10] The variability time scales are roughly proportional to mass and are therefore $\sim 10^5$–10^8 times larger in AGN than in BHBs, so that AGN can only be analyzed as a sample. The results does not necessarily imply that AGN follow the q-track, but only that the AGN, if they find themselves in a particular state, show similar jet properties to BHBs in the same state (Fender, 2010).

[11] `http://adsabs.harvard.edu/abstract_service.html`

Cyg X-1 was discovered in X-rays 1964 during a balloon flight (Bowyer et al., 1965). Murdin & Webster (1971) and Bolton (1972) independently identified the source in the optical with HDE 226868, an O9.7 Iab supergiant (Walborn, 1973). In radio, Hjellming & Wade (1971) reported upper limits of 5 mJy before and a flux of 0.015 mJy in May 1971, coincident with X-ray source detected independently by Tananbaum et al. (1971, using UHURU) and Rappaport et al. (1971, using a rocket borne experiment). Tananbaum et al. (1972) recognized the first distinct spectral states with the UHURU satellite. But it was not until a decade later that Gies & Bolton (1982) dynamically constrained the compact object to be a black hole.

The distance to Cyg X-1 ranges from 1.8 to 2.4 kpc in literature (Ziółkowski, 2005, and references therein), with the recent, most exact values of $1.86^{+0.12}_{-0.11}$ kpc obtained from trigonometric parallax using the Very Long Baseline Array (Reid et al., 2011), which is in agreement with the work of Xiang et al. (2011), who study the X-ray dust scattering halo in Cyg X-1 and obtain a distance of 1.81 ± 0.09 kpc. Using this distance, Orosz et al. (2011) find a black hole mass of $M = 14.8 \pm 1.0 M_\odot$ and an inclination of $i = 27.1^\circ \pm 0.8^\circ$.[12]

The black hole is close to being a Kerr black hole (maximal spin, $a \approx 1$, Kerr, 1963), with a independently determined by Duro et al. (2011, 2013) from the shape of the Fe Kα-line using the sophisticated `relline`-model of Dauser et al. (2010), by Gou et al. (2011) from modeling the thermal continuum spectrum, and by Fabian et al. (2012) by fitting reflection models to broadband Suzaku data.

The orbital period of the source is $P = 5.599829$ days (Brocksopp et al., 1999b; Gies et al., 2003, 2008) and has been detected across the spectral domain, e.g., in X-rays, radio (Pooley et al., 1999, who find that the minimum of the radio is delayed by ~16 h at 15 GHz compared to the X-rays), Hα (Ninkov et al., 1987), etc. Additionally, the source shows a super orbital period of ~150 d (Brocksopp et al., 1999a; Benlloch et al., 2004; Poutanen et al., 2008) that seems, however, to have doubled recently (Zdziarski et al., 2011a, but see, e.g., Priedhorsky et al. 1983 for the evidence of a similar ~300 d long period before 1980).

With $\sim 10^{-6}\,M_\odot\,\mathrm{year}^{-1}$, the mass loss of HDE 226868 is high (Herrero et al., 1995) and the accretion on the compact object feeds from this wind. Such winds are driven by copious absorption lines in UV (Castor et al., 1975) and are generally clumpy (Oskinova et al., 2012; Sundqvist & Owocki, 2013, and references therein). However, HDE 226868 is close to filling its Roche lobe (Conti, 1978; Gies & Bolton, 1986a,b), so the wind is strongly focused towards the black hole (Friend & Castor, 1982). Consistently with this scenario, the absorption in optical band is strongest at superior conjunction, i.e., at $\phi_\mathrm{orb} = 0$ (Gies et al., 2003). So are X-ray dips, i.e., strong absorption episodes in the X-rays, most likely due to clumps (Bałucińska-Church et al., 2000; Poutanen et al., 2008; Boroson & Vrtilek, 2010; Miškovičová et al., 2013).

Because of the focused wind, the accretion is not simple Bondi & Hoyle accretion (Bondi & Hoyle, 1944; Bondi, 1952), but an accretion disk is present. Evidence for the disk comes from the direct spectral signatures in the soft X-rays and the presence of the Fe Kα

---

[12] Although note, that other, less well constrained values, are still used even in later publications, e.g., 50° in Del Santo et al. (2013).

line in the spectrum (Miller et al., 2002; Nowak et al., 2011; Duro et al., 2011, 2013).

Extended radio emission from Cyg X-1 on milli-arcsecond scales, i.e., an actual radio imaging of the compact jet, has been reported by Stirling et al. (2001) for a hard state period. Rushton et al. (2012) present evidence for the presence of a weak compact jet in the soft state of Cyg X-1, however they note that the source may not have entered a full soft state during their observations. Jets in the hard and hard-intermediate state have been spectroscopically detected in mid-IR by Rahoui et al. (2011) who, remarkably, also for a first measure the jet break time in a BHB during one of their hard state observations spectroscopically. On the much larger scale of arcminutes, Gallo et al. (2005) report on a ring-like structure[13] at 1.4 GHz with a diameter of ∼5 pc. They conclude that the structure was inflated by the inner radio jet and estimate that to do so the jet has to have a kinetic power of the order of the X-ray luminosity of the object.

1.5 Plan of thesis

The rest of this thesis is organized as follows: In Chapter 2, we discuss the instruments and some the less widely-known analysis techniques used in this work, namely Fourier-based X-ray timing analysis. In Chapter 3, we present results from near real time monitoring of black hole binaries with pointed observations of the RXTE and INTEGRAL satellites, with an emphasis on the elusive state transitions. In Chapter 5, we continue the analysis of the states and state transitions and develop a general methodology to classify states of Cyg X-1 using all sky monitors (RXTE-ASM, MAXI, Swift-BAT, and Fermi-GBM) and use it to quantify the long-term evolution of the source. In Chapter 6, we show this methodology in further use with a focus on polarization analysis with INTEGRAL, as well as individual observations with Chandra and XMM satellites. In Chapter 7, we use the unique RXTE observational campaign of Cyg X-1 to conduct a Fourier frequency- and energy-resolved analysis of X-ray timing parameters of the source at all spectral shapes in order to understand the link between spectal and timing characteristics and to put constraints on theoretical models for the accretion and ejection flows. In Chapter 4 we address the long-term spectral evolution of Cyg X-1 in more detail and with a focus on the orbital variability of the absoption and therefore the clumpy stellar wind of HDE 226868. We summarize our results and give an outlook on some future work in Chapter 8.

---

[13] The structure is also clearly visible in the optical band with, e.g., the Hα filter, with a short exposure, but remained curiously unrecognized prior to the work of Gallo et al. (2005).

Schlag mal auf das Gehäuse von oben drauf (ruhig kräftiger). Das hilft meistens.

(From the Remeis admin list. A response to a complaint about one of our computers.)

2 Instrumentation and data analysis

2.1 Instrumentation

An introduction to X-ray detectors and telescopes has been given elsewhere (Fürst, 2011; Wilms, 2012b; Zschornack, 2007; Trümper & Hasinger, 2008; Arnaud et al., 2011) and is out of the scope of this work. Still, we want to emphasize here that we can only be sure that our analysis is sound if we understand the idiosyncrasies of the instruments we employ – and only then can we push the boundaries of the science that can be done with these instruments.

In the following we give very short overview of the instruments used in this work: the ASM, PCA and HEXTE on board RXTE (Sect. 2.1.1), the IBIS on board INTEGRAL with a special focus on its polarimetric abilities (Sect. 2.1.2), the Swift-BAT (Sect. 2.1.3), MAXI (Sect. 2.1.4), and Fermi-GBM (Sect. 2.1.5) all sky monitors, and finally the Ryle/AMI (Sect. 2.1.6) radio telescope.[1]

2.1.1 RXTE

NASA's Rossi X-ray Timing Explorer (RXTE; Bradt et al., 1993, see also RXTE technical appendix[2]) was launched on 1995 December 30 and decommissioned on 2012 January 5. The satellite had an initial altitude of 580 km, an inclination of 23° and a period of about 100 min, with some altitude loss over the years. The satellite's main strength was the ability to conduct ultra-fast timing studies, complemented by a broadband spectral coverage with a modest spectral resolution in pointed observations and a long term all-sky monitoring in three energy bands. A good, concise overview of RXTE and its instruments

---

[1] The inclined reader may find it amusing that this whole extensive work has not used a single 'classical' telescope, i.e., one with mirrors (Wolter, 1952), but instead utilized instruments employing collimators, coded masks and the Earth occultation technique.

[2] `http://heasarc.gsfc.nasa.gov/docs/xte/appendix_f.html`

can be found in Kreykenbohm (2004).

Due to the spacecraft orbit, RXTE observations were affected by the South Atlantic Anomaly, a region with increased particle background (Fürst et al., 2009). The instruments were switched off during the passage and data taken directly after the passage can suffer from high instrumental background.

ASM

The three Shadow Scan Cameras (SSCs) of the All Sky Monitor (ASM; Levine et al., 1996) were one-dimensional coded masks on top of proportional counter detectors. The ASM scanned the sky in pre-planned dwells of ∼90 s exposure windows, so that each sky position was covered 5 to 10 times a day. ASM data are not analyzed by the individual user, but the light curves are publicly available at a dedicated website.[3] The three energy bands of the ASM cover roughly 0.5–3 keV (band A), 3–5 keV (band B), and 5–12 keV (band C). In early 2010, the ASM started to show strong signs of instrumental decline, possibly due to gain changes in the detectors (Sect. 5.1.1, see also Grinberg et al., 2013; Vrtilek & Boroson, 2013).

PCA

The five Proportional Counter Units (PCU) built up the Proportional Counter Array (PCA; Jahoda et al., 1996; Jahoda et al., 2006). The optics consisted of a hexagonal collimator with 1° (full width half maximum) field of view. The nominal energy range is between ∼2 and ∼50 keV.

The best possible timing resolution for the light curves was ∼1 μs, although it was only achievable at the expense of energy resolution of the light curves. Numerous other data modes were available to be chosen from by the observer/proposer.[4]

The energy resolution ($\Delta E/E$ with ΔE full width half maximum) of the spectral data is 0.17 at 6 keV. Several calibration epochs of the PCA are defined based on changes in the voltage or micrometeorite damage to the instruments. The epochs are listed online[5], but see also Sect. 7.1. The calibration of the instrument is especially complicated around Xenon (filling gas of the detectors) absorption edges (see Wilms et al., 2006, for a discussion of their influence on scientific results).

HEXTE

The High-Energy X-ray Timing Experiment (HEXTE; Rothschild et al., 1998) covered the ∼15–250 keV range. It consisted of two clusters (A & B) of 4 phoswich detectors each. The co-aligned field of view, defined by collimator optics, is the same as for the PCA. To

---

[3] `http://xte.mit.edu/ASM_lc.html`

[4] see the ABC of XTE `http://heasarc.nasa.gov/docs/xte/abc/contents.html`.

[5] `http://heasarc.nasa.gov/docs/xte/e-c_table.html`

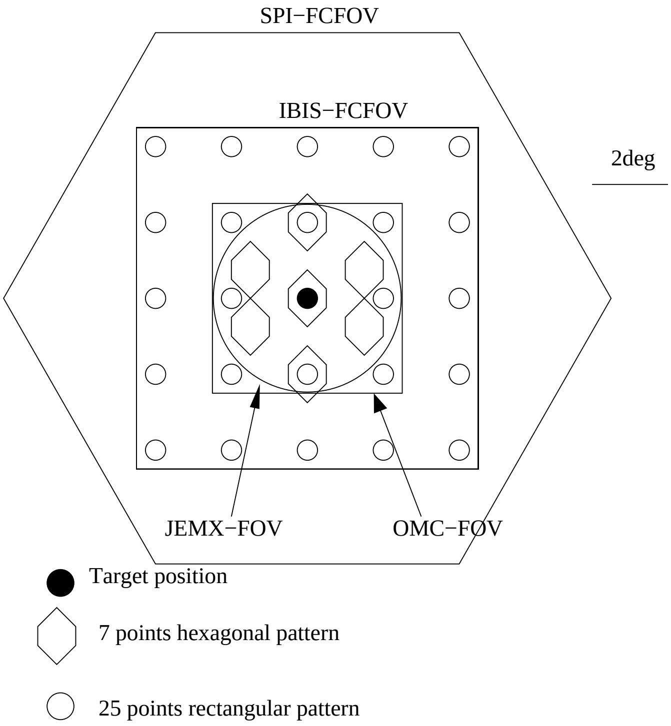

Figure 2.1: INTEGRAL dithering patterns and, respectively, field of view (FOV) and fully coded field of view (FCFOV) of the intstruments on board INTEGRAL (Courvoisier et al., 2003, Fig1).

provide source and background measurements, the clusters rock, i.e., the clusters are alternately rotated 1.5° (or if necessary 3°) off the source every 16, 32, 64, or 128 s.

In the last years of RXTE's lifetime, the rocking mechanism failed, first of cluster A and then of cluster B, leading to problems using the respective clusters (see Sect. 5.1) because of the complicated background of the instruments (see Fig. 6 in Rothschild et al., 1998, and Fig. 4.6 in Kreykenbohm, 2004 for plots of HEXTE background).

2.1.2 INTEGRAL

ESA's International Gamma-Ray Astrophysics Laboratory (INTEGRAL) satellite (Winkler et al., 2003) was launched on 2002 October 17 into a highly eccentric 72-hour orbit that allows for long (∼90% of the orbit), quasi-uninterrupted observations, carried out when the spacecraft is outside of the radiation belts (nominal altitude 60 000 km approaching and 40 000 km leaving the radiation belts). INTEGRAL carries two main scientific instruments: the Imager on-board INTEGRAL (IBIS; Ubertini et al., 2003) and the spectrometer on-board INTEGRAL (SPI; Vedrenne et al., 2003), both working in hard X-rays and γ-rays. They are complemented by two instruments covering lower energies, the twin Joint European Monitors for X-rays that employ the coded mask technique (Jem-X 1 & 2; Lund et al., 2003, see also Westergaard et al. 2003 for the analysis software) and the Optical Monitor Camera (OMC; Mas-Hesse et al., 2003). All instruments are co-aligned.

To improve the resolution and the background correction, INTEGRAL observations are split into individual uninterrupted pointing, so-called Science Windows (ScWs) of usually

$\sim$30 min exposure each, with the satellite dithering in a predetermined pattern from ScW to ScW (Fig. 2.1, but further user-defined pattern are possible, e.g., a random pattern within 2° of the source employed for some of the Cyg X-1 Key Programme observations). ScWs are the basic units for analysis of INTEGRAL data. INTEGRAL observations are identified by the number of spacecraft orbit (revolution) and further by number of ScWs in the given revolution.

IBIS/ISGRI & IBIS as a Compton polarimeter

An overview of the functional principles of coded mask telescopes and the reconstruction techniques for the images is given in great detail by Oertel (2013) and in't Zand (1992), but see also the much shorter articles by Skinner (1995) and Skinner (2004) for a condensed discussion with a focus on the restrictions of coded mask instruments. Here, we assume that the reader has familiarized herself with the basic concept.

IBIS consists of two detector layers located behind a Tungsten MURA (Modified Uniformly Redundant Array) coded mask: the upper layer INTEGRAL Soft Gamma-Ray Imager (ISGRI; Lebrun et al., 2003) and the lower layer Pixellated Imaging Caesium Iodide Telescope (PICsIT Labanti et al., 2003). The nominal sensitivity of ISGRI is from 15 keV to 1 MeV, although note that the lower limit has never been below 18 keV and has increased to 22 keV after revolution 1090 (Chernyakova et al., 2012, see also Popp 2011 for a discussion of some of the calibration problems at low energies in the newest revolutions). PICsIT is nominally sensitive from 170 keV to 10 MeV. IBIS's fully coded field of view is $9^\circ\times9^\circ$ large (see Fig. 2.1) and the partially coded field of view at 50% modulation $19^\circ\times19^\circ$, so that the number of serendipitously observed sources is large for almost any observations, especially in crowded regions such as the galactic center.

The standard ISGRI analysis procedures are introduced by Goldwurm et al. (2003). A user's guide including a cookbook (Chernyakova et al., 2012) can be found online on the websites of the Integral Science Data Centre (ISDC; Courvoisier et al., 2003)[6]. The latest survey catalogues are presented by Bird et al. (2010) and Krivonos et al. (2010). The analysis presented here roughly follows the standard procedures with some convenience adaptations.

Together, ISGRI and SPI can be used as a Compton polarimeter for energies between $\sim$250 keV and $\sim$2 MeV (see Lei et al., 1997, for an extensive review on both mechanisms and detection for γ-ray polarimetry and Forot et al. 2007, 2008 for the special case of INTEGRAL/IBIS). Figure 2.2 sketches the working principle. Events recorded in ISGRI and PICsIT within 2.3 μs are tagged as Compton events, but only 2% of them are truly Compton scattered in IBIS with θ_com and then absorbed in PICsIT, the other 98% are mostly background events and some chance coincidences (Forot et al., 2008). Since the Compton scattering cross section depends on the polarization direction, the distribution of these true Compton counts depends on the azimuth angle Ψ from their incident electric vector:

---

[6] `http://www.isdc.unige.ch/integral/analysis#Documentation`

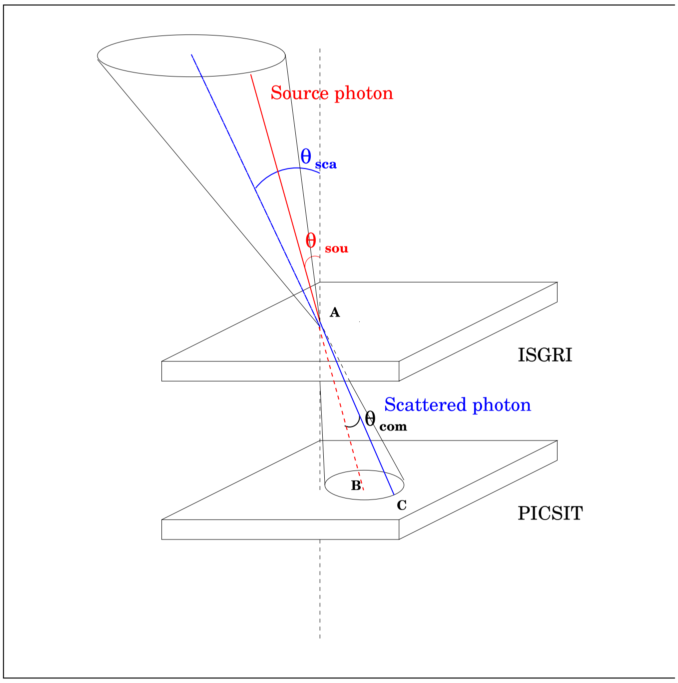

Figure 2.2: Working principle of the IBIS Compton mode: a source photon is Compton scattered in ISGRI and then absorbed in PICsIT. Detection of both events allows to measure the polarization since the Compton scattering cross section is maximum for photons scattered at right angle to the direction of the incident electric vector. Figure from Forot et al. (2007).

$$N(\Psi) = S(1 + a_0 \cos(2\Psi - 2\Psi_0)) \tag{2.1}$$

with the polarization angle $\Psi_o - \pi/2$ and polarization fraction a_0/a_{100} (Forot et al., 2008; Laurent et al., 2012), a_{100} being the amplitude expected for a fully polarized source as obtained from GEANT3 Monte Carlo simulations (Laurent et al., 2003).

The use of the Compton mode is notoriously complex and only few sources have been studied so far: two Gamma-ray bursts (Götz et al., 2009, 2013, also used by Laurent et al. 2011a to set new constraints on Lorentz invariance violation) and two X-ray binaries, the Crab (Forot et al., 2008) and Cyg X-1 (Laurent et al., 2011b). See Laurent et al. (2012) for a concise review that also includes SPI results. Still, the polarimetric capabilities at high energies are a unique feature of INTEGRAL that may enable us to disentangle the origin of this high energy emission in BHBs. For the next decade(s) we are not aware of any further instrument planned that would make similar studies possible.

2.1.3 Swift-BAT

The Burst Alert Telescope (BAT; Barthelmy et al., 2005) on board the Swift X-ray telescope (Gehrels et al., 2004, launched in 2004 November; see also Krauss, 2013 for a very nice introduction on the instruments and data analysis) is a coded mask instrument with a very large field of view of $\sim 60^\circ \times 100^\circ$ whose primary aim is an all sky observation in the 14–195 keV band in order to detect γ-ray burst early and to facilitate fast follow-up observations. While doing so, it accumulates light curves of all sources active in the hard X-ray band (see Baumgartner et al., 2013, for the 70 month catalogue). BAT light curves of all visible sources active in the 15–50 keV band are publicly available in orbit-wise and daily bins.[7] In spite of its lack of soft coverage, BAT is the main all sky monitor available to the scientific community after the demise of RXTE and therefore ASM.

2.1.4 MAXI

The Monitor of All-sky X-ray Image (MAXI; Matsuoka et al., 2009) is installed on the Japanese Experiment Module of the International Space Station (ISS), and bears two instruments, the Solid-State Slit Camera (Tsunemi et al., 2010; Tomida et al., 2011) and the Gas Slit Camera (GSC; Mihara et al., 2011; Sugizaki et al., 2011), which consists of proportional counters and slit-and-slat collimators. The GSC scans the sky every 92 min orbit in the 2–30 keV band, although note that prolonged gaps in the light curve are possible due to the closeness of an object to the sun and obstructions of the field of view, e.g., by the Space Shuttle docked to the ISS. MAXI is also affected by the SAA. Orbit-wise and daily GSC light curves in 2–4 keV, 4–10 keV, and 10–20 keV bands are made available to the public online.[8]

2.1.5 Fermi-GBM

The Gamma-Ray burst Monitor (GBM; Meegan et al., 2009) on board the Fermi mission (renamed from GLAST to Fermi after the successful launch in a near Earth orbit in 2008 June) employs the Earth occultation technique, i.e., it is an uncollimated detector that sees step-like features in the measured count rate when a γ-ray source crosses Earth's limb (Harmon et al., 2002; Case et al., 2011; Wilson-Hodge et al., 2012). The analysis of the data is complex and requires a detailed simulation of the detectors (Hoover et al., 2008; Bissaldi et al., 2009). Quick look data are provided to the scientific community by the Fermi GBM Earth occultation Guest Investigation teams at NASA/MSFC and LSU[9]. The data are binned daily and available in the 12–25 keV, 25–50 keV, 50–100 keV, and 100–300 keV bands as fluxes in mCrab. General results of the GBM survey are discussed by Case et al. (2011) and Wilson-Hodge et al. (2012).

2.1.6 Ryle/AMI

Mullard Radio Astronomy Observatory's Ryle telescope (Pooley, 2006) was an Earth-rotation synthesis telescope[10] with the main aim to map extended radio sources. Gaps in the observation schedule could be used for monitoring – as happened in case of the Cyg X-1 monitoring campaign that is used in this work. Ryle was reconfigured and incorporated into the Arcminute Microkelvin Imager (AMI; Grainge et al., 2012) between 2006 and 2008. Ryle and AMI data used in this work are courtesy of G.G. Pooley, who also has been organizing an observational campaign of Cyg X-1 since 1996, i.e., almost the very start of the RXTE monitoring (see Fig. 4.1).

---

[7] `http://heasarc.nasa.gov/docs/swift/results/transients/`

[8] `http://maxi.riken.jp/top`

[9] `http://heastro.phys.lsu.edu/gbm/`

[10] For a comprehensive book on radio astronomy techniques see Thompson et al. (2001).

2.2 Analysis techniques

2.2.1 Some general considerations

Although – or perhaps because – X-ray data analysis is challenging, few formal introductions exists, Arnaud et al. (2011) being a notable exception. Most information is hidden in the introductory part of theses (e.g., the detailed discussions in Hanke, 2007; Hanke, 2011) or summer school talks[11].

Next to satellite specific software for data reduction, different analysis software is employed. XSPEC (Arnaud, 1996) is most widely used. Here, however, we use ISIS (Houck & Denicola, 2000; Houck, 2002; Noble & Nowak, 2008). For a brief summary of the main advantages of ISIS, in particular the programmability, which allows us to conduct all analysis within the ISIS/s-lang environment including X-ray timing, and the model-independent treatment of unfolded spectra, see Nowak et al. (2005).[12]

A good introduction to the statistical tools used can be gathered combining the books by Arnaud et al. (2011), Wall & Jenkins (2003) and Barlow (1989). We employ the χ^2-statistics (e.g., Wall & Jenkins, 2003, who also nicely list the advantages and pitfalls of the approach) since Cyg X-1 is a bright, rather well-behaved source, but see, e.g., Gehrels (1986) for the discussion of different approaches to faint sources.

2.2.2 X-ray timing analysis

A detailed introduction into the calculation of the Fourier-based X-ray timing parameters used in this work can be found in Nowak et al. (1999) and Pottschmidt (2002), with a more general discussion presented in the overview by van der Klis (1989) and in the seminal book on random data analysis by Bendat & Piersol (2010). The aim of the following introduction is not to give the reader a comprehensive overview, especially since we do not treat questions of background, dead time and noise in detail. The intent is to facilitate an intuitive understanding for the meaning of the introduced quantities and to enable the reader to follow the interpretation of these quantities in the (astro)physical context. In the remaining of this section we closely follow Pottschmidt (2002).

---

[11] In the case of the analysis system used in this work but also for a general introduction see `http://www.black-hole.eu/media/summerschool2/X-ray_Spectra_Part_I.pdf` and `http://www.black-hole.eu/media/summerschool2/X-ray_Spectra_Part_II.pdf` by Dr. M. A. Nowak from the 2010 *2nd School on Multiwavelength Astronomy*.

[12] A reader interested in using ISIS, may find the corresponding wiki entry at the Remeis observatory to be a good starting point: `http://www.sternwarte.uni-erlangen.de/wiki/doku.php?id=isis:tutorial`.

Power spectra

Light curves are time series of count rates l_j with j number of the time bin[13]. Here, we only consider light curves that are evenly spaced[14] with Δt. The corresponding Fourier frequencies are then

$$f_k = \frac{k}{N\Delta t} \tag{2.2}$$

$N\Delta t$ the total length of the light curve and $k \in [-N/2, N/2]$, although only values with $k \geq 1$ have a physical meaning. The (usually complex) discrete Fourier transform, L_k, for a light curve of N time bins is then:

$$L_k = \sum_{j=0}^{N-1} l_j \exp(2\pi jk/N). \tag{2.3}$$

Since an astrophysical light curve is the sum of a signal component, s_j, and noise component, n_j, i.e., $l_j = s_j + n_j$, and since the Fourier transform is linear, it follows that $L_k = S_k + N_k$.

The power spectral density (PSD) P_k, is the squared magnitude of the Fourier transform L_k (and therefore always real) and gives the fraction of the total light curve variance that is due to variability with the frequency f_k. It can be written using the complex conjugate of the Fourier transform, L_k^*, as:

$$P_k = L_k^* L_k. \tag{2.4}$$

Because the uncertainty of a given PSD value is of the order of the value itself, averaging PSDs both in frequency space and over several disparate light curve segments is therefore essential to be able to draw physical conclusions.[15] Note especially that merely increasing the length of the light curve only makes lower frequencies accessible but does not reduce the uncertainties.

The noise in the light curves considered in this work, i.e., BHB light curves, are dominated by the counting noise (Pottschmidt, 2002). This Poisson noise is itself frequency independent, but modified by the occurrence of dead time[16] in the detectors in a frequency-dependent way. Zhang et al. (1995) give an analytical discussion of dead time effects that is also used Zhang et al. (1996) for the treatment of the so-called very large events (cosmic rays) in the PCA-detectors. These considerations are taken into account for X-ray timing analysis throughout this work (see especially Pottschmidt, 2002, Sect. 3.2.4, who

---

[13] We use j not i as in Chapter 7 to avoid confusion with the imaginary unit i.

[14] For treatment of unevenly spaced light curves see, e.g., Scargle (1982) and Horne & Baliunas (1986).

[15] The Discrete Fourier Transform is often – including the instance used in this work – computationally implemented using the Fast Fourier Transform algorithm, which works fastest on segements of the length of 2^n with $n \in \mathbb{N}$.

[16] I.e., the time a detector is not sensitive to incoming photons, in case of proportional counters the time required for the cascade to proceed to the anode.

also show the contribution of the dead time to the Poisson noise in different normalizations).

Cross power quantities

While the PSD characterizes the variability of one light curve, the relationship between two light curves, e.g., simultaneous light curves $l_{h,j}$ and $l_{s,j}$ of the same source in the hard and soft energy bands, can be examined using the (usually complex) cross power density (CPD):

$$C_k = L^*_{h,k} L_{s,k}. \tag{2.5}$$

Coherence function, γ^2, and time lags, δt, the two quantities of interest, are calculated from the CPD, which has to be averaged to obtain meaningful values, as is the case for the PSD.

The coherence function, γ^2, compares the squared norm of the averaged CPD, $\langle C_k \rangle$, with its maximal attainable value, i.e., with the product of the averaged squared norms of the Fourier transforms of two considered time series, $l_{h,j}$ and $l_{s,j}$:

$$\gamma^2 = \frac{|\langle C_k \rangle|^2}{\langle |H_k|^2 \rangle \langle |S_k|^2 \rangle} \tag{2.6}$$

It measures the linear correlation between the two time series (Vaughan & Nowak, 1997) and can, in the ideal noiseless case, obtain values between 1 (ideal coherence) and 0 (no coherence), although noise can lead to larger values. Note that all X-ray timing quantities shown in the following Chapters are noise-corrected if not explicitly noted otherwise.

While the coherence is related to the norm of $\langle C_k \rangle$, the phase lag ϕ_k is the argument of $\langle C_k \rangle$, i.e., the phase difference between $L_{h,k}$ and $L_{s,k}$:

$$\phi_k = \arg(\langle C_k \rangle). \tag{2.7}$$

The corresponding time lag between the light curves is then simply

$$\delta t_k = \frac{\phi_k}{2\pi f_k}. \tag{2.8}$$

The s-lang scripts (`isisscripts`) used for calculation of timing properties throughout this work (especially `foucalc`) are publicly available.[17] See also Pottschmidt (2002) for a discussion of the corresponding IDL tools and Pirner (2009) for the s-lang tools.

---

[17] `http://www.sternwarte.uni-erlangen.de/git.public/`

> ‘Achtung! Im Gebiet der Jagdhunde wurde ein Planet aus seiner Bahn geworfen. Es handelt sich eindeutig um eine Supernova. Dieser Schnelläufer rast auf die Erde zu. Geschätze Geschwindigkeit etwa einhundertsechsundvierzigtausend Kilometer pro Sekunde. Sein Radius gelangt in den Bereich der Riesensterne, er hat die physikalischen Eigenschaften einer Sonne und wird die Erde in kürzester Frist erreicht haben. [...] Notruf von Raumschiff Hydra!’
>
> *(Raumpatrouille Orion, Folge 2 ‘Planet außer Kurs’)*

3

Near real time monitoring of black hole binaries

When a non-periodic transient source goes into outburst or when a persistent source shows potentially scientifically interesting behavior such as a state transition, it is crucial to let the scientific community know as soon as possible to trigger possible follow up observations. The usual way to do this is via the ‘Astronomer’s Telegram’[1], an online portal widely known in the astrophysical community. This Chapter summarizes astronomer’s telegrams (ATels) on the last state transitions of Cyg X-1 during the lifetime of RXTE as well as the serendipitous discovery of an outburst of the transient black hole binary H1743−322 with INTEGRAL. It gives examples for how the theory of states and state transition that was introduced in Sect. 1.3 manifests itself observationally during individual transitions and outbursts and preludes the more general, statistical treatment of states and transitions in Cyg X-1 in Chapters 5 and 6. In particular, we consider examples of state transitions from hard to the soft intermediate/soft state (Sect. 3.1), back from the soft to intermediate state (Sect. 3.2), and a very quick transition into soft state (Sect. 3.3), all for Cyg X-1. The dates of all discussed transitions of Cyg X-1 can be easily put into the context of the long-term source behavior by comparing to the long-term evolution from 1996 to 2012 as presented in Fig. 5.1 and further discussed Chapter 5. H1743−322 serves as an example for the typical transient outburst onset (Sect. 3.4).

The following Sections are strongly based on and in large parts taken in verbatim from the respective ATels. Sect. 3.1 is based on ATel #2751 (Grinberg et al., 2010), Sect. 3.2 on ATel #3307 (Grinberg et al., 2011a), Sect. 3.3 on ATel #3616 (Grinberg et al., 2011b), and Sect. 3.4 on ATel #4418 (Grinberg et al., 2012). All analysis performed in this Chapter used near real time (NRT) data from the RXTE and INTEGRAL satellites. While susceptible to calibration issues and other problems, NRT data is available quasi-instantly and therefore allows prompt announcements to the community.

---

[1] `http://www.astronomerstelegram.org`

Table 3.1: Spectral and timing parameters of RXTE observations of Cyg X-1 discussed in Sect. 3.1

observation	begin obs [UT]	exposure [ks]	radio flux[a] [mJy]	Γ_1	black body norm (from `diskbb`) [10^5]	rms[b] [%]	time lag[c] [ms]
95121-01-13-00	2010-06-19 21:53:52	2.3	14.3	1.82±0.01	not required	28.8	3.0
95121-01-13-01	2010-06-19 23:31:28	2.1	14.4	1.83±0.01	not required	28.5	0.9
95121-01-13-02	2010-06-20 01:08:32	1.9	15.2	1.81±0.01	not required	27.4	1.7
95121-01-14-02	2010-07-04 00:27:28	2.1	9.0	2.65±0.03	$1.3^{+1.2}_{-0.5}$	20.6	8.0
95121-01-14-01	2010-07-04 02:05:20	2.5	5.3	2.60±0.02	$4.4^{+1.5}_{-1.1}$	21.2	13
95121-01-14-00	2010-07-04 03:36:32	1.6	8.0	2.67±0.03	$3.2^{+1.5}_{-1.1}$	21.6	12
95121-01-15-00	2010-07-19 20:03:28	3.3	not available	3.01±0.02	13^{+4}_{-3}	32.7	0.9
95121-01-15-02	2010-07-19 23:12:32	1.5	2.8	2.88±0.03	$3.4^{+2.3}_{-1.5}$	31.2	1.7
95121-01-15-01	2010-07-20 02:20:32	1.2	not available	2.86±0.03	$1.6^{+1.7}_{-0.7}$	31.8	1.5

[a] Radio flux densities are from the AMI array. [b] Soft band (4.5–5.8 keV), in the 0.002–256 Hz range. [c] In the 3.2–10 Hz band, between soft 9.5–15 keV and 4.5–5.8 keV, positive lags mean that the hard band is lagging the soft.

3.1 Cygnus X-1: The 2010 June/July hard to soft state transition

RXTE has performed pointed observations of Cyg X-1 on 2010 June 19/20, 2010 July 4, and 2010 July 19/20 as part of our bi-weekly observational campaign, when following the γ-ray detections with the AGILE satellite (Bulgarelli et al., 2010; Sabatini et al., 2010), a stoferting of the source was detected in radio and with X-ray all sky monitors (Negoro et al., 2010; Rushton et al., 2010a; Wilson-Hodge & Case, 2010; Evangelista et al., 2010; Rushton et al., 2010b) ending a year-long hard state (Nowak, 2008). Therefore, we promptly performed spectral and timing analysis of the NRT data of these observations. The X-ray spectrum can be well described by a broken power law with a break at about 10 keV and photon indices Γ_1 and Γ_2 below and above the break, respectively, with an additional black body component and modified by an iron line and by absorption (Wilms et al., 2006, and Chapter 4). Further state classification is performed based on the timing properties, which allow for a more accurate characterization than spectral parameters alone (Pottschmidt et al., 2000; Böck et al., 2008). Power spectral densities and X-ray time lags were calculated from 4.5–5.8 keV (soft band, channels 11-13) and 9.5–15 keV (hard band, channels 11-13) PCA light curves with 2 ms resolution. So was a hardness intensity diagram (HID, Fig. 3.1). The main parameters are summarized in the Table 3.1.

Following Pottschmidt et al. (2003) and Wilms et al. (2006), the spectral and timing properties on 2010 June 19/20 are indicative of a hard state. Especially, the soft photon index Γ_1 is below 2 and the average time lags are low at $\sim$2 ms (3.2–10 Hz range). The radio flux is high at 14–16 mJy.

On 2010 July 4, the HID (Fig. 3.1) clearly reveals the source to be on its bright soft branch (Böck et al., 2008), as is confirmed by the soft photon index Γ_1 of 2.6–2.7, and the presence of disk emission. We note, however, that the PSD still shows Lorentzian components, the rms is low, and the X-ray time lags are enhanced, all typical characteristics of a transitional state (Pottschmidt et al., 2003). Note that during this phase the radio outflow and hard tails are usually the strongest (Cadolle Bel et al., 2006; Wilms et al., 2007).

On 2010 July 19/20 the soft state is reached: the hardness of the source decreases compared to 2010 July 4 while the count rates are comparable. Both, the Γ_1 and the contribution of the disk emission, increase further. A cut-off power law without further Lorentzian components offers a good description of the PSDs and the averaged X-ray time lags are again low.

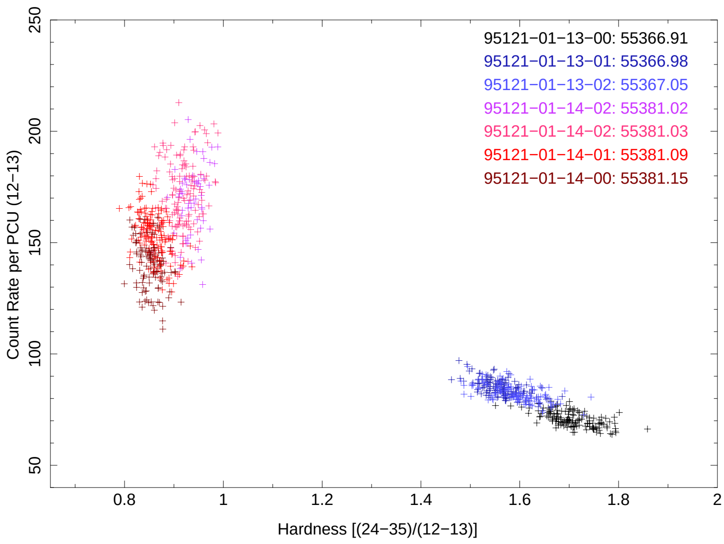

Figure 3.1: Hardness-intensity diagram of the RXTE-PCA observatios of Cyg X-1 on 2010 June 19/20 (ObsID 95121-01-13-XX) and on 2010 Jul 4 (ObsID 95121-01-14-XX) – see Sect. 3.1 for discussion and Table 3.1 for spectral and timing parameters of the individual observations. Figure courtesy of M. Böck.

3.2 Cygnus X-1: The 2011 April soft to intermediate state transition

This Section reports RXTE, INTEGRAL, and AMI observations of Cygnus X-1 in 2011 April as the source transited from the soft into the intermediate state. After having spent 2006 to mid-2010 in an extraordinarily hard state (Nowak et al., 2011; Grinberg et al., 2013, see also Chapter 5 and 7), the source entered a soft state in summer 2010 (Negoro et al., 2010; Rushton et al., 2010a; Wilson-Hodge & Case, 2010; Evangelista et al., 2010; Rushton et al., 2010b; Grinberg et al., 2010; Tudose et al., 2010, see also Sect. 3.1). This soft state came to an end in April 2011. The Swift-BAT hard X-ray flux started to recover, showing an increasing trend starting around 2011 April 18. Similarly, the AMI radio flux recovered from being consistent with zero to almost its canonical hard state value of 15 mJy between 2011 April 09 and 2011 April 25. This picture is supported by our pointed X-ray observations discussed in the following. For an overview of the BAT and AMI evolution throughout 2011 see Fig. 3.2.

INTEGRAL observations were performed on 2011 April 11/12. The 20–500 keV INTEGRAL/ISGRI spectrum (66 ks exposure) was well described by a power law with a photon index of 2.63±0.02, consistent with results from our INTEGRAL Key Programme observations throughout the soft state.

An overview over the available RXTE/PCA data used in this Section is given in Table 3.2.[2] The 3–40 keV RXTE/PCA spectra (exposure ∼1.4–2.3 ks) can be described by the same model employed previously in Sect. 3.1. We also determined rms variability values (for 0.008–256 Hz range; narrower than the 0.002–256 Hz of Sect. 3.1 and Grinberg et al. 2010 due to shorter exposure times) and averaged timelags (for 3.2–10 Hz range) for

---

[2] No HEXTE data are used here since the rocking mechanisms of both HEXTE detectors have failed by 2011 April.

Table 3.2: Spectral and timing parameters of RXTE observations of Cyg X-1 discussed in Sect. 3.2

obs start [UT]	radio flux[a] [mJy]	Γ_1	soft band rms[b] [%]	timelag[c] [ms]
2011-04-09	no detection			
2011-04-12 04:12:32		3.02±0.12	31.1	−0.3±0.9
2011-04-12 05:50:24		3.29±0.13	20.8	2.2±1.3
2011-04-12 07:27:28		2.95±0.15	26.0	4.5±1.4
2011-04-12 09:05:36		3.14±0.20	28.6	3.5±1.6
2011-04-14 07:37:55	6.4			
2011-04-16 08:49:54	5.6			
2011-04-19 11:45:35	5.8			
2011-04-21 08:25:28	8.5			
2011-04-22 02:18:24		2.71±0.08	20.2	6.8±1.7
2011-04-22 03:55:28		2.69±0.11	23.3	5.0±1.1
2011-04-22 05:32:32		2.76±0.13	22.8	4.6±1.7
2011-04-22 05:49:53	6.4			
2011-04-22 07:08:32		2.71±0.10	15.3	3.5±1.6
2011-04-22 08:36:32		2.69±0.12	20.0	11.6±2.1
2011-04-24 02:19:38	6.5			
2011-04-25 08:57:06	12.1			

No contemporary X-ray and radio measurements are available. [a]Radio flux densities are from the AMI array. [b] Calculated in the 0.008-256 Hz range. [c]In the 3.2–10 Hz band, between soft 9.5–15 keV and 4.5–5.8 keV, positive lags means that higher energies are lagging the soft.

4.5–5.8 keV and 9.5–15 keV PCA lightcurves. A summary of selected parameters (the disk parameters are not well constrained and therefore not included) is presented in Table 3.2.

The decreasing photon index Γ_1 (Γ_1 and Γ_2 are correlated, see Wilms et al. 2006 and Sect. 4.2.2) between 2011 April 12 and 2011 April 22, the comparatively low rms values, the radio flux turn-on/increase, and especially the enhanced time lags on 2011 April 22 are typical indicators that Cyg X-1 has entered a transitional state. The photon index Γ_1 on 2011 April 22 is consistent with the one measured for the RXTE monitoring observation on 2010 July 04, and classified as transitional in Sect. 3.1 and in Grinberg et al. (2010). Abrupt parameter changes within the transitional state have been observed at $\Gamma_1 \approx 2.5$ before (transition between hard intermediate and soft intermediate states, Böck et al. 2011). Cyg X-1 appears close to this Γ_1-range.

Even if the source would have failed to reach the full hard state after this transition, this episode could still be described as a reverse failed state transition, analogous to the previously observed failed state transitions from the hard to the soft state (Pottschmidt et al., 2003).

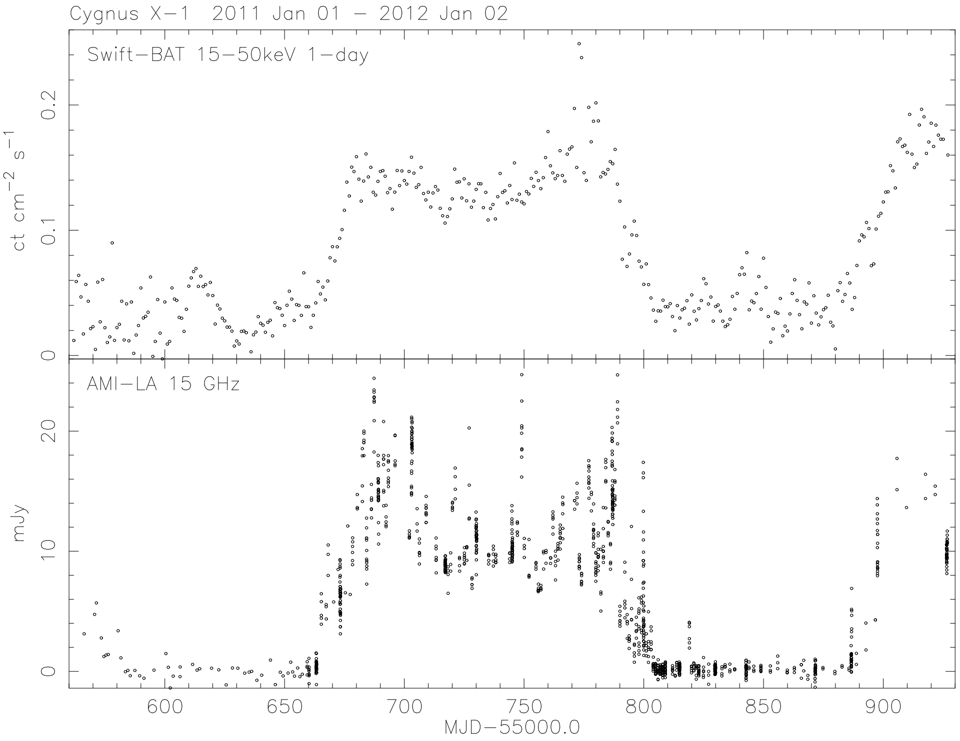

Figure 3.2: Radio (AMI) and hard X-ray (Swift-BAT) light curves of Cyg X-1. Figure courtesy of G.G. Pooley, `http://www.mrao.cam.ac.uk/~guy/cx1/2011.ps`.

3.3 Cygnus X-1: 2011 August transition into soft state

Radio and X-ray monitoring observations during end of 2011 July and early 2011 August (Negoro et al., 2011, MAXI/GSC; Pooley 2011, AMI; Trushkin et al. 2011, RATAN) indicated Cyg X-1 entering the soft state. A plot of the behavior of Cyg X-1 as observed with AMI and BAT is shown in Fig. 3.2.

Our bi-weekly RXTE monitoring campaign of Cyg X-1 showed that the source transited into a soft state between August 13 and August 26. Three groups of observations were conducted: on July 29 (ObsID 96121-01-16-00/01/02/03/04, overall exposure 10 ks), August 13 (96121-01-17-00, overall exposure 16 ks) and August 26/27 (96121-01-18-00/01/02/03, overall exposure 6 ks). As previously in Sects. 3.1 and 3.2, we modeled the 3–40 keV RXTE/PCA spectra with a broken power law, an iron line, an absorption component and, where required, a disk black body.

July 29: The soft photon index of $\Gamma_1 \sim 1.9$–2.0 and the average 3.2–10 Hz time lag ranging between 3 ms and 4 ms point towards a softer mode of the hard state. The PSDs in the 0.008-256 Hz range show a clear two-humped structure without a power law component. No black body component is required in the spectral fits.

August 13: The spectra are similar to those from July 29, with a slight softening of the photon index Γ_1 to 2.05–2.15 and an increase of the avegra lags to 4–5 ms. The PSDs remain two-humped with no or very small power law contribution and the black body is still not required. This behavior is still indicative of a softer mode of the hard state or of the hard intermediate state.

August 26/27: A multi-temperature black body component (diskbb) with a temperature of 0.35–0.50 keV is clearly required in the fits. The spectrum is steep, with a soft power law index Γ_1 between 2.7 and 2.9. The time lag is highly variable between 9 ms and −0.2 ms and the PSDs show a strong power law component as is typical for the soft state.

Taking into account X-ray all sky monitors and radio monitoring data, we conclude from these three pointed observations that the source has transited into a soft state between 2012 August 13 and 2012 August 26. This is especially interesting since the transition occurred so quickly after the end of the previous prolonged soft state, which lasted from July 2010 to April 2011 (see Sect. 3.2 and Grinberg et al., 2011a).

3.4 H1743−322: 2012 September outburst onset

This section reports the onset of the outburst of the black hole binary H1743−322 (IGR J17464−3213) as detected by INTEGRAL during the monitoring of the new galactic center transient Swift J174510.8−262411. Note that INTEGRAL is less sensitive than RXTE, only covers higher energies[3] and only allows for timing analysis for very bright sources and not to the quality available with RXTE (Grinberg et al., 2011c).

The source was first detected in INTEGRAL/ISGRI near real time data covering MJD 56190.471–56191.372 (2012 September 20/21, part of INTEGRAL revolution 1213) with 8.3 mCrab in the 20–40 keV band and 11.1 mCrab in the 40–80 keV band.

The flux increased to 24.1 mCrab (20–40 keV) and 38.9 mCrab (40–80 keV) on MJD 56191.724–56192.163 (2012 September 21/22, part of INTEGRAL revolution 1214) and H1743−322 was detected in the 80–150 keV range at 53 mCrab.

In the data of MJD 56192.164–56193.044 (2012 September 22/23, part of revolution 1214) the source has further brightened to 37.5 mCrab in the 20–40 keV band, 52.1 mCrab in the 40–80 keV band and 64.4 mCrab in the 80–150 keV band. At this time, a 4.3 sigma detection at 65 mCrab was possible in the 150–300 keV band. The source spectrum at this point can be described by a power law with a high energy cutoff with a the photon index of ∼1.5 and a cutoff energy of ∼100 keV.

The Jem-X soft X-ray coverage is sparse, resulting in 3–7 keV upper limits of 11 mCrab and 17 mCrab in revolutions 1213 and 1214, respectively.

The evolution of the INTEGRAL fluxes and the spectral shape indicates that the source

---

[3] Except when Jem-X data are available, which is usually only the case for the main observations target due to the much smaller Jem-X field of view. Some coverage of sources close to the prime target of an observation with Jem-X is possible because of INTEGRAL's dithering strategy (Sect. 2.1.2).

was in a hard state in April 2012, typical for the onset of an outburst of transient black hole binaries.

Observations of the source with all-sky monitors confirm this conclusion: An increase in the 15–50 keV flux by a factor of >5 within during a week as compared to the previous quiescence of the source can also be seen in the Swift/BAT data. A transient warning has been issued by the MAXI transient alert system on 2012 September 24.

> Spectrum analysis enabled the astronomer to tell when a star was advancing head on, and when it was going the other way. This was regarded as very precious. Why the astronomer wanted to know, is not stated; nor what he could sell out for, when he did know. An astronomer's notions about preciousness were loose. They were not much regarded by practical men, and seldom excited a broker.
>
> *(Mark Twain, "The Secret History of Eddypus")*

4 Spectral evolution with RXTE

MONITORING campaigns with pointed instruments such as INTEGRAL and RXTE offer a unique glimpse of the long term spectral evolution of different sources at moderate spectral resolutions. They allow us to place individual observations in the greater context, even though they may not be as well suited for in-detail studies of individual parameters, such as absorption or reflection, as individual observations with higher resolution instruments such as Chandra or XMM. A detailed knowledge of the long term evolution is, however, key to interpreting individual observations.

In the following, we give an overview over the data (Sect. 4.1) of the RXTE campaign, discuss the application of empirical broken power law to describe the data (Sect. 4.2) and address the orbital variability of absorption as seen by RXTE in the light of clumpy wind models for the stellar wind of HDE 226868 (Sect. 4.3). We summarize our results in Sect. 4.4.

4.1 Data

This Chapter is based on 2741 orbits of RXTE observations of Cyg X-1 from the beginning of the mission in late 1995 to the end in early 2012. This encompasses all observations of Cyg X-1 ever made with RXTE and includes the bi-weekly observational campaign which was carried out since 1999. For the bi-weekly campaign simultaneous radio observations with the Ryle radio telescope (Sect. 2.1.6) have been carried out from the beginning of 1999 until middle of 2006. After the refurbishment of the instrument (Pooley, 2006), the campaign was continued with the now renamed AMI array from middle of 2008 on (see Fig.4.1).

We use data from all three instruments on board RXTE (Sect. 2.1.1): ASM, PCA, and HEXTE. For PCA, we use data from the top Xenon layer of PCU 2 only, i.e., the best calibrated data from the PCU which has been on during all the observations. We make use of the improved PCA background models and only discard data within 10 minutes

Table 4.1: Systematic errors used for different PCU calibration epochs.

epoch	MJD	channels with 1% sys. err.	channels with 0.5% sys. err.	# obs.
1	<50163	6-7	8-9	15
2	50163-50188	5-6	7	25
3	50188-51259	4	5	333
4	51259-51676	3	4	395
5	>51677	3	4	1976

In this Chapter, we follow the convention of `http://heasarc.nasa.gov/docs/xte/e-c_table.html` and list channel numbers for the `std2` mode starting with 0, while Böck et al. (2011) and Grinberg et al. (2013) and therefore also Chapter 5 started counting with 1.

of South Atlantic Anomaly (SAA; Fürst et al., 2010) passages, as opposed to 30 minutes in earlier works (Pottschmidt et al., 2003; Wilms et al., 2006). For spectral analysis we extracted PCA spectra in the `standard2f` mode for each RXTE orbit: we obtain a total of ~4.8 Ms (~55 d) of data in 2741 spectra with a mean PCA exposure of about 1.7 ks. The improved PCA background and response allow us to consider a wider energy range than previously, namely ~2.8–50 keV, though exact values depend on the epoch used. This approach means a wider overlap between the PCA and HEXTE spectra, which are considered between 18 keV and 250 keV, and therefore a better constraint on the multiplicative constant used to account for the differences in the flux calibration of the two instruments. Following Böck et al. (2011) we added a systematic error of 1% to the fourth PCA bin (`std2` channel 3, 2.8–3.2 keV) and of 0.5% to the fifth PCA bin (`std2` channel 4, 3.2–3.6 keV) in the data from epoch 5[1], which constitutes the majority of out data set. For epochs 1 to 4 we aim for the closest possible match in energy (see Table 4.1) for the systematic errors. No further systematic errors were used.

A careful examination of all best-fit spectra suggests the existence of a calibration feature at $\lesssim 5$ keV, i.e. in the region of the Xenon L edges (Jahoda et al., 2006; Wilms et al., 2006). The structure in the residuals is however small, not always present, and at a position in the spectrum where it usually does not strongly influence any of the model components for models employed in the following (but see Sect. 7.1.2 for some possible influence on the fits and how it is treated). We therefore neither try to model this feature, since globally modeling it using, e.g., a Gaussian component would also compromise spectra where it is not visible, nor do we take it into account by adding additional systematics to our data.

---

[1] Over its lifetime the PCA saw four different gain and calibration epochs, followed by a long fifth epoch defined by the loss of the propane layer in PCU0 in 2000 May. See `http://heasarc.gsfc.nasa.gov/docs/xte/e-c_table.html` for details. These epochs are not to be confused with the five activity periods of Cyg X-1 that we define in Fig. 5.1 and Sect. 5.2.1, see also Grinberg et al. (2013)

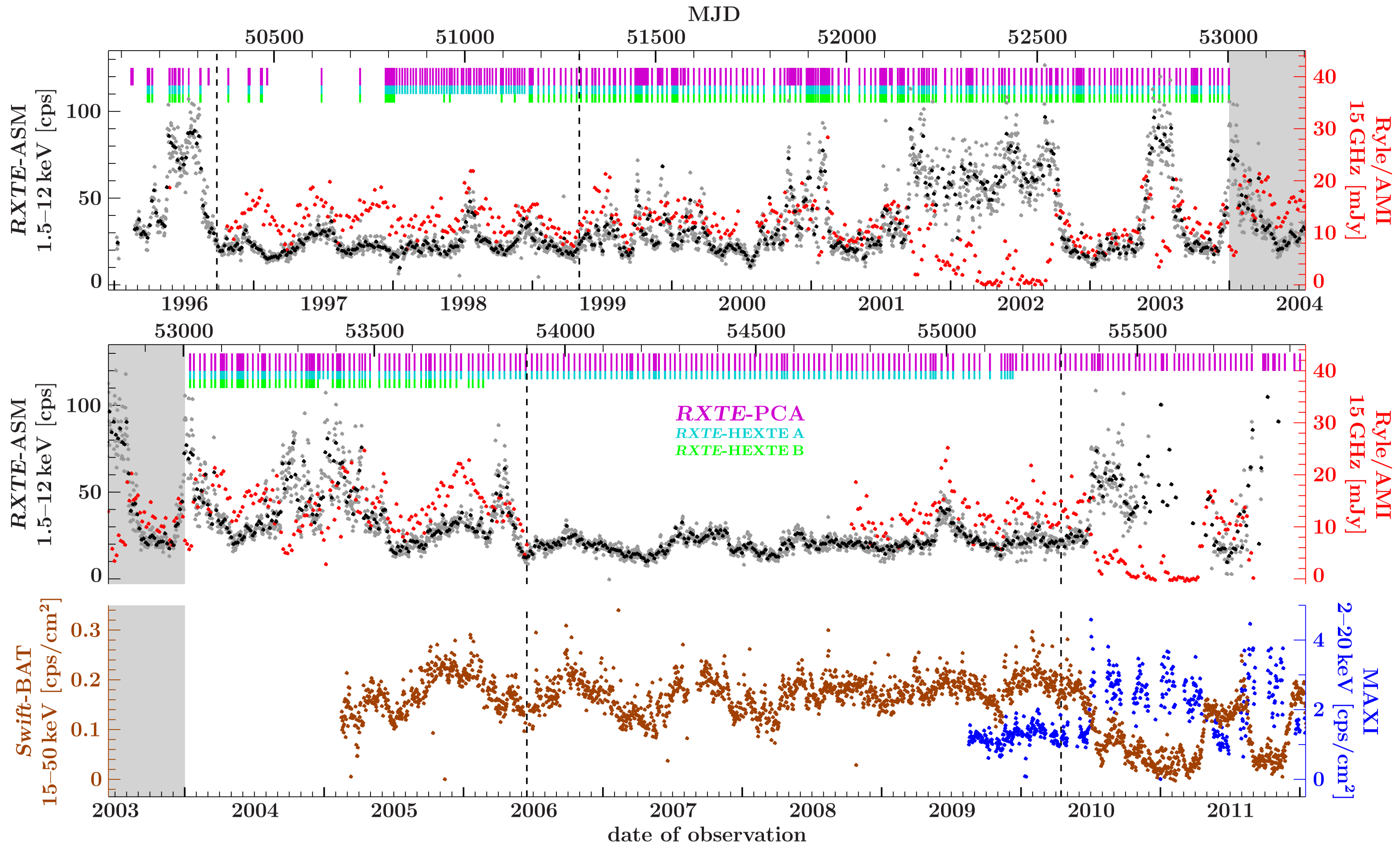

Figure 4.1: RXTE-ASM (black: binned to 5.6 days, i.e., one orbital period of the source; gray: binned to 1 day) and Ryle/AMI (red, binned to 5.6 days) as well as *Swift*-BAT (brown, binned to 1 day) and MAXI (blue, binned to 1 day) data for Cyg X-1. Additionally the dates of all 2741 single RXTE orbits used in this analysis are shown by dashes with colors indicating the different instruments operating during a given orbit: magenta represents PCA, blue HEXTE cluster A and green HEXTE Cluster B.

We group both PCA and HEXTE data to a signal to noise ratio (SNR) of 10. Because of the strong decrease in flux at high energies during the soft state and the low SNR for especially short observations this means that the effective upper energy bound is lower than 250 keV in most cases.

In several early observations no HEXTE data are available (see Fig.4.1). Additionally, the HEXTE A cluster was parked in on-source position in October 2006[2]; the HEXTE B cluster was parked in off-source position in December 2009[3]. Both instruments have not been moved after this occurrences. Since background models for HEXTE are still not reliable, no HEXTE A data are available after October 2006 and no HEXTE B data after December 2009. Overall, we do not have any HEXTE data for 507 individual orbit-wise observations.

4.2 Empirical modelling

4.2.1 Broken power law models

Wilms et al. (2006) have analyzed the 1999–2004 subset of spectral data of Cyg X-1 on an ObsID timescale and shown that a simple phenomenological description of the joint PCA and HEXTE spectrum by an absorbed broken power law with a high energy cut off and an Fe Kα line is a good description of the data. They find that for the harder states, the quality of simple broken power law fits exceeds that of different, more complex Comptonization models. Power law and broken power law models have also been successfully employed to describe other sources and the value of the photon index has been shown to be a good proxy for the spectral state (e.g., Dunn et al., 2010, 2011).

Here we use a broken power law model

$$\texttt{bknpower}(E) \propto \begin{cases} E^{-\Gamma_1} & \text{for } E \leq E_{\text{break}} \\ E_{\text{break}}^{\Gamma_2-\Gamma_1} E^{-\Gamma_2} & \text{for } E \geq E_{\text{break}} \end{cases} \tag{4.1}$$

with the soft photon index Γ_1, the hard photon index Γ_2 and the break energy E_{break}. It is modified by a high energy cut off with the cut off energy E_{cut} and an e-folding energy E_{fold}:

$$\texttt{highecut}(E) = \begin{cases} \exp((E_{\text{cut}} - E)/E_{\text{fold}}) & \text{for } E \geq E_{\text{cut}} \\ 1 & \text{for } E \leq E_{\text{cut}}, \end{cases} \tag{4.2}$$

and by absorption using `tbnew`[4], an updated version of the `TBabs` model with the `wilm` abundances from Wilms et al. (2000) and the cross sections of Verner et al. (1996). Following the results of Xiang et al. (2011), we adopt a minimum absorption column of $N_{\text{H,min}} = 4.8 \times 10^{21}\,\text{cm}^{-2}$, which is their best result for the galactic absorption columns

---

[2] https://heasarc.gsfc.nasa.gov/docs/xte/whatsnew/newsarchive_2006.html#_hexteA-norock

[3] https://heasarc.gsfc.nasa.gov/docs/xte/whatsnew/newsarchive_2010.html#hexteB_locked

[4] http://pulsar.sternwarte.uni-erlangen.de/wilms/research/tbabs/

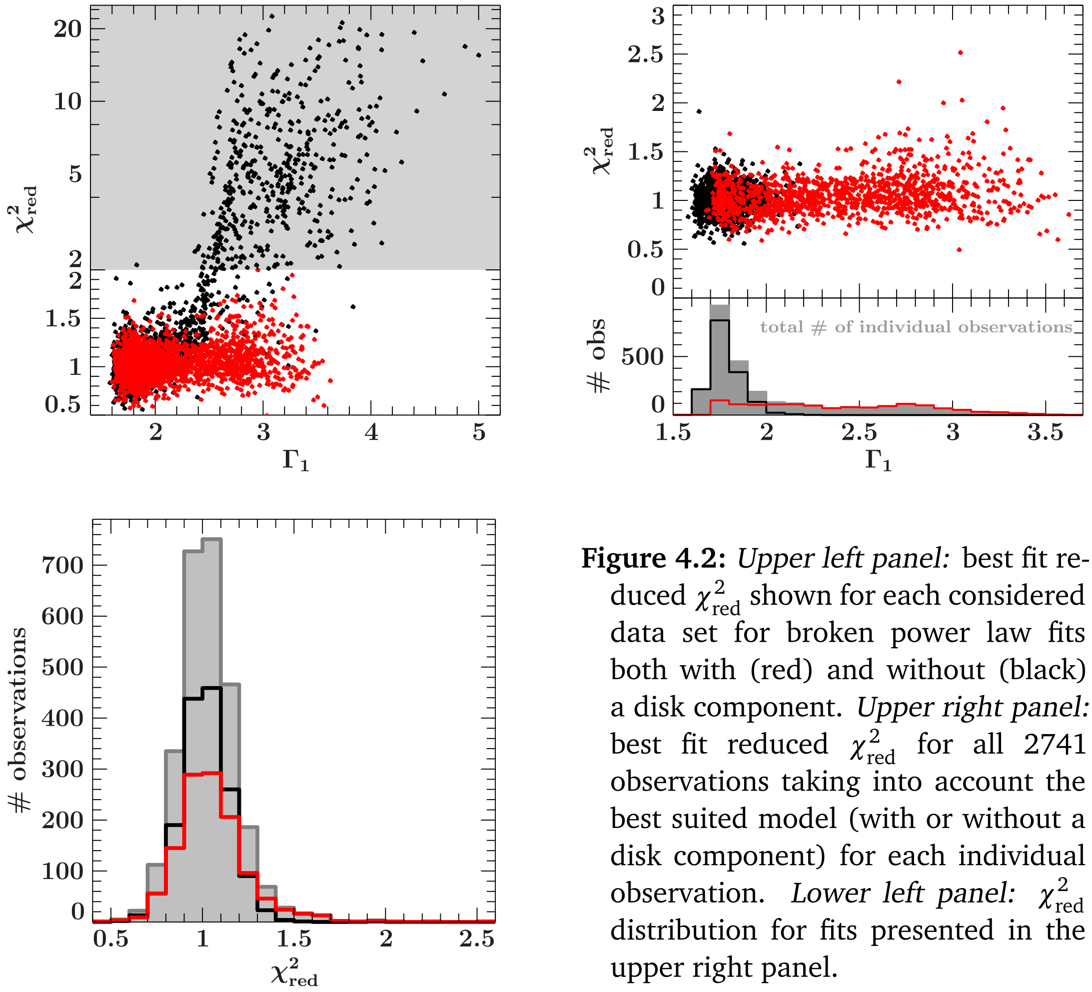

Figure 4.2: *Upper left panel:* best fit reduced $\chi^2_{\rm red}$ shown for each considered data set for broken power law fits both with (red) and without (black) a disk component. *Upper right panel:* best fit reduced $\chi^2_{\rm red}$ for all 2741 observations taking into account the best suited model (with or without a disk component) for each individual observation. *Lower left panel:* $\chi^2_{\rm red}$ distribution for fits presented in the upper right panel.

between an Earth-bound observer and Cyg X-1. We model the Fe Kα line at $\sim$6.4 keV (Thompson et al., 2009), which is required by the data, with a Gaussian component centered at E_0 with width σ and flux A [photons s^{-1} cm^{-2}]. For the hard state observation this model is sufficient for a good description of the spectral shape of Cyg X-1.

An examination of the best fit models shows that this model does not give a good description of softer data (for $\chi^2_{\rm red}$-values see Fig. 4.2, upper left panel) – a behavior expected seen, e.g., in the analysis of individual observations in Chapter 3. A soft component is required and clearly seen as an excess in the residuals of the individual fits where no good fit with the simple model is possible. We interpret this excess as an accretion disk (cf. Sect. 1.2) and model it with the `diskbb` model (Makishima et al., 1986; Mitsuda et al., 1984), which describes a multi-color disk with the inner disk temperature $T_{\rm in}$, a temperature profile that depends on the disk radius as $r^{-3/4}$, and a normalization parameter.

We re-fit all data with this additional component and choose the best model for every individual data set comparing the values of χ^2 of the fits with and without the disk component: if the addition of the disk component leads to an improvement of 5% or more, we accept the disk as real.[5] We treat some outliers as described in Sect. 7.1.2.

The hardest observations do not require the disk component in the predominant number of cases (Fig. 4.2, upper right). The fraction of observations that require a disk becomes significant only for observations with $\Gamma_1 \gtrsim 1.9$. In total 1204 observations require a disk and 1537 do not. The good quality of the fits both with and without the disk (Fig. 4.2, lower left) is notable for our automated fitting approach, especially when comparing, e.g., to the results of Dunn et al. (2010, cf. their Fig. 2) for a sample of BHBs.

The determination of the very existence of the disk and of the disk parameters is notoriously complicated with RXTE (e.g., Dunn et al., 2011), especially for low disk temperatures such as the 0.2–0.5 keV in Cyg X-1, even for a bright source and when a careful treatment of the data such as the one presented here allows to use the lower PCA channels. Where the disk exists, additional degeneracies in our model, especially with the absorption parameter N_H, are introduced. However, orbital variations of N_H due to material local to the source (Bałucińska-Church et al., 2000; Hanke, 2011; Miškovičová et al., 2013) necessitate fitting of N_H instead of employing a constant value which disregards the orbital variations (Sect. 4.3).

A further complication is that not all data sets presented here include HEXTE data as seen on Fig. 4.1. The problem is most striking for the series of prolonged soft states after MJD 55200 when both HEXTE clusters stopped rocking. The lack of high energy data means that we cannot constrain E_fold, as apparent from a visual inspection of Fig. 4.3. Because of the evolution of the E_fold (Fig. 4.3), constraining it to a constant value does not allow for acceptable fits in the soft state observations. We therefore fit E_fold but exclude observations with no HEXTE data from the following discussion of the `highecut` parameters.

4.2.2 Parameter correlations

We first address relationships between parameters of the spectral fits and show scatter plots for all relevant parameters of the broken power law and the high energy cut off in Fig. 4.3. All parameters show strong, often non-linear correlations, as already noted by Wilms et al. (2006), but shown here for a much larger sample of observation, especially with a better coverage of intermediate and soft states.

- In correlations that involve E_fold, data without HEXTE coverage are clear outliers – not unexpectedly, given how the average values of E_fold are $\gtrsim$100–150 keV even in the soft state. Correlations with E_cut also seem slightly affected. All other parameter combinations seem well constrained even when only PCA data are available.
- There is a strong correlation between the soft and the hard photon indices, Γ_1 and Γ_2, also represented as a correlation between Γ_1 and $\Delta\Gamma = \Gamma_1 - \Gamma_2$ (Wilms et al., 2006). The Γ_1-Γ_2 correlation becomes slightly steeper for higher Γ_1. Note

---

[5] Only for the three orbits in ObsID 10238-01-03-00 and single orbits from the ObsIDs 50119-01-06-01 and 60090-01-45-02 neither model could yield fits with $\chi^2_\mathrm{red} < 2.5$. An examination of this data suggests incorrect background extraction either in PCA or HEXTE data. We therefore excluded these orbits from our analysis. They are *not* counted to the quoted 2741 individual RXTE orbits used for the analysis.

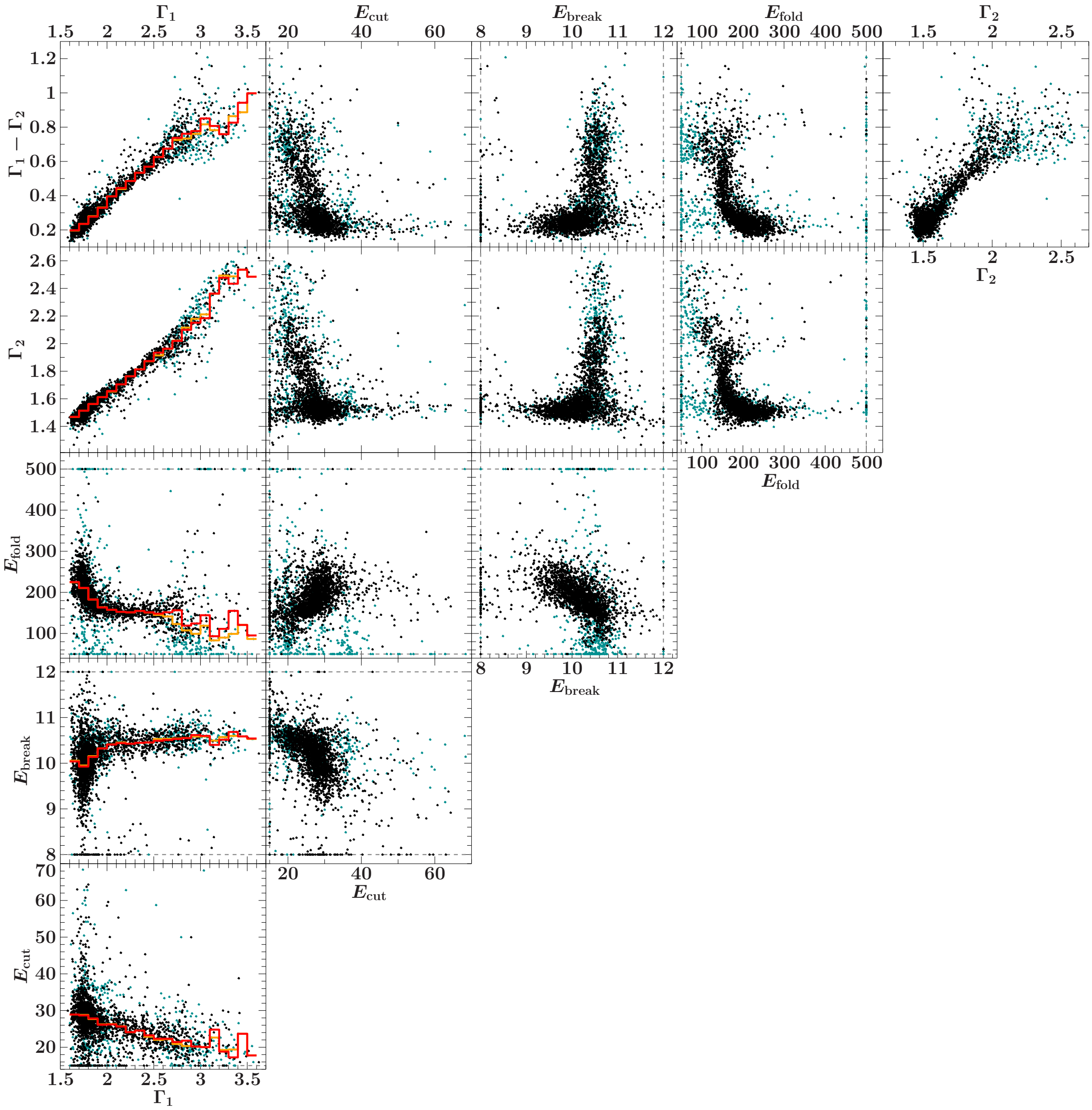

Figure 4.3: Relationships between the parameters of the broken power law and high energy cutoff model components for all Cyg X-1 observations. Observations that have both PCA and HEXTE data are shown in black, observations that lack HEXTE data in blue. Grey dashed lines denote hard limits for the respective parameters. For the correlations involving Γ_1, we show medians of all data in orange and only of those that have HEXTE coverage in red.

that for the softest observations, the correlation between Γ_1 and $\Delta\Gamma$ is especially weak compared to the hard observations, even when taking into account only those observations which have HEXTE coverage.

- We only consider values of E_{fold} when HEXTE data are available. Γ_1-dependent

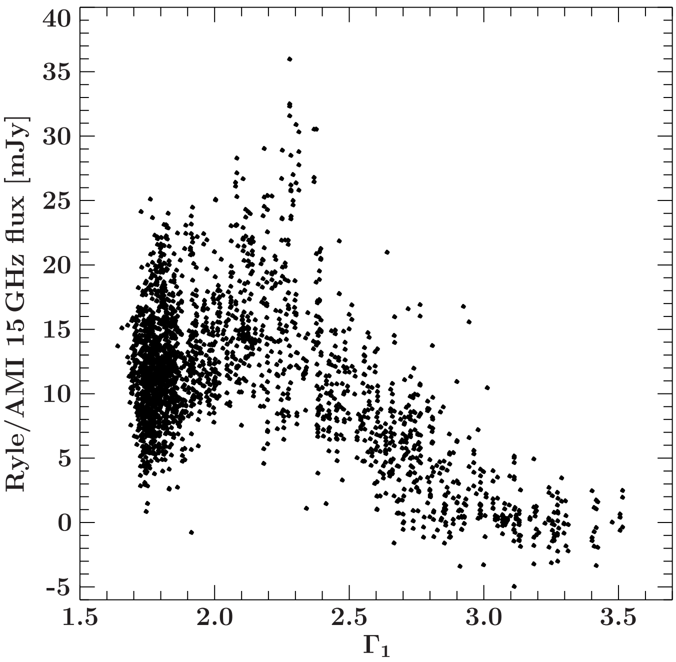

Figure 4.4: Relationship between radio flux as measured by Ryle/AMI at 15 GHz and the soft photon index Γ_1. Only radio measurements strictly simultaneous to pointed RXTE observations are shown; note that one RXTE observation can correspond to multiple radio measurements, resulting in the vertical 'stripes'.

behavior of E_{fold} is clearly non-linear: the median E_{fold} decreases for $\Gamma_1 < 2.0$ and is constant at ~160 keV for $2.0 < \Gamma_1 < 2.6$. While comparatively few observations are usable to constrain the parameters of the high energy cutoff in the soft state, E_{fold} seems to show stronger variations, especially towards higher values. This result is especially interesting when compared to the results of Motta et al. (2009) for GX 339−4, who see a decrease of the e-folding energy of the exponential roll-off as the source enters the intermediate state and a recovery of the e-folding energy in the soft state.[6] While the behavior seen here does not follow the same clear trend, further investigation employing better high energy coverage in the soft state, e.g., with INTEGRAL, seem promising.

- The break energy of the power law, E_{fold}, is remarkably constant for $\Gamma_1 > 2.0$ at ~10.5 keV, with a possible slight increasing trend for the median value.

The radio activity of the source shows clear correlations with spectral shape (Fig. 4.4): while the amplitude of possible values at a given Γ_1 is large, the general trend is towards higher radio flux when the source softens until $\Gamma_1 \approx 2.1$–2.3 and a decrease in radio flux above this Γ_1 value. At about $\Gamma_1 \approx 2.7$–2.8, the radio data are consistent with scatter around zero. Interestingly, this Γ_1-value roughly corresponds to the Γ_1-value where we see clear changes in the X-ray timing parameters: the PSDs become dominated by the power law component (Sect. 7.2.2) and the average timelags show an abrupt return to small values (Sect. 7.3.3).

---

[6] Motta et al. (2009) use the `cutoffpl` model $\mathtt{cutoffpl}(E) \propto E^{-\Gamma} \exp(E/E_{\mathrm{cutoff}})$, so that that the parameter they discuss as "cutoff energy" actually corresponds to our E_{fold}.

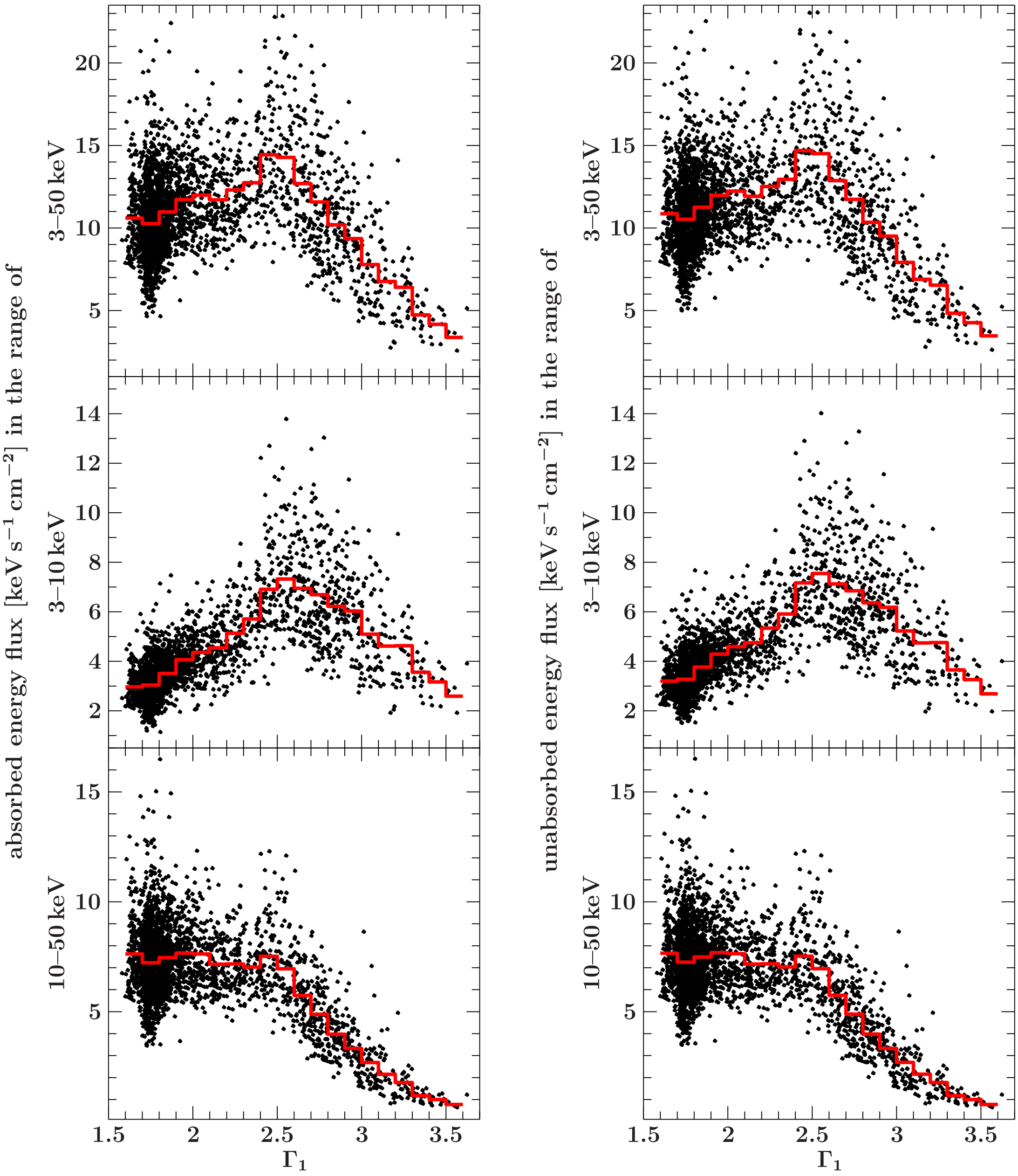

Figure 4.5: Absorbed (left) and unabsorbed (right) energy flux in the 3–10 keV, 10–50 keV and 3–50 keV bands for the best fit broken power law models of the pointed RXTE observations. Note that the 10–50 keV range is not affected by absorption. Differences in 3–10 keV and 10–50 keV ranges are small.

4.2.3 Evolution of flux with spectral state

Figure 4.5 shows the relationships between the soft spectral index Γ_1 and the flux in the 3–50 keV, 3–10 keV, and 10–50 keV energy ranges. The influence of the absorption on the total flux is small and both absorbed and unabsorbed flux show the same trends.

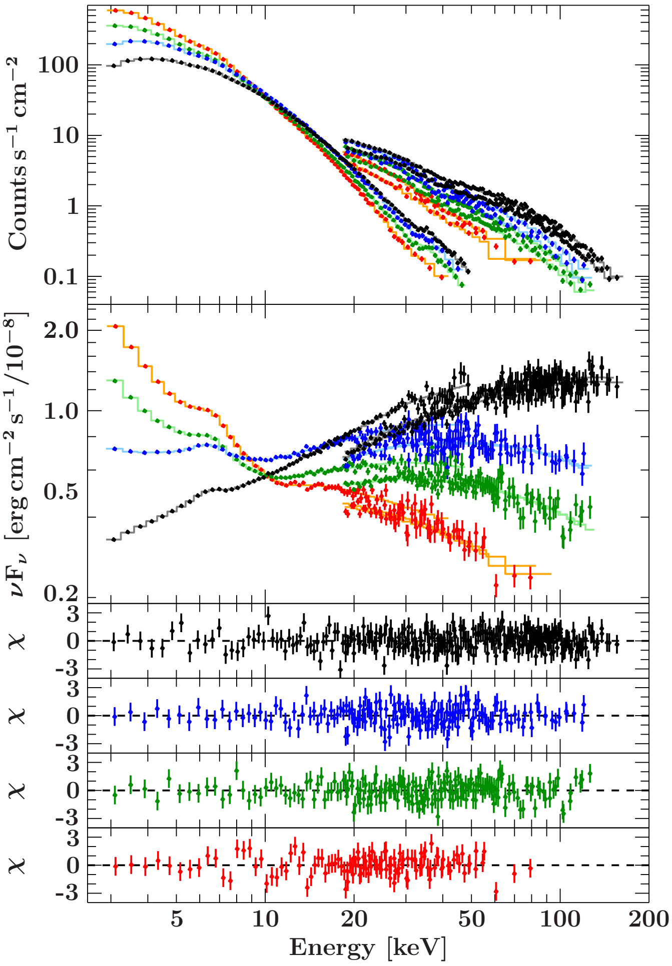

Figure 4.6: Different spectral shapes within the same 3–50 keV flux range of 1.05–1.15 keV$\text{s}^{-1}\text{cm}^{-2}$. Each spectrum shown consists of one PCA and two HEXTE (A & B) spectra (the jump is due to the different normalizations between the instruments). From hardest to softest the respective values of the soft power law index and the reduced χ^2 are:

- $\Gamma_1 \approx 1.6$ and $\chi^2_{\text{red}} \approx 0.98$ for 261 DOF (shown in black),
- $\Gamma_1 \approx 2.1$ and $\chi^2_{\text{red}} \approx 1.06$ for 159 DOF (shown in blue),
- $\Gamma_1 \approx 2.6$ and $\chi^2_{\text{red}} \approx 1.05$ for 181 DOF (shown in green),
- $\Gamma_1 \approx 3.0$ and $\chi^2_{\text{red}} \approx 1.15$ for 102 DOF (shown in red).

The behavior of the flux is consistent with the one seen by Grinberg et al. (2013) and in Chapter 5, where we used all sky monitors to define states:

- the 3–10 keV flux increases with Γ_1 in hard and intermediate states and reaches a peak at Γ_1 ~2.5–2.6. For softer observations, it decreases again, so that the 3–10 keV flux in the hard state and in the softest observations is comparable.
- The 10–50 keV flux does not depend on the spectral shape below the spectral break for $\Gamma_1 \lesssim 2.5$, consistent with our inability to use the Swift-BAT and Fermi-GBM instruments to distinguish soft and intermediate states (Sect. 5.2.6 and 2.1.5) and with the small differences in spectral shapes between hard and intermediate states as seen by INTEGRAL-ISGRI in state-resolved spectra (Sect. 6.2.2).
- the 3–50 keV flux is actually smaller in the softest than in the hard observations.

The same behavior can be observed when considering the flux values against Γ_2 instead of Γ_1. The 10–50 keV flux remains stable for $\Gamma_2 < 2.0$ and only decreases for $\Gamma_2 > 2.0$. According to the correlations shown in Fig. 4.3, $\Gamma_1 \approx 2.5$ and $\Gamma_2 \approx 2.0$ are corresponding values, and the results are consistent.

At any given values of Γ_1, the source flux in the 3–50 keV band can vary by as much as a factor of >2. Flux variations at the same spectral shape in the 3–10 keV and 10–50 keV bands are slightly smaller, but still very pronounced.

Reciprocally, the same 3–50 keV flux can correspond to very different spectral shapes: Figure 4.6 shows four spectra which all have about the same 3–50 keV flux, but vary between very hard with $\Gamma_1 \approx 1.6$ and very soft with $\Gamma_1 \approx 3.0$.

4.3 Orbital variability of absorption

4.3.1 Orbital variability as seen by RXTE

Transient absorption dips at or close to superior conjunction ($\phi_{\mathrm{orb}} \approx 0$) have been found already in early observations of Cyg X-1, e.g., by Li & Clark (1974) who observe a dip of at least 30 min duration[7] (see also further early results with different instruments by Mason et al., 1974; Parsignault et al., 1976; Pravdo et al., 1980; Remillard & Canizares, 1984; Kitamoto et al., 1984). More recent studies with RXTE-ASM (Bałucińska-Church et al., 2000; Poutanen et al., 2008; Boroson & Vrtilek, 2010) and Chandra (Miškovičová et al., 2013) as well as preliminary results from the RXTE campaign (Hanke, 2011) have confirmed the strong orbital variability of the absorption in Cyg X-1.

Here, we use the empirical broken power law models of Sect. 4.2, which offer the so far best description of the data, in order to investigate this variability in more details following Hanke (2011), but with more data especially in the soft states and employing a slightly better modelling of the data. Figure 4.7 shows the orbital coverage of the data used in this work; note the uniformity of the coverage for both, observations requiring and not requiring a disk component.

When comparing the N_{H} of the models with and without the disk for the *same* observation, N_{H} is larger when using the disk for all but 25 of the 2741 total observations. This can easily be understood, since both components are driven by the same spectral range (the first few used PCA bins) and an increase in N_{H} can compensate for the presence of a disk component. When discussing the orbital variability we will therefore have to treat observations that do require a disk and observations that do not require a disk separately.

A further effect to be taken into account is a correlation between N_{H} and Γ_1: a larger N_{H} can compensate a steeper spectrum and vice versa (e.g., Suchy et al., 2008). However, this is mainly a problem for individual observations and for absolute values, while here we are interested in general trends as apparent in a large sample. Note also that in previous work (e.g., Hanke, 2011) no lower limit for N_{H} was set, resulting in unphysical values that were lower than the known absorption along the line of sight to the source of $\sim 4.8\times 10^{21}\,\mathrm{cm}^{-2}$ (Xiang et al., 2011).

---

[7] I.e., of the typical duration of an obrit-wise RXTE spectrum discussed in this work.

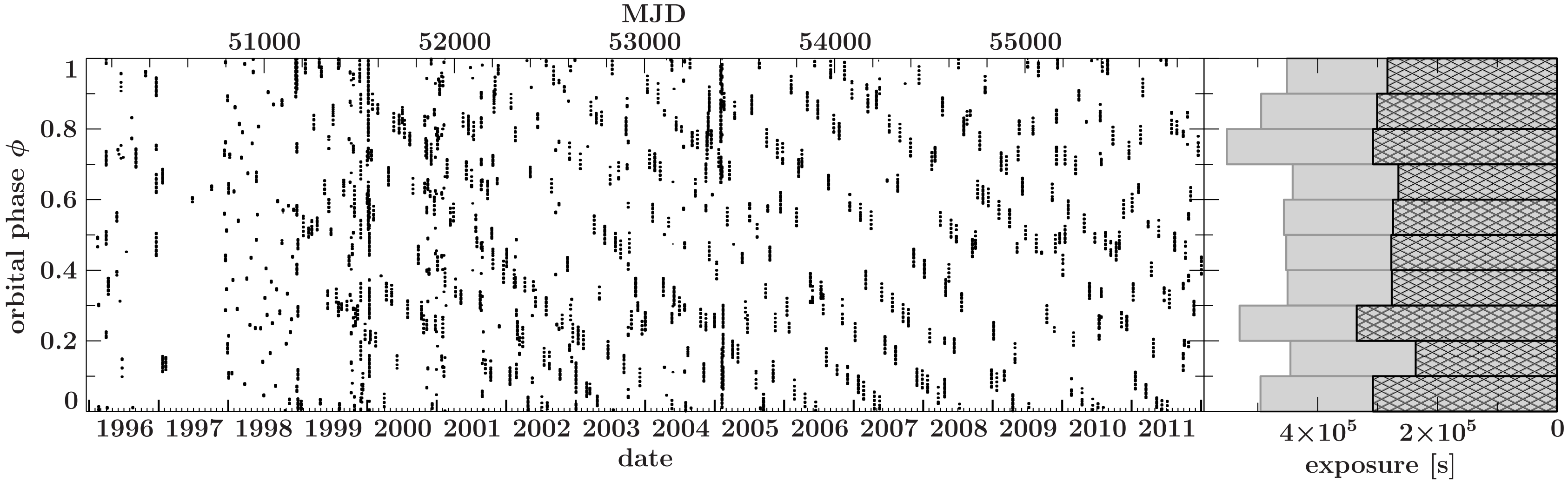

Figure 4.7: All RXTE observations of Cyg X-1 and their orbital coverage. The top-left to bottom-right diagonal pattern arises because the spacing of the individual observations in the bi-weekly observational campaign corresponds to roughly ~2.5 binary orbits of ~5.6 days (Gies et al., 2003). Histograms on the left represented the total exposure time at a given orbital phase interval. Total exposures of all observations are shown in grey and the parts of the exposure that corresponds to the observations that do not require a disk are hatched in black.

Figure 4.8 shows how the measured N_H depends on the orbital phase for three cases: all observations that do not require a disk, all observations that do require a disk and all observations that do not require a disk and fall into the long hard state from MJD 53900 to MJD 55375 (period IV, see Sect. 5.2.1). Orbital variability can be seen in observations without a disk by naked eye. Median/averahe values and the standard deviation reveal such variability also in the observations that do require a disk component. Uncertainties on N_H are much larger when a disk is added to the model and the values generally tend to be larger, implying that absolute values of both, absorption and disk parameters, have to be treated with caution in these cases. During the long hard state, the modulation is especially clear and does hardly show any instances that run into the limit of $4.8\times10^{21}\,\mathrm{cm}^{-2}$.

4.3.2 Comparison to stellar wind theory

While the resolution and the systematics of the PCA data prevent us from using more complex absorption models, the orbital variability implies that the material causing part of the absorption has to be local to the system, i.e., most likely the stellar wind of the companion.

For a qualitative comparison, we show the wind density of the toy model of Gies & Bolton (1986b) in Fig. 4.9: the model is based on the theoretical work on radiation driven winds in X-ray binaries of Friend & Castor (1982), who predict that if star close to filling its Roche lobe (as HDE 226868 is) the stellar wind will be highly asymmetric and focused towards the compact object. The models of Friend & Castor (1982) and the observational results of Gies & Bolton (1986a) agree that bulk of the emission forms within a cone of $\theta < 20^\circ$ with θ the angle away from the axis joining the companion star and the black hole. Therefore, within $\theta < 20^\circ$ the longitudinal density variations are modeled and outside, a sphrerical wind with the values at $\theta = 20^\circ$ is assumed.

While we again stress that a direct comparison of the N_H values obtained from RXTE with model predictions cannot be direcly undertaken, we see a general agreement in the sense that the superior conjunction ($\phi_\mathrm{orb} = 0$) corresponds to the highest measured average N_H values and the line of sight going through the densest regions of the wind close to HDE 226868, while the the inferior conjunction ($\phi_\mathrm{orb} = 0.5$) corresponds to the lowest average N_H and the line of sight going through the less dense parts of the wind.

The model for the stellar wind density does, however, not take into account possible clumping of the stellar wind in massive stars – a phenomenon not yet fully theoretically understood even in single stars, but supported by a large scope of observational evidence (see Sundqvist et al., 2012, for a concise review). Clumping here means that the bulk of the material is concentrated in cool dense clumps with larger regions of rarefied material between them.

In Cyg X-1, the clumps manifest themselves as dips in X-ray light curves, i.e., strong decreases in the soft X-ray count rates. In Fig. 4.8 we can observed two effects at superion conjunction: an overall increase of the baseline value for N_H (especially pronounced in the long, hard state shown on the lower left panel) and individual very high absorption

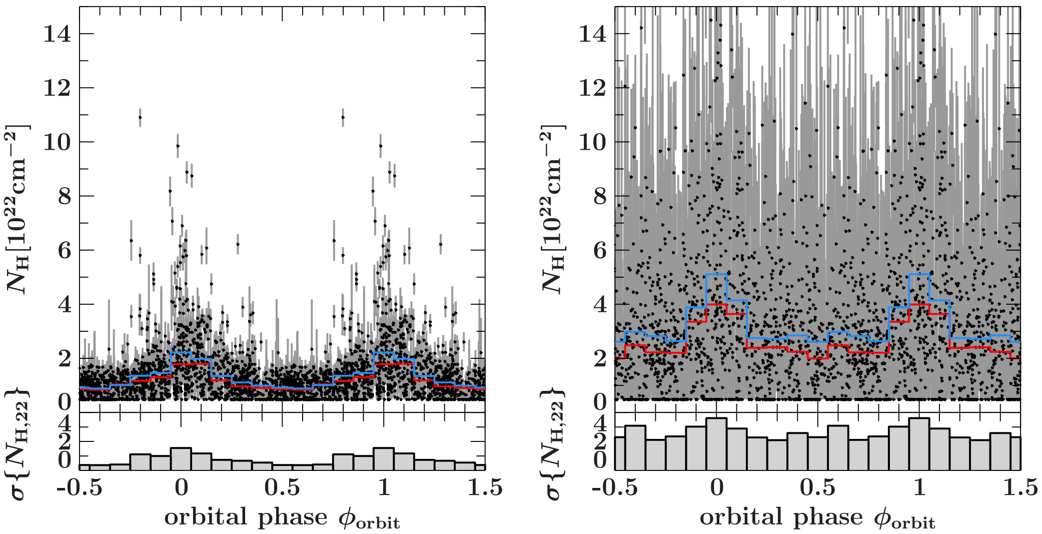

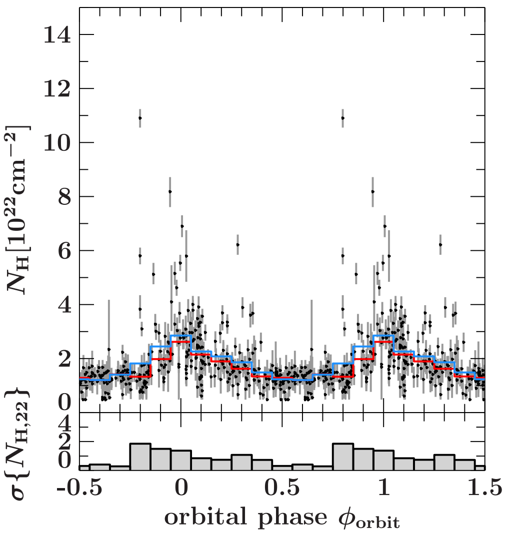

Figure 4.8: Orbital dependency of the N_H values for 1537 model fits without a disk black body component (*upper left*) and 1204 model fits with a disk component (*upper right*) as well as the observation during the long, extraordinarily hard states that do not require a disk (period IV, 321 observations, *lower left*). Shown are also the average (blue) and median (red) values of N_H as well as the standard deviation, $\sigma\{N_H\}$, of all column density measurements in every orbital phase bin.

episodes (note especially the individual N_H-values of $> 4\times10^{22}\,\mathrm{cm}^{-2}$). Theory still struggles with a detailed description of clumpy winds in X-ray binaries, but see, e.g., Oskinova et al. (2012) and especially the variability of the total optical depth along the orbit shown in their Figs. 7 and 8, that qualitatively agrees with presented observations of Cyg X-1.

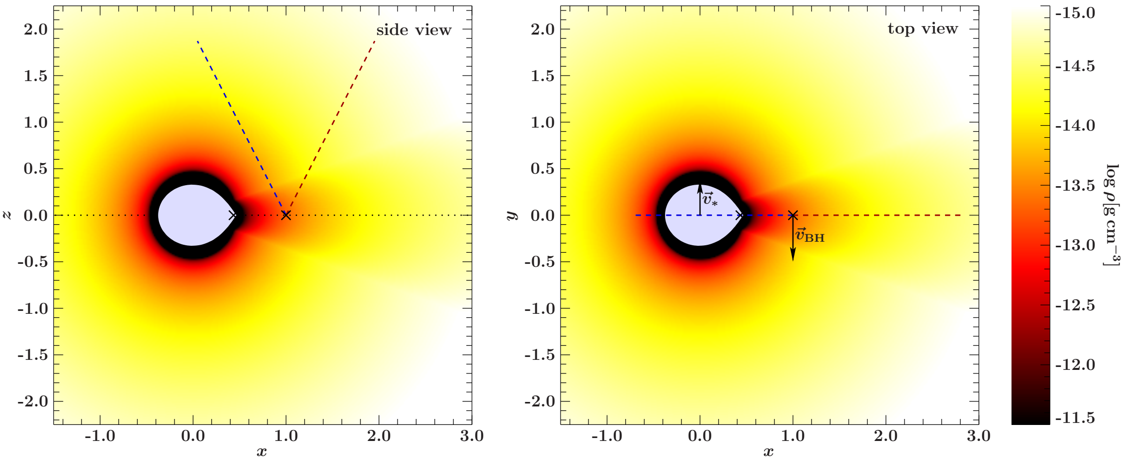

Figure 4.9: Stellar wind density of Cyg X-1 system assuming the focused wind model of Gies & Bolton (1986b). Lines of sight to the system are represented by dashed lines: for superior conjunction ($\phi_{\mathrm{orb}} = 0$) in blue and for inferior conjunction ($\phi_{\mathrm{orb}} = 0.5$) in red. The black hole and the center of mass are represented by crosses. Note that the shape of HDE 226868 is distorted due to the presence of the companion. *Left:* Side view of the binary system, orbital plane represented by dotted line. *Right:* Top view of the binary system. Figure adapted from Miškovičová et al. (2013).

4.4 Summary

In this Chapter we have addressed the spectral evolution of Cyg X-1 as seen in pointed RXTE observations. We have employed an empirical broken power law model and have confirmed the correlations seen by Wilms et al. (2006) between the different constituents of the model, but with a much larger data set with a better coverage of soft states. Constraints on the behavior of the cut off are challenging because of the missing hard X-ray coverage with HEXTE in the last years of RXTE lifetime. We expect this to be a limiting factor for the planned analysis of the soft states with more physical Comptonization models.

We emphasize that the X-ray flux of Cyg X-1 cannot be easily used to define states of the source, since Cyg X-1 shows a wide range of spectral state at the same 3–50 keV flux. Especially, the flux in the 10–50 keV range is in the same range in the hard and intermediate states – consistent with the fact that we could not use the Swift-BAT (Sect. 5.2.6) and Fermi-GBM (Sect. 5.2.7) hard all sky monitors to define the hard and intermediate states of the source.

We show that even although the observations were not originally made with this purpose, the pointed RXTE observations can be used to probe the orbital variability of the stellar wind of HDE 226868. Modeling the absorption and not using the same N_{H} value for all orbital phases is decisive for proper description of the spectra of Cyg X-1. Generally, more absorption is seen during the superion conjunction, when the line of sight passes closer to the HDE 226868 and therefore through the denser parts of its wind. More detailed studies and quantitative comparisons with models/simulations of the clumpy stellar wind are forthcoming.

Essentially, all models are wrong, but some are useful.

(Box & Draper 1987)

5 State definitions with all sky monitors

WE HAVE presented near real time analysis of Cyg X-1 and H1743−322, as the sources were undergoing state transitions in Chapter 3. These often elusive changes in spectral and timing properties are of special interest, since they correspond to major changes in the accretion geometry (see Sect. 1.2 and 1.3). The time coverage of pointed observations with RXTE (mostly bi-weekly monitoring) is however not enough for a proper statistics of states, since transitions can happen on timescales as short as hours (Böck et al., 2011; Axelsson et al., 2005). Additionally, state definitions are required to be able to interpret observations with instruments lacking broadband coverage, such as XMM, Chandra, INTEGRAL (see applications of the methodology developed here in Sect. 6), or radio and infrared measurements. In the following, we therefore use Cyg X-1 as an example and develop a all sky monitor based state classification that does not require simultaneous broadband coverage and agrees between different all sky monitors, enabling long term studies over time periods longer than the lifetime of individual satellites. This Chapter is based on a publication in 'Astronomy and Astrophysics' (Grinberg et al., 2013)[1] and in large parts is taken in verbatim from there.

As a persistent source Cyg X-1 (see also Sect. 1.4) does not cover the full q-track: its bolometric luminosity changes only by a factor of ∼3–4 between the states (Wilms et al., 2006, and references therein) and its spectrum is never fully disk-dominated. The frequent state transitions (sometimes very fast – within hours, see, Böck et al., 2011) mean that the source often crosses the jet line. Since these state changes are thought to be associated with significant changes in the accretion flow geometry and energetics, a knowledge of the source state is crucial for interpreting all (multiwavelength) observations of Cyg X-1 and its donor star. A typical example is the study of the stellar wind of HDE 226868, which during soft states is strongly photoionized by the radiation from the vicinity of the black hole (Gies et al., 2008).

---

[1] The paper is listed as one of the highlights of the A&A volume 554, see `http://www.aanda.org/index.php?option=com_content&view=article&id=936&Itemid=292`.

Between 1996 and 2012, state information was readily available using the All Sky Monitor on the Rossi X-ray Timing Explorer (RXTE-ASM) and regular pointed monitoring observations. Here, various state definitions exist, which use, e.g., measured count rates and/or colors (e.g., Remillard, 2005; Gies et al., 2008), or sophisticated mapping between these measurements and spectral parameters (e.g., Ibragimov et al., 2007; Zdziarski et al., 2011b). The former prescription is easy to use, but is very instrument-specific and cannot be translated easily to other X-ray all sky monitors. The latter approach requires a sophisticated knowledge of the instrumentation of all sky monitors, as well as of the detailed spectral modeling. Furthermore, the previously used state definitions are all slightly inconsistent among themselves. In this work we introduce a novel approach to classify states of Cyg X-1 using the all sky monitors RXTE-ASM, MAXI, Swift-BAT, and Femi-GBM based on 16 years of pointed RXTE observations. Our aim is to find an easy-to-use prescription for determining the states that is as consistent as possible between these instruments in order to facilitate long-term studies that are longer than lifetime of individual monitors. We start with a description of our data reduction approach in Sect. 5.1. Section 5.2 comprises the actual state mapping from pointed RXTE observations to RXTE-ASM, Swift-BAT, MAXI, and Fermi-GBM, including a discussion of the precision of state determinations attainable with these instruments. We summarize and discuss our results in light of the statistics of the state behavior of Cyg X-1 in Sects. 5.3 and 5.4.

5.1 Observations and data analysis

5.1.1 ASM data

We considered all 97556 RXTE All Sky Monitor (ASM, Sect. 2.1.1) measurements of Cyg X-1 performed during the lifetime of RXTE. We first filtered for measurements where the background was clearly oversubtracted (count rates r_A, r_B, or $r_C < 0$). The quality of the ASM data started deteriorating after about MJD 55200 (early January 2010): valid pointings are fewer and the overall variance of the measurements becomes larger (Fig. 5.1). Since the larger variance could be source intrinsic, we analyzed the ASM light curve of a source known to be roughly constant at the level of precision required here, the Crab (Wilson-Hodge et al., 2011): after MJD 55200 the Crab light curve shows prolonged gaps (Fig. 5.2). Where data exist, the average values of the ASM count rate (calculated on a 10 d timescale), which were stable at ~75 cps before, decrease by up to 10%. The variance of the data strongly increases by a factor of ~10. The ASM hardness (between the C and A bands) increases from stable values around ~0.95 to up to ~1.4 and shows higher variability. Both the timescale of this change in behavior and the similar behavior of the light curves of other sources during the same time period imply that we do not see the long-term variability of the Crab nebula as has been observed by Wilson-Hodge et al. (2011) here, but truly instrumental decline during the last years of the ASM lifetime.[2]

---

[2] Vrtilek & Boroson (2013) come to similar conclusions regarding ASM data from 2010 on and report gain changes in the last two years of ASM lifetime as a possible cause.

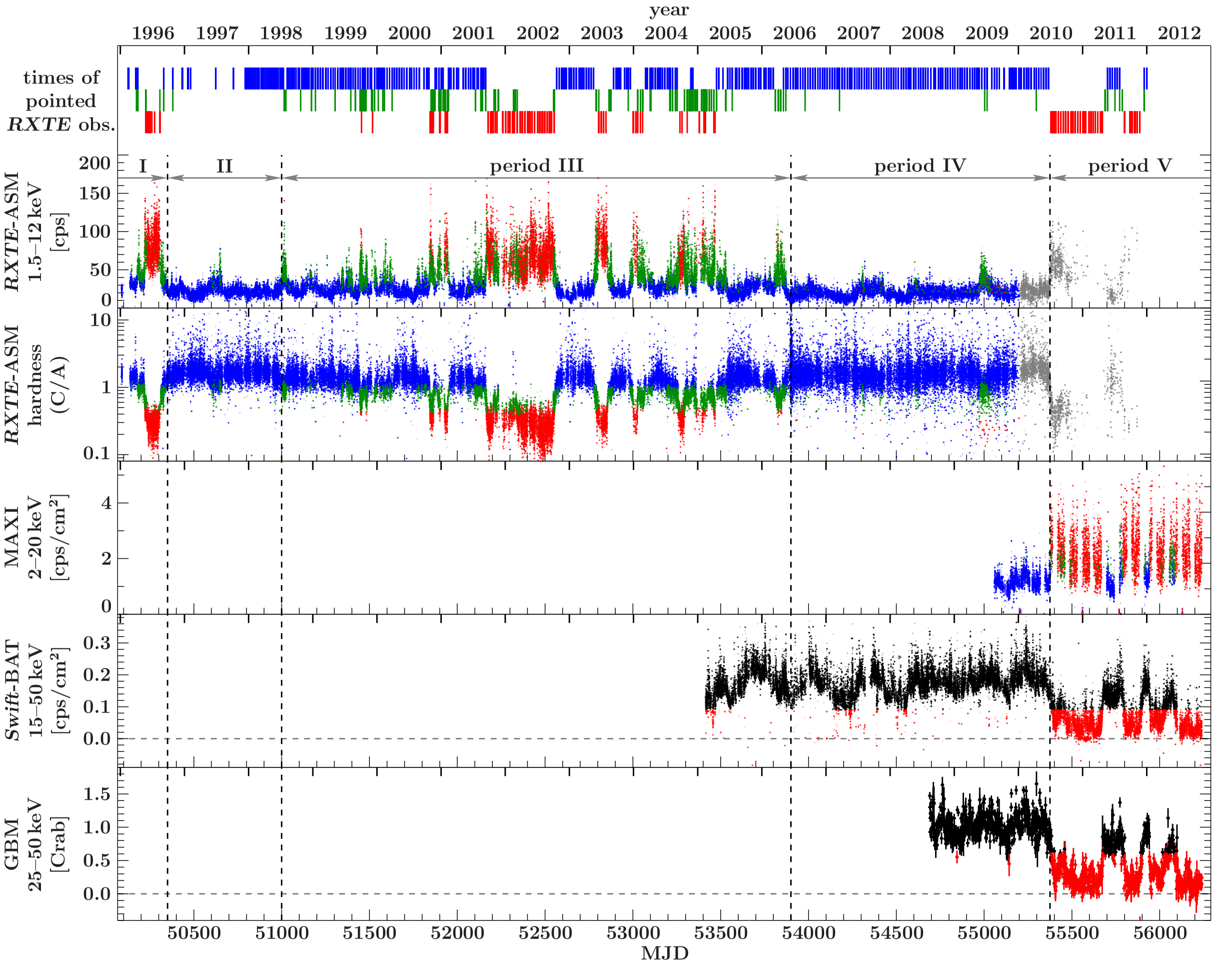

Figure 5.1: Pointed RXTE observations and all light curves (RXTE-ASM, MAXI, Swift-BAT, and GBM) of Cyg X-1 used in this analysis. ASM, MAXI, and BAT data are shown in the highest available resolution, GBM are binned daily. ASM hardness is calculated by dividing count rates in band C (5.0–12 keV) by count rates in band A (1.5–3.0 keV). Vertical dashed lines and horizontal arrows represent periods of different source activity patterns (Sect. 5.2.1). Blue, green, and red colors represent states of individual measurements classified using the respective classification for the different instruments as introduced in Sect. 5.2: blue represents the hard state, green the intermediate state and red the soft state. ASM data after MJD 55200 (in gray) are affected by intrumental decline. Hard and intermediate states cannot be separated in BAT and GBM; BAT and GBM data corresponding to these periods of hard or intermediate states are therefore shown in black.

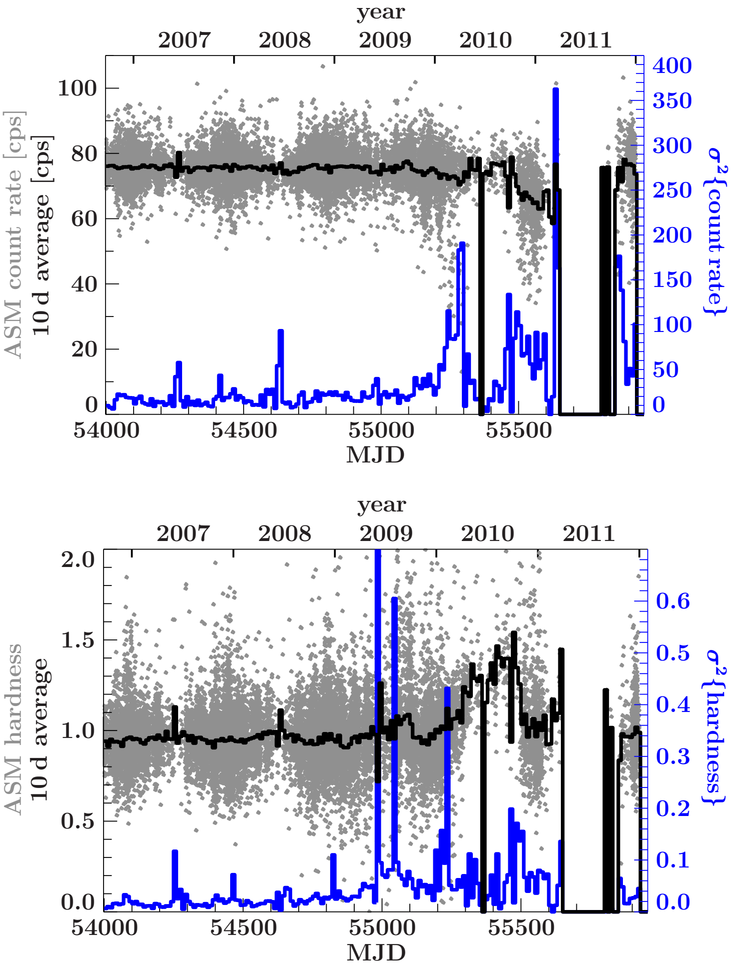

Figure 5.2: Crab ASM light curve (upper panel, 1.5–12 keV, gray points) and hardness (lower panel, 5.0–12 keV/1.5–3.0 keV, gray points) with the respective 10-day average values (black histograms) and variances (blue histograms).

The ASM data measured post January 2010 can still be used to assess trends with large changes in count rate; however, for the following analysis, which relies on absolute values of both count rate and hardness, we ignore all ASM data after MJD 55200. Overall, we used 94068 individual ASM measurements corresponding to 80082 individual times (a source can be in the field of view of two SSCs simultaneously) spanning over 5000 days from MJD 50087 (1996 January 5) to MJD 55200 (2010 January 4).

5.1.2 Pointed RXTE observations

For spectral analysis we consider the same pointed RXTE observations as we have introduced in Sect. **??** and refer to this Section for details of data extraction and treatment.

Where possible due to the available PCA modes, light curves with a time resolution of 2^{-9} s ($\sim$2 ms) were extracted for timing analysis, choosing the same energy bands as Böck et al. (2011): a low-energy band corresponding to energies 4.5–5.7 keV (channels 11–13) and a high-energy band corresponding to energies 9.4–14.8 keV (channels 23–35; energy conversion for epoch 5). Calculation of the rms and X-ray time lags follows Nowak et al. (1999). We used segments of 4096 bins; i.e., we calculated the root mean square variability (rms) between 0.125 and 256 Hz.

For two simultaneous, correlated light curves, such as the high- and low-energy light curves of Cyg X-1 used here, one can calculate a Fourier frequency dependent time lag between the two from the Fourier phase lag at any given frequency (Nowak et al., 1999, and references therein). In our calculations a positive time lag means that the light curve in the hard energy band is lagging the soft. The timelag depends strongly on Fourier-frequency and shows a complex variation with state see (see Pottschmidt et al., 2000 for examples and note that we use the same frequency binning in the relevant frequency range). To obtain a single value that serves as a good signature for the overall level of the lags, we average it over the frequency range of 3.2–10 Hz (see Pottschmidt et al., 2000, 2003).

5.1.3 Swift-BAT, MAXI, and Fermi-GBM data

RXTE was switched off on 2012 January 5 (MJD 55931). To continue the monitoring of the long term behavior of Cyg X-1 we therefore need to use other instruments. The all sky monitor available in the soft X-ray band at the time of writing is MAXI, the hard X-rays above 10 keV are covered by Swift-BAT and Fermi-GBM.

MAXI is an all-sky monitor onboard the Japanese module of the International Space Station (Matsuoka et al., 2009). Light curves from the Gas Slit Camera detector (GSC) are available in three energy bands (2–4 keV, 4–10 keV, and 10–20 keV) on a dedicated website[3]. MAXI light curves show prolonged gaps of several days due to observational constraints.

Swift-BAT is sensitive in the 15–150 keV regime (Barthelmy et al., 2005). Satellite-orbit averaged light curves in the 15–50 keV energy band from this coded mask instrument are available on a dedicated website [4].

The Gamma-ray Burst Monitor (GBM; von Kienlin et al., 2004; Meegan et al., 2007) onboard Fermi observes the sky in the hard X-ray and soft γ-ray regimes (about 8 keV to $\sim$30 MeV). It permanently provides complete coverage of the unocculted sky. Because of its strongly limited spatial resolution, the brightness of individual sources cannot be determined directly and so the Earth occultation method is applied (Case et al., 2011; Wilson-Hodge et al., 2012). In this work we use the publicly available quick-look Fermi GBM Earth occultation results provided by the Fermi GBM Earth occultation Guest Investigation teams at NASA/MSFC and LSU[5], which consist of light curves with a 1 d resolution in four energy bands between 12 keV and 300 keV (12–25 keV, 25–50 keV, 50-100 keV, and 100–300 keV) starting from MJD 54690. On average each measurement of Cyg X-1 is based on 18 occultations.

As these data are prescreened by the respective instrument teams, no further selection criteria were applied, and we used all data available from the start of the each mission until MJD 56240, resulting in 36454 individual measurements for BAT, 9794 for MAXI,

---

[3] `http://maxi.riken.jp/top/index.php?cid=1&jname=J1958+352`

[4] `http://swift.gsfc.nasa.gov/docs/swift/results/transients/`

[5] `http://heastro.phys.lsu.edu/gbm/`

and 1443 for GBM (Fig. 5.1).

5.2 Identifying the states of Cygnus X-1

5.2.1 General source behavior

The different periods of source activity and therefore the different population of the individual source states strongly affect our ability to distinguish the regions that the respective states occupy on hardness-intensity diagrams (HIDs) or in other spaces. As a first step for our analysis we therefore present an overview of the light curves used for this work and over the ASM 5–12 keV to 1.5–3 keV hardness (Fig. 5.1).

The source behavior from early 1996 (RXTE launch) until the end of 2004 has been discussed by Wilms et al. (2006), who used a crude definition of ASM based states using only the count rate. This classification is sufficient to distinguish main activity patterns, and also consistent with more detailed studies (Zdziarski et al., 2011b). We extend this earlier work and supplement the ASM data with BAT, MAXI, and GBM. By eye, i.e., without using the state definitions introduced later in this section and shown in color in Fig. 5.1, we are able to distinguish five main periods with different source activity patterns:

- a pronounced soft-state episode in 1996 (up to ~MJD 50350, period I);
- one and a half years of a mainly stable hard state with only short softenings, seen as spiky features in Fig. 5.1, between the end of 1996 and early 1998 (~MJD 50350–51000, period II);
- a series of failed state transitions and soft states that started in early 1998 (see Pottschmidt et al., 2003) and included a prolonged, very soft period between the end of 2001 and the end of 2002. This activity period continued until mid-2006 (~MJD 51000–53900, period III);
- an almost continuous hard state from mid-2006 to mid-2010, which includes the hardest spectral states ever observed in Cyg X-1 (see Nowak et al., 2011, for examples; ~MJD 53900–55375, period IV);
- a series of prolonged soft states that followed an abrupt state transition at around MJD 55375 and continued during the writing of this paper (>MJD 55375, period V).

Periods I to III are fully, and period IV is almost fully covered by the ASM. Some ASM data exist during period V, but are affected by problems described in Sect. 5.1.1 and therefore excluded from our analysis. During period IV the ASM hardness shows higher variability than in previous hard states, but the same effect is also seen in the hardness of the Crab and is instrumental (Fig. 5.2).

BAT coverage started at the end of period III on MJD 53414 (mid-February 2005) and continues during the writing of this paper. Thus, BAT data are available during soft states, namely in period V, but simultaneous coverage of soft states by BAT and ASM is lacking.

GBM and MAXI coverage started MJD 54690 (2008 August 12) and MJD 55058 (2009 August 15), respectively, and was going on when this paper was written. These instruments mainly cover the final phase of period IV and the ongoing period V. No simultaneous coverage with ASM exists during the intermediate and soft states, except during the phase of ASM deterioration.

During the joint coverage by ASM and BAT, Cyg X-1 displayed two softening episodes, which did not reach a stable soft state (~MJD 53800–53900 and around MJD 55000). Both episodes are clearly visible in the ASM band but not in the BAT light curve. This is a remarkable contrast to the full state transition of ~MJD 55375, which is associated with a clear drop in the BAT count rate simultaneous with an increase in the ASM count rate. Similar softenings visible in the soft X-ray band but not in the hard band have been observed in 1997–1999 by Zdziarski et al. (2002), who discuss changes seen in the ASM where no corresponding changes were observed in the 20–300 keV band with BATSE. Only further long-term observations in both soft and hard X-rays can help decide whether only successful state transitions are accompanied by a change in hard X-ray flux and whether the behavior of the hard component above 15–20 keV can be used to decide whether a state transition will fail or not.

Reliable ASM data are lacking after MJD 55200. The BAT light curve suggests that while the source left the soft state for short periods of time, those hard periods were softer than the prolonged hard states in periods II and IV.

A striking feature of the hardness during the hard states are values that exceed the average by a factor of ~5 and more (Bałucińska-Church et al., 2000; Poutanen et al., 2008). They correspond to so-called X-ray dips, where blobs of cold material in the line of sight cover the source. Since it is virtually impossible to decide whether an individual ASM dwell was measured during a dip, we do not treat these data separately for the purpose of this paper (but see Boroson & Vrtilek, 2010).

5.2.2 Γ_1-defined states

In this Chapter, we use the spectral fits introduces and discussed in detail in Chapter 4, in particular, the soft photon index, Γ_1, that we and others (e.g., Pottschmidt et al., 2003; Wilms et al., 2006; Böck et al., 2011; Nowak et al., 2011) have shown to have strong correlations with other spectral and timing parameters on timescales from hours to years across the whole range of its values and therefore to be a good proxy for the spectral state.

Figure 5.3 shows the dependency of the total rms between 0.125 and 256 Hz in both-high and low-energy bands and the time lag (averaged between 3.2 and 10 Hz) on Γ_1. The timing and spectral behavior is clearly related, but is complex with changes in both slope and sign. For clarity in the plot we do not show error bars; however, the uncertainity of single measurements is close to or smaller (much smaller in the case of the hard observations) than the spread of the correlation at any given frequency. The value of $\Gamma_1 \sim 2$, where spectral models with a disk become dominant, corresponds to a bend in the timing correlations. Another clear kink can be seen at $\Gamma_1 \sim 2.5$.

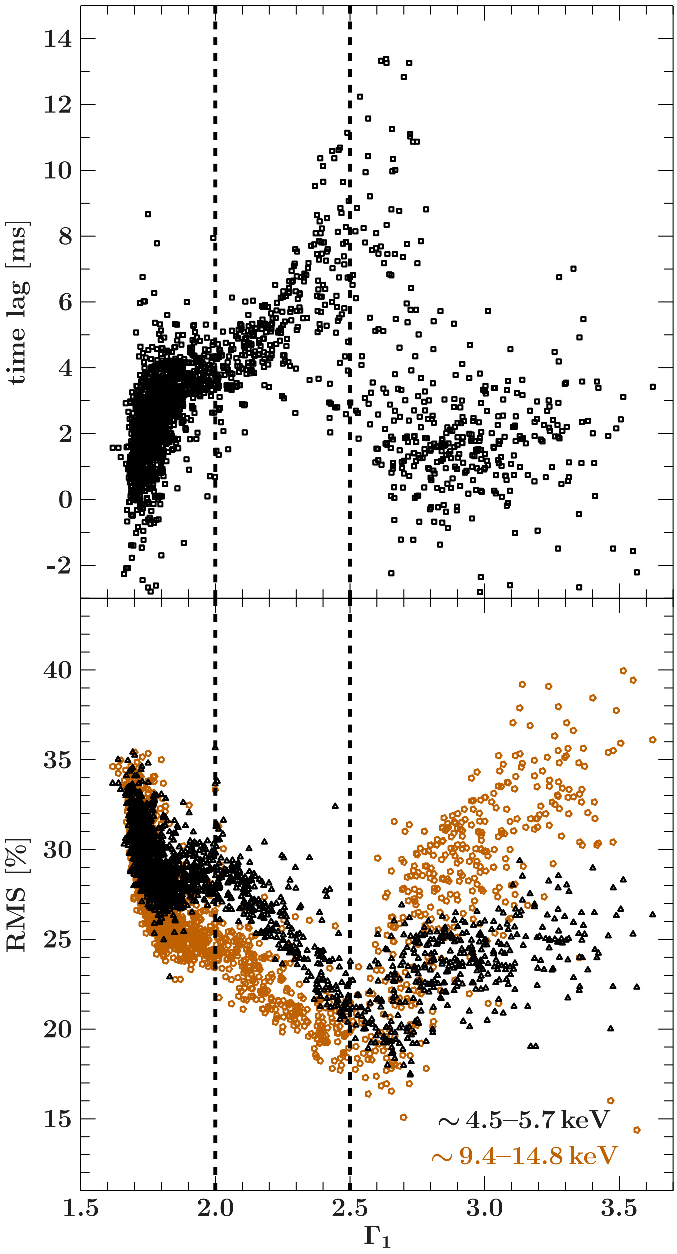

Figure 5.3: X-ray time lag and fractional RMS as a function of the soft photon index Γ_1.

We use both our spectral and timing analysis results to define Γ_1 ranges for different source states that are characterized by spectral and timing behavior that is similar within a state but different between the three states. Hard states correspond to $\Gamma_1 < 2.0$, intermediate states correspond to $2.0 < \Gamma_1 < 2.5$, and soft states correspond to $\Gamma_1 > 2.5$.

5.2.3 Simultaneous ASM mapping

For direct classification of the ASM data, we use the 1424 instances when ASM observations of Cyg X-1 are simultaneous with spectra from pointed RXTE observations, i.e.,

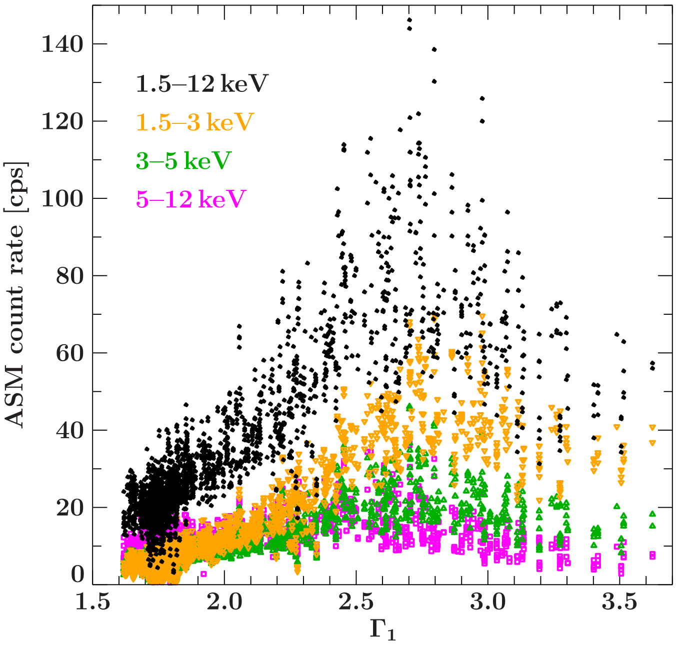

Figure 5.4: Dependency of the ASM count rate in different bands on the soft photon index Γ_1 of simultaneous pointed RXTE observations. Shown are total ASM counts (1.5–12 keV, black dots) and counts in the three ASM energy bands: band A (1.5–3 keV, orange upside down triangles), band B (3–5 keV, green triangles), and band C (5–12 keV, magenta squares).

Table 5.1: Spearman's rank correlation coefficients ρ between the ASM counts and the soft photon index Γ_1

Energy band [keV]	1.5–12	1.5–3.0	3.0–5.0	5.0–12
ρ ($\Gamma_1 < 2.7$)	0.77	0.81	0.76	0.62
ρ ($\Gamma_1 > 2.7$)	−0.60	−0.54	−0.55	−0.68

Values of Γ_1 from pointed RXTE observations; ρ calculated for the cases $\Gamma_1 < 2.7$ and $\Gamma_1 > 2.7$ in the three individual ASM bands.

fall within the good time intervals used for the orbit-wise spectral extractions. This corresponds to 2400 individual ASM measurements since the source is often observed by more than one SSC. We treat the measurements of different SSCs independently for the actual mapping since instrument alignment onboard RXTE would otherwise introduce a bias towards a higher number of ASM measurements with Cyg X-1 in the field of view of two SSCs during pointed observations of Cyg X-1.

Figure 5.4 shows the dependency of the ASM count rate from individual ASM-SSC dwells on the soft photon index Γ_1 of the broken power law fits. Because of the use of individual ASM SSC dwells, an RXTE spectrum, hence a Γ_1-value, can correspond to more than one simultaneous ASM measurement. While the ASM count rate in all bands is correlated with Γ_1, this correlation is not unique: it appears to change sign at $\Gamma_1 \sim 2.7$ (Table 5.1). Consistent with this observation, Zdziarski et al. (2011b) note that on several instances in the soft state their derived bolometric flux is lower than during the high-flux hard state[6].

---

[6] Zdziarski et al. (2011b) define the soft state according to a power-law photon index deduced from the ASM count rates. This approach does not exactly correspond to the approach chosen here, however, it is similar enough to allow rough comparisons.

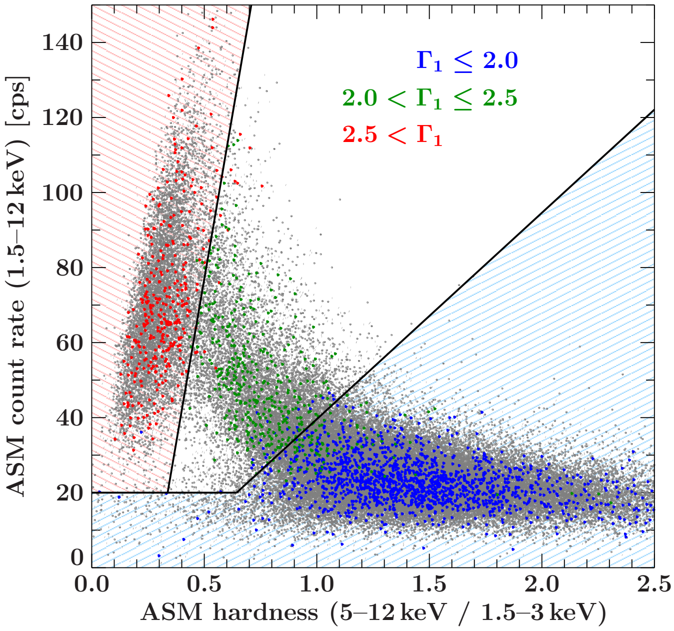

Figure 5.5: PCA to ASM mapping. Gray data points are all ASM measurements of Cyg X-1 in the shown range. Blue points represent PCA defined hard states, green intermediate and red soft states. Black lines show the cuts defining the states in the ASM HID. The light blue shaded region corresponds to the position of the hard state in the HID, the light red shaded to the position of the soft state. The intermediate state region is shown without shading.

Thus, cuts in ASM count rate alone cannot separate the states.

The Γ_1-based definition of states introduced in Sect. 5.2.2 results in in 1608 ASM measurements in the Γ_1-defined hard state, in 455 ASM measurements in the Γ_1-defined intermediate state, and in 337 ASM measurements in the Γ_1-defined soft state. Each of the states primarily populates a well-defined distinct area in the ASM HID (Fig. 5.5). A visual inspection reveals that neither cuts in hardness alone nor cuts in count rate alone yield a good division between the states. The softest observations tend to have count rates in the transitional state range (~40–50 cps), the hard state area extends to low hardnesses usually associated with transitional or even soft states, and the hard and transitional states strongly overlap both in ASM hardness and count rate. To account for these features, we choose the following ansatz: an ASM observation with count rate c and (5–12 keV/1.5–3 keV) hardness h is defined as hard if $c \leqq 20$ cps regardless of the hardness. For $c > 20$ cps the cuts between the states are defined by linear functions of the form

$$c_{\mathrm{ASM}} = m_{\mathrm{ASM},i} \cdot (h - h_{0,i}) \tag{5.1}$$

where $i \in \{\mathrm{hard}, \mathrm{soft}\}$. The line with slope $m_{\mathrm{ASM,hard}}$ and x-intersection $h_{0,\mathrm{hard}}$ divides the hard and the intermediate states, and the line with slope m_{soft} and intersection $h_{0,\mathrm{soft}}$ divides the intermediate and the soft states, respectively.

We determine the best division between the states such that the fractional contamination of the ASM-defined states by different Γ_1-defined states is minimized. Contamination here is defined for the hard state (and accordingly for soft and transitional states) as the fraction of all measurements classified as hard using the ASM that is classified as transitional or soft according to Γ_1. Initial fits indicate that good separations of the states are achieved for $h_{0,\mathrm{hard}} \sim h_{0,\mathrm{soft}}$. We therefore reduce the number of free parameters for the cuts and set

$$h_{0,\text{hard}} = h_{0,\text{soft}} = h_0. \tag{5.2}$$

For the best cuts we obtain $h_0 = 0.28$, $m_\text{hard} = 55$, and $m_\text{soft} = 350$ (Fig. 5.5 and Table 5.2). The contamination by other Γ_1-defined states is <5% for the hard state, <10% for the intermediate state and <3% for the soft state. Note that since the source behavior changes continuously from one state to the other, such that the states do not represent three distinct, fully independent regimes, we do not expect a perfect separation of the states (e.g., Wilms et al., 2006). The spread in count rate and hardness is amplified by the orbital and superorbital modulations of Cyg X-1 and by dips (e.g., Poutanen et al., 2008). The stronger contamination of the intermediate state is expected: as a transitional state between the hard and the soft state, it is short-lived and confined by two divisional lines. The separation between the hard and the intermediate state appears especially unclean; we therefore advise to treat the classification cautiously when an observation is close to this cut.

To test our approach we compare the ASM-based behavior with the results of the spectro-timing analysis of the quick, observationally exceptionally well covered intermediate to soft transition presented by Böck et al. (2011). In particular, we can recover the moment of the transitions at slightly before MJD 53410.

5.2.4 Non-simultaneous ASM mapping

In general, an all sky monitor and a pointed instrument will not observe a source at the same time, so that we need to assess how well a given monitor pointing can be used to characterize the source state during a non-simultaneous observation. For every RXTE spectrum we consider ASM measurements within 1.5 h intervals $\Delta t = \pm(0\text{–}1.5)$ h, $\pm(1.5\text{–}3)$ h, $\pm(3\text{–}4.5)$ h, etc., up to 48 hours. The length of the intervals is motivated by the length of the RXTE orbit of ~1.5 h, during about half of which Cyg X-1 is visible. For simultaneous ASM measurements with different SSCs we use the average for all subsequent analysis. We obtain 135901 pairs of ASM and RXTE state classifications (the same ASM measurement may be used to classify several RXTE spectra, if the RXTE spectra are close enough). For each delay interval and for each ASM defined state, we determine the percentage of spectra with a different RXTE classification.

Figure 5.6 shows that this contamination remains stable for the hard state for up to ~48 h. For the soft state, the contamination reaches 20% for a 48 h delay and is even greater for the intermediate state, which also shows a very strong increase within the first ~10 h. Strictly simultaneous data, which were discussed in Sect. 5.2.3, are not taken into account here, resulting in higher starting contaminations. The results are similar when using positive or negative delays only. The trends are expected, because the hard state often occurred in long, stable stretches during the RXTE lifetime, while the intermediate state is short lived due to its transitional nature.

Table 5.2: Overview over all sky monitor based state definitions for Cyg X-1.

State	ASM-based[a]	MAXI-based[b]	BAT-based[c]	GBM-based[d]
hard	$c \leq 20 \vee c \leq 55 \cdot (h - h_0)$	$c_\mathrm{M} \leq 1.4 \cdot h_\mathrm{M}$	...[e]	...[f]
interm.	$c > 20 \wedge 55 \cdot (h - h_0) < c \leq 350 \cdot (h - h_0)$	$1.4 \cdot h_\mathrm{M} < c_\mathrm{M} \leq 8/3 \cdot h_\mathrm{M}$	...[e]	...[f]
soft	$c > 20 \wedge c > 350 \cdot (h - h_0)$	$8/3 \cdot h_\mathrm{M} < c_\mathrm{M}$	$c_\mathrm{B} \leq 0.09\,\mathrm{counts\,cm^{-2}\,s^{-1}}$	$f \leq 0.6\,\mathrm{Crab}$

[a] With ASM 1.5–12 keV count rate c in counts s^{-1} , ASM (5–12 keV/1.5–3 keV) hardness h, and $h_0 = 0.28$. [b] With MAXI 2–4 keV count rate c_M in counts s^{-1} and MAXI (4–10 keV/2–4 keV) hardness h_M. [c] With BAT normalized 15–50 keV countrate c_B in counts $\mathrm{cm}^{-2}\,\mathrm{s}^{-1}$. [d] With daily GBM 25–50 keV flux f. [e] Distinguishing between hard and intermediate states is not possible based on BAT light curves alone. The source is defined as in BAT-based hard *or* intermediate state for $c_\mathrm{B} > 0.09\,\mathrm{counts\,cm^{-2}\,s^{-1}}$. [f] Distinguishing between hard and intermediate states is not possible based on GBM daily light curves alone. The source is defined as in GBM-based hard *or* intermediate state for $f > 0.6\,\mathrm{Crab}$.

Table 5.3: Time Cyg X-1 spent in the different states (hard – H, intermediate – I, soft – S) as measured by the RXTE-ASM, Swift-BAT, MAXI, and Fermi-GBM all sky monitors.

Period[a]	MJD	RXTE-ASM			MAXI			Swift-BAT		Fermi-GBM	
		H	I	S	H	I	S	H & I	S	H & I	S
I	50087[b]–50350	37%	19%	44%	...	...	...	...	...	...	...
II	50350–51000	99%	1.0%	0%	...	...	...	...	...	...	...
III	51000–53900	63%	20%	17%	...	...	...	...	...	...	...
IV	53900–55375	97%[d]	2%[d]	<1%[d]	...	...	...	99%	1%	...	...
V	55375–56240[c]	...	...	...	17%[e]	8%[e]	75%[e]	40%	60%	23%[f]	77%[f]

Between MJD 50087 and 55200, Cyg X-1 spent a total of 75.6% of its time in the hard state, 12.8% in the intermediate state, and 11.6% in the soft state as measured with ASM.

Percentages are only shown if at least most of the period is covered by the respective instrument. [a] Periods defined in Sect. 5.2.1. [b] Start of period I defined by the start of the RXTE-ASM measurements. [c] The end of period V is defined by the availability of data at the time of writing. [d] ASM data only until MJD 55200. [e] MAXI data affected by gaps in the light curve. [f] Daily average values are used for GBM.

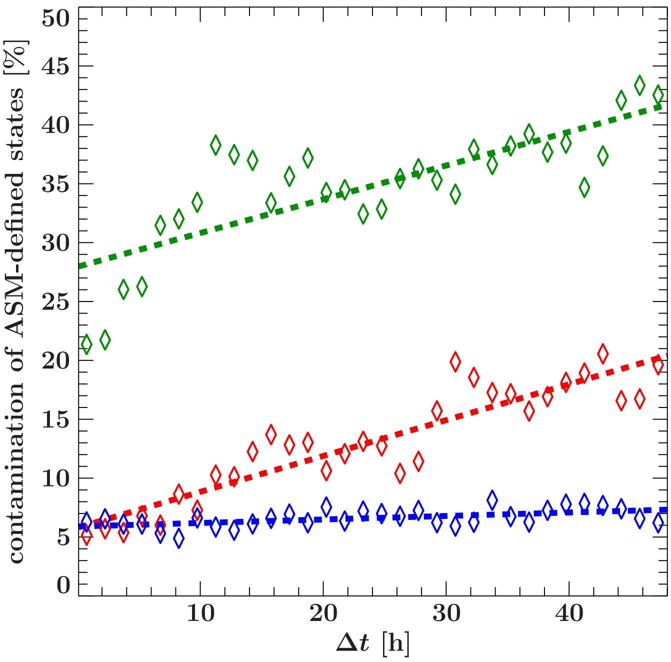

Figure 5.6: Percentage of contamination of the ASM defined states (hard state shown in blue, intermediate in green, and soft in red) for time delays $\Delta t = \pm(0\text{–}1.5)\,\mathrm{h}$, $\pm(1.5\text{–}3)\,\mathrm{h}$, $\pm(3\text{–}4.5)\,\mathrm{h}$, etc., between the ASM and the pointed RXTE measurements. Simple linear fits to the data are shown as dashed lines to illustrate the overall trends.

5.2.5 MAXI mapping

Since only 37 MAXI measurements are strictly simultaneous with pointed RXTE data, we use MAXI data within $\Delta t = 1\,\mathrm{h}$ before and after a pointed RXTE observation and obtain 219 MAXI measurements with Γ_1-based state classifications, which offer a better overall statistics with 107 hard states, 101 soft states, and 11 intermediate states. Increasing Δt to 2 h does not yield a better coverage of the intermediate state, neither does attempting to map ASM onto MAXI, since a simultaneous coverage by the two instruments is only available during the end of period IV.

To find the best approach for defining MAXI-based states, we considered all possible different combinations of count rates measured with MAXI (the three energy bands as introduced in Sect. 5.1.3 and the overall count rate) and different combinations of hardness measures within the MAXI bands. The clearest separation can be achieved when using the ratio between count rates in the medium (4–10 keV) and the low (2–4 keV) MAXI bands (MAXI-hardness, h_{MAXI}) and the count rate in the low (2–4 keV) MAXI band, c_{MAXI}, as done in Fig. 5.7. The MAXI 4–10 keV/2–4 keV hardness is also the closest correspondence to ASM hardness we can achieve using publicly available MAXI light curves.

The sparse coverage of the intermediate state makes it hard to separate the three basic states. Given that the hard and the soft states populate distinct parts of the MAXI HID (see Fig. 5.7) and knowing the shape of the cuts in the ASM HID, we separate the states by two linear functions of the form

$$c_{\mathrm{MAXI}} = m_{\mathrm{MAXI},i} \cdot h_{\mathrm{MAXI}}, \tag{5.3}$$

where $i \in \{\mathrm{hard}, \mathrm{soft}\}$, m_{hard} separates the hard and the intermediate states and m_{soft} separates the intermediate and the soft states. The absence of an x-intersection and of

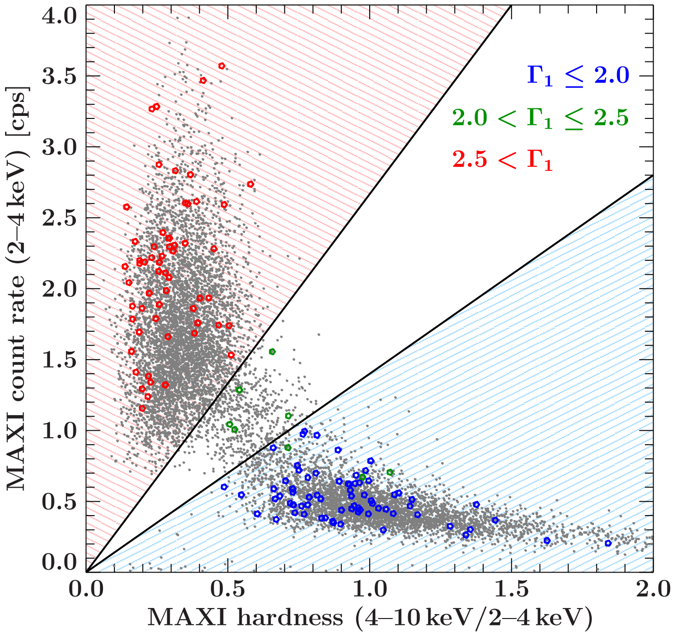

Figure 5.7: PCA to MAXI mapping. Gray data points are all MAXI orbitwise measurements of Cyg X-1 in the shown energy range. Blue circles represent Γ_1-defined hard states, green intermediate states and red soft states. Black lines define the state cuts. The light blue shaded region corresponds to the hard state in the MAXI HID, the light red shaded region to the soft state, and the region without shading to the intermediate state.

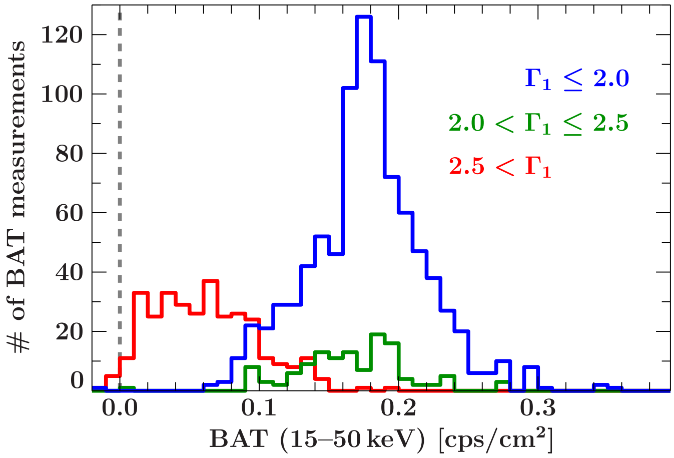

Figure 5.8: Histogram of BAT fluxes of Γ_1-defined states. The hard state is shown in blue, the intermediate state in green, and the soft state in red.

a threshold count rate value is motivated by the lower number of classified data points compared to the ASM HID, which also prevents us from direct fits for m. The best values obtained by eye are $m_{\mathrm{MAXI,hard}} = 1.4$ and $m_{\mathrm{MAXI,soft}} = 8/3$ (Table 5.2).

For a reader interested in performing her own classification using MAXI data, we note that these are conservative cuts in the sense that we obtain the purest intermediate state possible here. As in the case of RXTE-ASM we expect the separation between the hard and intermediate states to be especially unclean.

5.2.6 BAT mapping

Swift-BAT light curves in different energy bands are not readily available. Since BAT also does not cover soft X-ray energies where the contribution of the accretion disk becomes important as the spectrum softens, we use only the light curves in the standard 15–50 keV band for our analysis and therefore do not perform a two-dimensional mapping.

Since only 290 BAT measurements are strictly simultaneous with pointed RXTE data, we employ the same approach as for MAXI (Sect. 5.2.5) and use BAT data within $\Delta t = 1\,\mathrm{h}$ before and after the RXTE spectrum to obtain 1339 BAT measurements with an RXTE based state classification: 895 in the hard state, 124 in the intermediate state, and 320 in the soft state.

Figure 5.8 shows the histogram of the BAT fluxes in the different states. While the soft and hard state clearly show different BAT fluxes, the intermediate states populate the same region as the hard ones. The BAT measurements, therefore, do not enable us to separate the hard and the intermediate states. The soft state can still be identified by a cut at a BAT area-normalized count rate of $c_\mathrm{BAT} = 0.09\,\mathrm{counts\,cm^{-2}\,s^{-1}}$ For BAT count rates below c_BAT, Cyg X-1 is in the soft state, for fluxes above it in the hard or intermediate states (Table 5.2). The contamination by the other state is ~7% in both cases.

We also considered an ASM to BAT mapping where we classified BAT data by using the closest ASM measurements if one exists within ±0.5 h around the BAT measurement in order to increase the number of data points with classification. No simultaneous good ASM and BAT data are available in the soft state (see Fig. 5.1 and Sect. 5.1.1). The histograms of the hard and intermediate states follow the trends apparent from Fig. 5.8: it is not possible to separate the two states using BAT flux.

5.2.7 GBM mapping

Since GBM light curves are publicly available only in daily bins, strictly simultaneous mapping between RXTE spectra and GBM is not possible. We therefore define an RXTE spectrum as simultaneous to a GBM measurement if the good time interval used to extract the spectrum lies within the GBM measurement. If all simultaneous RXTE spectra show the same state, the GBM measurement is classified as belonging to this state. If the states of the RXTE spectra differ, the GBM measurement is not classified.

The 104 GBM measurements with simultaneous RXTE observations include on average 3.8 (reaching from 1 to 8) individual RXTE spectra. Only 6 out of the 104 measurements are unclassified due to state ambiguities. The remaining valid classifications include 61 hard states, 3 intermediate states, and 34 soft states. All 6 unclassified measurements include hard and intermediate state classifications. There were no GBM measurements including both intermediate and soft, or hard and soft RXTE spectra. The distribution of these results is consistent with Cyg X-1 spending most of the time covered by GBM observations in stable hard and soft states. That six out of nine GBM measurements including a Γ_1-defined intermediate state also include Γ_1-defined hard states reflects the high variability and instability of the intermediate states.

We first consider GBM HIDs. These show a clear separation in two regions: a region with mainly soft and a region with hard and intermediate observations, which are clearly separated in GBM flux alone. We therefore consider only GBM fluxes and calculate histograms of GBM fluxes of Γ_1-defined states. The best separation between the states can be

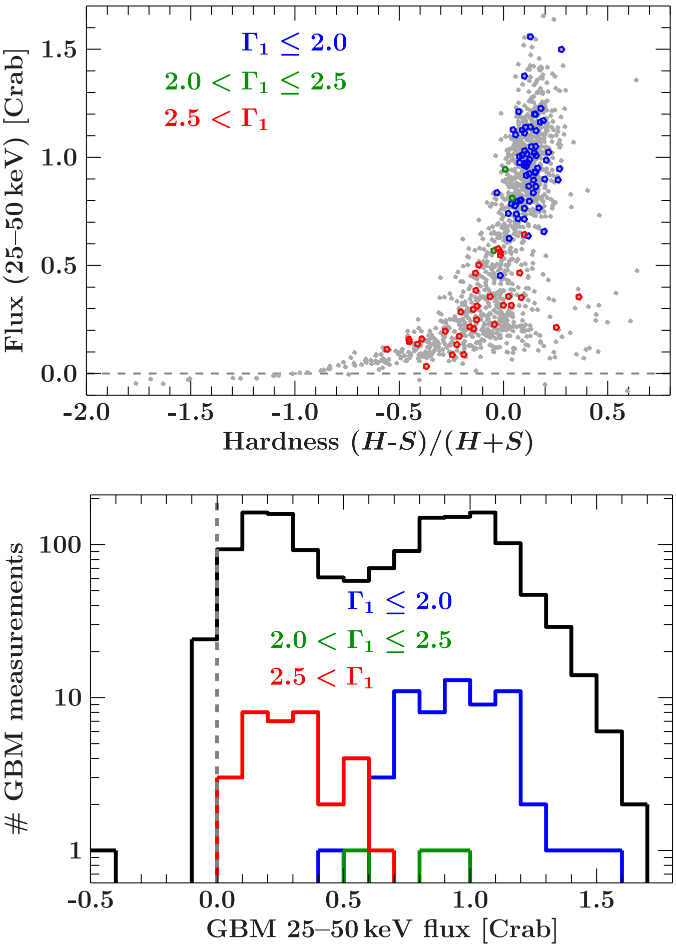

Figure 5.9: *Top panel:* Daily GBM HID. S denotes the 12–25 keV flux, H the 25–50 keV flux. The gray dashed line denotes the zero flux level. Total GBM measurements are shown in gray. *Bottom panel:* Histogram of daily GBM fluxes of Γ_1-defined states. The hard state is shown in blue, intermediate state in green, and soft state in red. Total GBM measurement are shown in black. The gray dashed line denotes the zero flux level.

achieved when using 25–50 keV fluxes (Fig. 5.9). While hard and intermediate states cannot be separated, the soft state can be divided from the other two by a cut at a GBM flux of 0.6 Crab: for fluxes <0.6 Crab the source is in the soft state, for fluxes ≥0.6 Crab in hard or intermediate state (Table 5.2). We do not give values for contamination here because of the long integration times of the GBM and because we excluded states where we know the source to change the Γ_1 defined state during one GBM measurement. We also note that since the hard and intermediate states cannot be distinguished using GBM, we did not introduce additional bias into our classification by not including GBM-measurements with simultaneous RXTE spectra in both hard and intermediate states.

5.3 The states of Cyg X-1

5.3.1 The statistics of Cyg X-1 states

Using the classification from the different instruments derived in the previous sections, we can assess the activity pattern during the different periods defined in Sect. 5.2.1. A detailed breakdown of the occurrence of different states is given in Table 5.3.

Period I contained a prolonged soft state, and the source spent twice as much time in soft state as in the intermediate state during this time. We lack all sky monitor coverage before MJD 50087, and therefore do not know whether this soft period observed was a part of a longer series of soft states. In period III the source spent as much time in the intermediate state as in the soft state, in accordance with the observation of multiple failed state transitions (e.g., Pottschmidt et al., 2003). Periods II and IV showed similar activity patterns dominated by a long, stable hard state, although data from the ASM were already affected by deterioration of the instrument in period IV (Sect. 5.2.1). The state classifications based on the ASM and the BAT agree well for period IV.

The disagreement between the statistics derived from Swift-BAT and MAXI classification for period V first seems worrisome. A visual inspection of Fig. 5.1 indicates, however, that this mismatch may be due to the gaps in the MAXI light curve. Indeed, out of the 7794 BAT measurements that fall into MAXI gaps (defined here as times when the interval between two MAXI measurements is larger than 6 h), 3876 are hard or intermediate and 3918 are soft, while 60% of all BAT measurements during period V are soft. MAXI gaps therefore fall more often into hard/intermediate states than into soft states during this period, and the difference seen in Table 5.3 is due to the incomplete MAXI coverage. MAXI data can therefore be used to determine states at certain times, but not to investigate the overall frequency of the occurrence of different states. A similar caution also applies to the GBM. Here, the disagreement between the GBM data and other instruments is partly due to the use of daily light curves, where the short-term variability is averaged out (Fig. 5.1). This can be directly seen from the higher resolution BAT data. Using individual BAT points during period V, 60% of all measurements are classified as coming from the soft state (Table 5.3). Classifying the daily BAT fluxes, however, increases the fraction of soft states to 68%, which is consistent with the GBM considering the uncertainties in both the GBM- and BAT-based definitions (Figs. 5.8 and 5.9). Data with a time resolution <1 d are therefore crucial for a reliable state classification.

Summarizing these observations, we estimate the typical inter-instrument systematic error of the state determination to be better than 10% for the post-RXTE instruments.

5.3.2 Stability of states

Section 5.3.1 highlights that the different states are clearly different in their stability. While the source tends to remain in the hard and the soft states for a prolonged time, not unexpectedly the intermediate state is far more unstable. This well known general behavior can be quantified using the RXTE-ASM data, i.e., the data set in our measurements that covers the longest time span, does not have gaps, and can be reliably used to define all three states.

To calculate the state statistics, we calculate the probabilities that Cyg X-1 has changed its state after a certain interval and that the source remained in the same state throughout this interval for each ASM data point measured at a reference time, t_{ref}. More formally, we calculated the transited fraction, P_{trans}, i.e., the probability that an observation made a certain time *after* the reference observation will find Cyg X-1 in a different

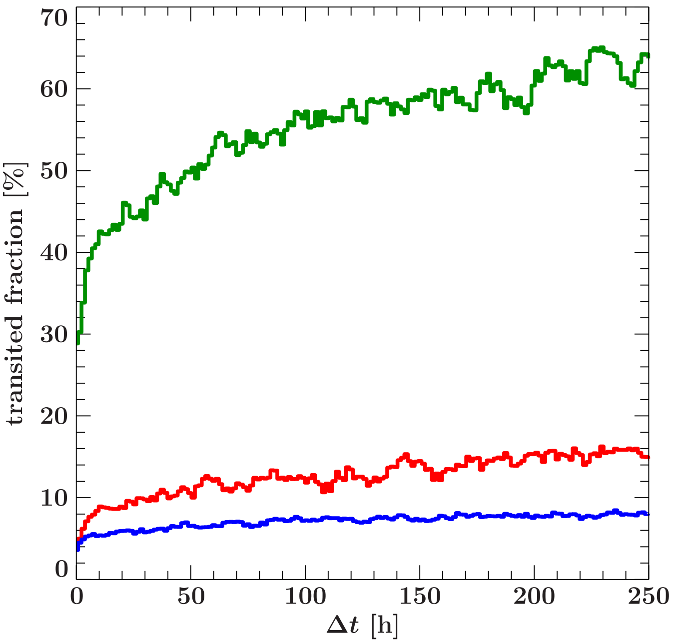

Figure 5.10: Probability, P_{trans}, that the source state is found changed a time interval Δt after a previous state determination for the different states (blue: hard; green: intermediate; red: soft) using ASM data.

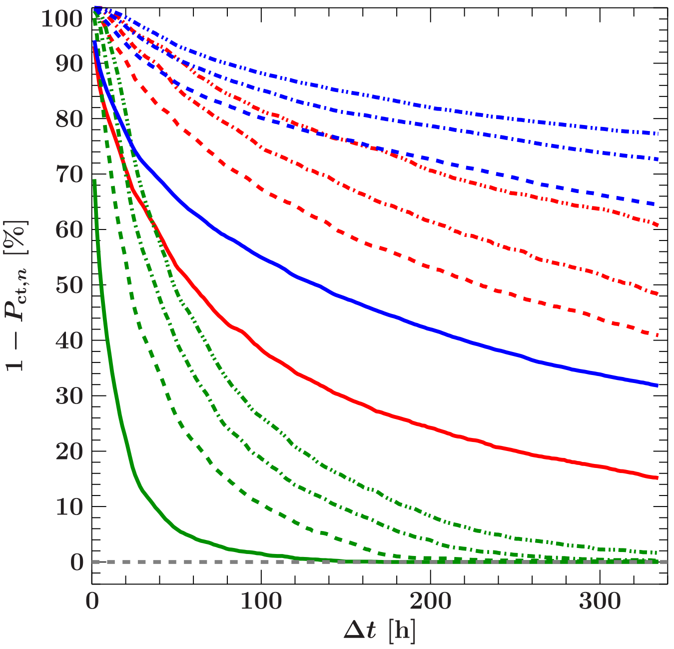

Figure 5.11: The probability, $1 - P_{\mathrm{ct},n}$, that the source has remained in the same state (blue: hard; green: intermediate; red: soft) for at least the time Δt for different values of n of ignored number of possible outliers/misclassifications ($n = 0$: solid; $n = 4$: dashed; $n = 8$: dot-dashed; $n = 12$: dot-dot-dashed). The gray dashed line represents 0.

source state (Fig. 5.10). The probability that the source state is unchanged is $1 - P_{\mathrm{trans}}$. We determined P_{trans} by calculating the fraction of all measurements in a different state than the reference measurement made at times t_i with $\Delta t_1 \leq t_i - t_{\mathrm{ref}} < \Delta t_2$ where $\{\Delta t_1, \Delta t_2\} \in \{\{0\,\mathrm{h}, 1.5\,\mathrm{h}\}, \{1.5\,\mathrm{h}, 3.0\,\mathrm{h}\}, \{3.0\,\mathrm{h}, 4.5\,\mathrm{h}\}, \ldots\}$. This approach is equivalent to the one employed in Sect. 5.2.4, where we used RXTE spectra as reference measurements.

The transited fraction, P_{trans}, does not take into account the possibility that the source might have undergone state changes between t_{ref} and t_i. To address this possibility we calculated the cumulative transited fraction, $P_{\mathrm{ct},n}$, which measures the probability that at least one source transition has happened up to a time interval Δt after the reference measurement. In order to assess the influence of possible outliers and/or misclassifications, we defined a state transition by the existence of more than $n \in \{0,\ldots,12\}$ measurements in a different state than the reference measurement in the time interval $t_{\mathrm{ref}} \leq t < t_{\mathrm{ref}}+\Delta t$. The probability that the source has remained in the same state for at least a time Δt is then given by $1 - P_{\mathrm{ct},n}$ (Fig. 5.11).

As expected from a simple look at the light curves (see Fig. 5.1), hard states are the most stable states: in more than 90% of all cases, the source is still in the hard state 200 h after a given hard state ASM measurement (Fig. 5.10). In over 30% of all cases, a period of 300 h after any given hard state measurement will not contain even a single measurement in a different state. This number increases to over 70% for larger n, i.e., when very short excursions to the soft/intermediate state and/or outliers due to misclassifications are ignored (Fig. 5.11).

Although less stable and shorter than hard states, soft states generally show similar behavior. Even for $n = 0$, a significant number of soft state measurements are not followed by a state transition within 300 h, i.e., prolonged stable, soft states lasting more than 12 days exist. Such states are observed by ASM in periods I and III (Fig. 5.1). MAXI and BAT data suggest an increased occurrence of such stable soft states also in period V.

The intermediate state behaves differently. The transited fraction strongly increases within the first few hours. Already fifty hours after a reference intermediate measurement about half of the measurement will show the source in a different state. The cumulative transited fraction approaches 100% even for $n = 12$ at 300 d (Fig. 5.11). Intermediate states are therefore short and unstable compared to hard and soft states.

5.4 Summary

Based on pointed RXTE observations, we have provided criteria to define X-ray states (hard, intermediate, and soft) using light curves from all sky monitor instruments. In particular we have shown that:

- due to the complex source behavior, simple state definitions based just on the source count rate or just on the hardness do not adequately describe states;
- a combination of RXTE-ASM total count rate and hardness can be used to define states before MJD 55200 (see Table 5.2 for exact cut);
- the best separation of states is achieved with simultaneous ASM data. Data within $\Delta t \pm 6$ h result in a contamination of <10% for the hard and soft states and <30% for the intermediate state;
- a combination of MAXI count rate and hardness can be used to define states (see Table 5.2 for exact cuts);
- soft coverage is needed to define states and the lack of such does not allow the hard and the intermediate states to be distinguished using publicly available BAT

light curves. BAT light curves can, however, be used to distinguish the soft state from hard/intermediate states: the source is in the soft state below a threshold of 0.09 counts $\mathrm{cm}^{-2}\,\mathrm{s}^{-1}$, and in the hard/intermediate state above it (Table 5.2);

- the lack of soft coverage does not allow a separation between hard and intermediate states with publicly available GBM data, with the analysis being further hindered by the low time resolution of the GBM ligh tcurve, but a rough state classification is to consider Cyg X-1 in the soft state for fluxes <0.6 Crab and in the hard/intermediate state above that threshold (Table 5.2);
- the hard state is by far the most stable state of Cyg X-1, followed by the soft state. The probability that the source remains in the hard state for at least one week (200 h) is >85% (using $P_{\mathrm{ct},12}$). Soft states are slightly less stable, but the probability of a soft state being longer than one week is still ∼75%. Intermediate states are short-lived and typically last a few days at most, implying that they can only be caught with monitor data with a time resolution of better than 1 d.

The state classification introduced here can be reliably used to define source states where no X-ray continuum spectrum measurement is available. The high frequency of all sky monitor measurements for RXTE-ASM, Swift-BAT, and MAXI enables us to catch short flares and especially quick state transitions.

> ‘When I was ten years old, all I gave my sweet-heart was a pair of projections that turned the group of rotations in four dimensions into principal bundles over the three-sphere. Ancient constructions, though I did rediscover them for myself.’
> ‘How were they received?’
> ‘She liked them so much, she extended them to larger spaces and gave me back the result. [...] So what about you?’
> ‘I've generally had more success with flowers.’
>
> *(Greg Egan, ‘Schild's Ladder’)*

6

Using all sky monitor defined state definitions for Cygnus X-1

In Chapter 5, we have developed a methodology for state classification of any given observation of Cyg X-1 using contemporary all sky monitor observations. Such a classification is decisive for interpreting individual observations and to enable state-resolved analysis of state-dependent properties such as γ-ray polarization.

In this Chapter, we use this methodology first to classify individual Chandra and XMM observations of Cyg X-1 (Sect. 6.1) with the aim to place the high resolution spectra in the context of the long-term evolution of the source and then to classify all available INTEGRAL observations with the aim of state-resolved polarization analysis and therefore possible identification of the origin of γ-ray radiation above $\sim$400 keV in Cyg X-1 (Sect. 6.2). The analysis presented in Sect. 6.1.1 was conducted for the forthcoming publication of Miškovičová et al. (2013, submitted) and the analysis presented in Sect. 6.1.2 for Duro et al. (2013, in prep.).

6.1 Defining states with all sky monitors

6.1.1 Chandra observations

Miškovičová et al. (2013) probe the orbital variability of the stellar wind by examining Chandra High Energy Transmission Grating (HETG: Canizares et al., 2005) spectra of Cyg X-1 at different orbital phanses: ϕ_{orb} $\sim$0.05 (Chandra ObsID 8525, 2008 April 18/19), $\sim$0.2 (ObsID 9847, 2008 April 19), $\sim$0.5 (ObsID 11044, 2010 January 14), $\sim$0.75 (ObsID 3815, 2003 March 4/5), and $\sim$0.95 (ObsID 3814, 2003 April 19/20, also analyzed by Hanke et al., 2009).

Such a study of the stellar wind is only feasible in the hard state of the source, since the strong X-ray radiation during the soft states completely photoionizes the wind. Even

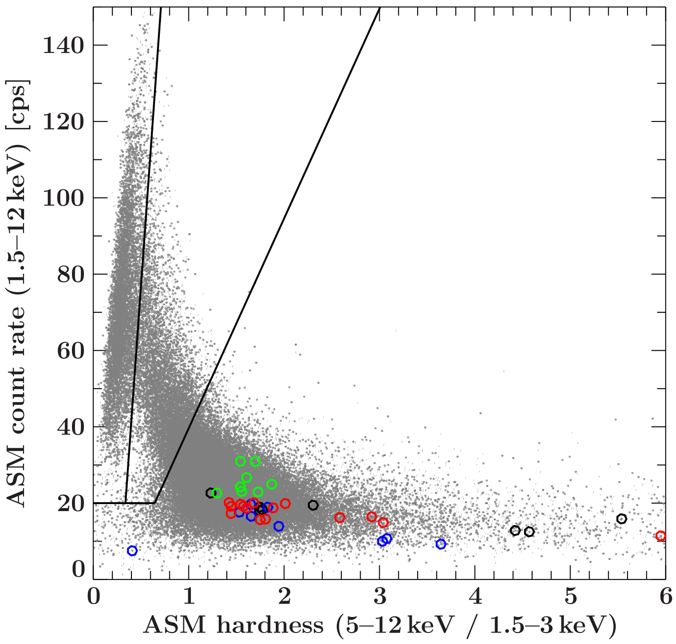

Figure 6.1: State classification for the ASM measurements during the Chandra ObsID 3814 (red circles), 3815 (green circles), 8525 (blue circles), and 9847 (black circles). Black solid lines represent the cuts between the states as introduced in Sect. 5.2.3. To illustrates the dipping behavior, higher hardness values are shown compared to Fig. 5.5.

the higher X-ray flux of intermediate states or bright hard states may influence the wind structure near the black hole.

We first address the classification of the observations based on the simultaneous ASM data. ObsID 11044 was taken during the time of ASM deterioration (Vrtilek & Boroson, 2013; Grinberg et al., 2013, see also Sect. 5.1.1) and we therefore have to use MAXI data for the assessment of this observation. The average daily RXTE-ASM values point towards similar conditions for the four other observations (ObsIDs 8525, 9847, 3815, and 3814). Strictly simultaneous individual ASM data points however show that while all four observations are in the ASM-defined hard state, ObsID 3815 differs from the remaining three (Fig. 6.1). The average count rates for OBsIDs 3814, 8525 and 9847 are 18 cps for 15 data points, 14 cps for 9 data points, and 17 cps for 8 data points, respectively. The hardness values (5–12 keV / 1.5–3 keV) cluster between 1.5 and 2, but show single instances well above 3, indicative of strong dips for these three observations. The average count rate for ObsID 3815 is higher with ~26 cps for 8 data points and the ASM light curve shows no dips.

Six MAXI measurements are simultaneous with ObsID 11044 and all show the source in the hard state. No strong changes in the hardness are visible.

All five observations are therefore in the hard state and suitable for wind studies. ObsID 3815, however, has to be treated carefully due to the higher X-ray flux and its possible effect on the structure of the clumpy wind from the companion (see Miškovičová et al., 2013, for details of the Chandra analysis of the time intervals with no dips; data taken during dips will be analyzed in a forthcoming publication by N. Hell et al.).

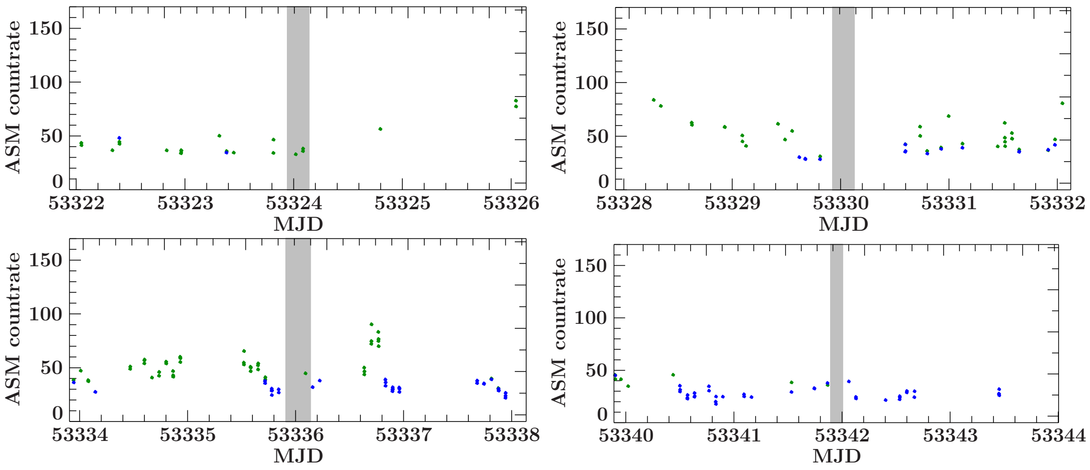

Figure 6.2: ASM light curves during and around XMM observations with ID – left to right and top to bottom – 0202760201, 0202760301, 0202760401, and 0202760501. Exact times of XMM observations are shaded gray. ASM data points are classified according to Sect. 5.2.3: blue represents the hard state, green the intermediate state.

6.1.2 XMM observations

Duro et al. (2013) analyze the broad Fe Kα reflection line in four XMM EPIC-pn observations (Strüder et al., 2001) in the modified timing mode that are simultaneous with broadband RXTE and INTEGRAL monitoring (the observations have also been previously analyzed by Fritz, 2008).

The XMM observations are $\sim$2.5–5 h in duration and were taken between November 14 and December 3 2004 during a period of frequent failed state transitions (see Sect. 5.2.1 and especially Fig. 5.1). Figure 6.2 shows ASM observations that are classified according to Sect. 5.2.3 during and around these XMM observations. Only observations 0202760201 and 0202760401 have strictly simultaneous data, in both cases Cyg X-1 was in the intermediate state. ASM measurements taken within 6 hours around observations 0202760301 and 0202760501 show the source both in hard and in intermediate state, so that a state classification is not straightforward. In all cases, the measurements are close to the cut between the hard and intermediate state, which is especially messy (Sect. 5.2.3). Given the general behavior of the source in the given time period, especially the high variability seen in all instruments employed in the spectral analysis, we therefore conclude the source to be in the intermediate state in all observations.

6.2 State-resolved analysis with INTEGRAL

6.2.1 The need for state-resolved polarization analysis

Bright and persistent, Cyg X-1 is one of the most observed X-ray binaries with INTEGRAL, both through a multi-year Key Programme and as part of the satellite calibration mainly

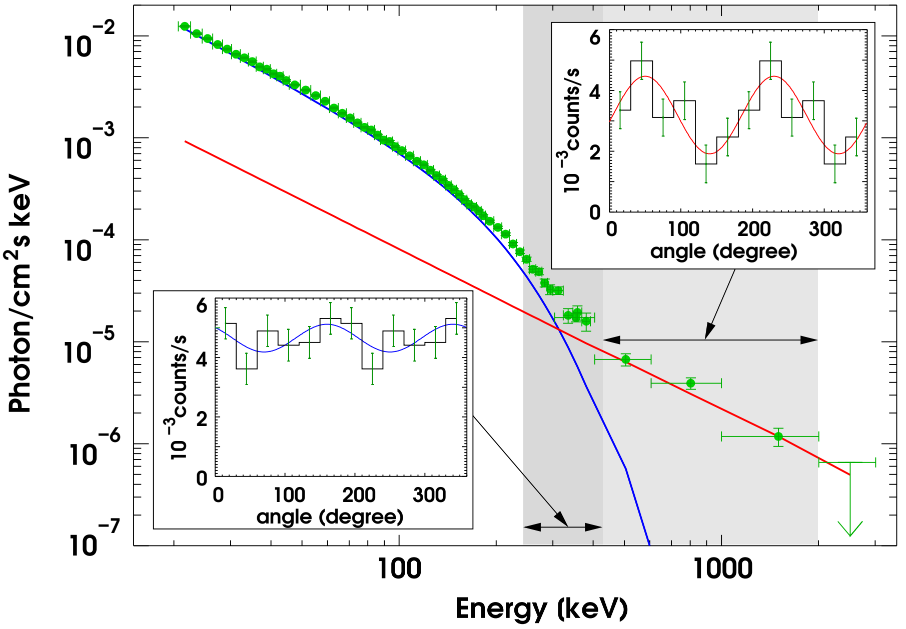

Figure 6.3: Unfolded INTEGRAL-IBIS spectrum of Cyg X-1 (ISGRI + Compton mode data). Insets show the polarization signal measured in the Compton mode data in the 250–400 keV and 400–2000 keV ranges. Figure courtesy of J. Wilms, after Laurent et al. (2011b).

in the early years of the mission. There are currently about 8 Ms gross exposure time of usable data[1].

All data[2] before 2009 (∼5 Ms gross exposure) have been used by Laurent et al. (2011b) for spectroscopic and polarimetric analysis of the source. The spectrum (Fig. 6.3, main box) clearly shows the existence of a non-thermal tail (often dubbed “hard tail”). Such a tail has been previously observed in Cyg X-1 by McConnell et al. (2000, 2002) in CGRO data, by Fritz (2008) in their simultaneous analysis of XMM, RXTE and INTEGRAL observation, and by Cadolle Bel et al. (2006) in their INTEGRAL observations during an intermediate state in 2003 June. Other sources showing such tails include, e.g., the canonical transient BHB GX 339–4 (Droulans et al., 2010). The origin of these hard tails is highly debated. In jet models (Markoff et al., 2005; Maitra et al., 2009; Nowak et al., 2011, and references therein) these high energy photons could be from synchrotron radiation. Comptonization models can produce them in a non-thermal plasma (Coppi, 1999; Malzac & Jourdain, 2000, and others) or in case of bulk motion (e.g., outflows) in the plasma (Laurent & Titarchuk, 2007). The main difference between both models is that such radiation produced by Comptonization would not be polarized, while the degree of polarization can be high under the jet paradigm, if the magnetic field is homogeneous

---

[1] some of the earliest calibration observations cannot be used for scientific purposes and are not included in these numbers and in our following analysis

[2] The screening applied in Laurent et al. (2011b) as well as in the following are an offset of maximally 10° from the center of the field of view and a minimal exposure of 1 ks in both ISGRI and PICSiT.

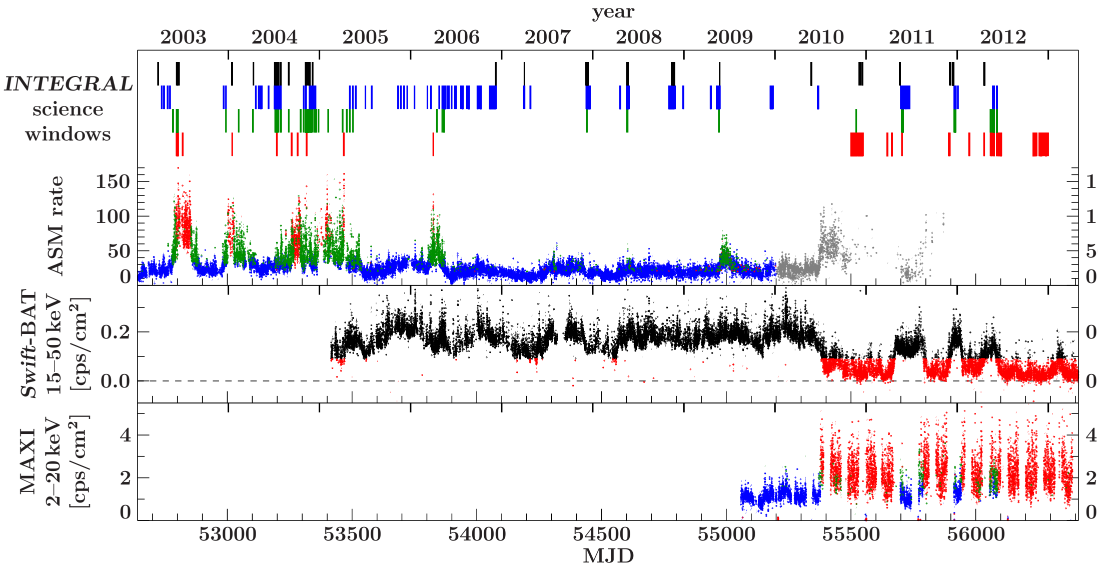

Figure 6.4: State classification of INTEGRAL science windows. ASM, BAT and MAXI data classified according to Sect. 5 (see also Grinberg et al., 2013). The colors represent different states: blue represents the hard state, green the intermediate state and red the soft state. Data for which no classification was possible is shown in black. Individual INTEGRAL science windows are represented by dashes, with different states plotted with a vertical offset for better display. For details of the classification see Sect. 6.2.2.

over the emission site.

Laurent et al. (2011b) could show that in the 250–400 keV band, i.e., where the curved Comptonization component dominates the spectrum, the radiation from Cyg X-1 is not polarized (polarization fraction $< 20\%$; Fig. 6.3, left inset). On the other hand, the polarization fraction in the 400-2000 keV range, i.e., for the hard tail, is $67 \pm 30\%$ (Fig. 6.3, right inset): *the hard tail is strongly polarized*. Note that the polarization angle cited by Laurent et al. (2011b) is erroneous due to a sign mistake and has actually to be $40^\circ \pm 15^\circ$ (Jourdain et al., 2012), although this does not change any of the conclusions of our work.[3] The result was confirmed in a fully independent analysis with the INTEGRAL-SPI instrument by Jourdain et al. (2012). Interestingly, this polarization angle is not the same as the one derived from radio observations (Stirling et al., 2001).

The high degree of polarization is a strong cue toward a synchrotron origin of the radiation, although some theoretical problems in explaining the result remain, see, e.g., Zdziarski et al. (2012) for a discussion of the implication of the high degree of polarization on the slope of the energy spectrum of the synchrotron emitting electrons, which appears too steep compared to the canonical value of ~2.

Data used in the studies by Laurent et al. (2011b) and Jourdain et al. (2012) are not filtered by the state (generally the INTEGRAL data before ~2010 are dominated by the hard and, to lesser extent, intermediate states). However, in the model of BHB states

---

[3] The angle given by Laurent et al. (2011b) is $140^\circ = 180^\circ - 40^\circ$.

(Sect. 1.1), persistent jets exist only in the hard state. In the intermediate state, the jets are transient, showing distinct ejection events, and in the soft state they are absent. A state resolved polarization analysis is therefore crucial for both, the determination of the origin of the polarized γ-ray emission and better understanding of the changes in accretion/ejection geometry of BHBs between states:

- A clear detection of the polarization of the power law component in the hard state and a non-detection (i.e, a low upper limit) in the soft state would mean that the geometry of the source changes between the states, with a jet present in the hard state and no jet in the soft. The remaining hard X-rays in this state would have a different origin, e.g., in the corona.
- If the power law component is highly polarized in the soft state, the accretion geometry has to remain similar in both, hard and soft states. Although radio emission from Cyg X-1 (and other BHBs) is highly quenched in soft state, this would mean that the γ-ray producing part of the jet persist in the soft state and only the radio producing part of the jet, i.e., the part of the jet further away from the black hole, is disrupted. Here we should especially note that as a persistent source, Cyg X-1 never reaches the deep soft state of some of the transient sources in which the spectrum is fully dominated by the accretion disk. Cyg X-1 may therefore be a BHB analogon of Seyfert galaxies with their weak jets (McHardy et al., 2006).

6.2.2 The states of INTEGRAL observations

ScW-wise INTEGRAL spectra cannot be clearly classified into states by modelling them, without further information due to their low signal to noise ratio. In revolution-wise spectra (~1–2 d exposure each), the hard and the soft state can be clearly distinguished; between hard and intermediate states, however, the difference in both slope and normalizazion is not large enough for a clear identification. Additionally, the source is intrinsically variable on timescales as short as hours (Böck et al., 2011, and Sect. 5.3.2), so that a revolution-wise state classification would result in high contamination by wrongly classified single ScWs.

For a clean classification with known contamination, we use the state classification introduced in Chapter 5 (see also Grinberg et al., 2013). We repeat the following two steps steps first using ASM, then MAXI and then BAT for all yet unclassified ScWs. ASM and MAXI both allow to distinguish all three states, although MAXI classifications are generally somewhat less certain, while only the soft states shows a clear signature in the BAT energy range of 15–50 keV (Sect. 5.2.3, 5.2.5, and 5.2.6).

Step 1: Where simultaneous all sky monitor data are available, they are used to classify the ScW. If more than one all sky monitor datapoint exists and the classifications are inconsistent with each other, the ScW is defined as unclassified.

Step 2: Where no simultaneous all sky monitor data exist, we use the closest all sky monitor within 6 hours from the ScW to classify the ScW.

Table 6.1: Results of the state classification of all INTEGRAL data of Cyg X-1 from 2003 to 2012

state	# ScWs	gross exposure [Ms]	spectrum exposure[a] [Ms]
hard	1739	4.3	2.11
intermediate	316	0.8	0.22
soft	868	2.1	1.2
unclassified	379[b]	–	–

[a] Dead time corrected exposure, from the `exposure` keyword in the header of the spectral files. [b] 28 observations are classified as "unclassified" because of disparate simultaneous classifications; 351 cannot be classified, because there is either no all sky monitor data within 6 hours of the ScW or the closest all sky monitor measurement if a BAT measurement that is not in the soft state, since public BAT data cannot be used to distinguish between hard and intermediate states (Sect. 5.2.6).

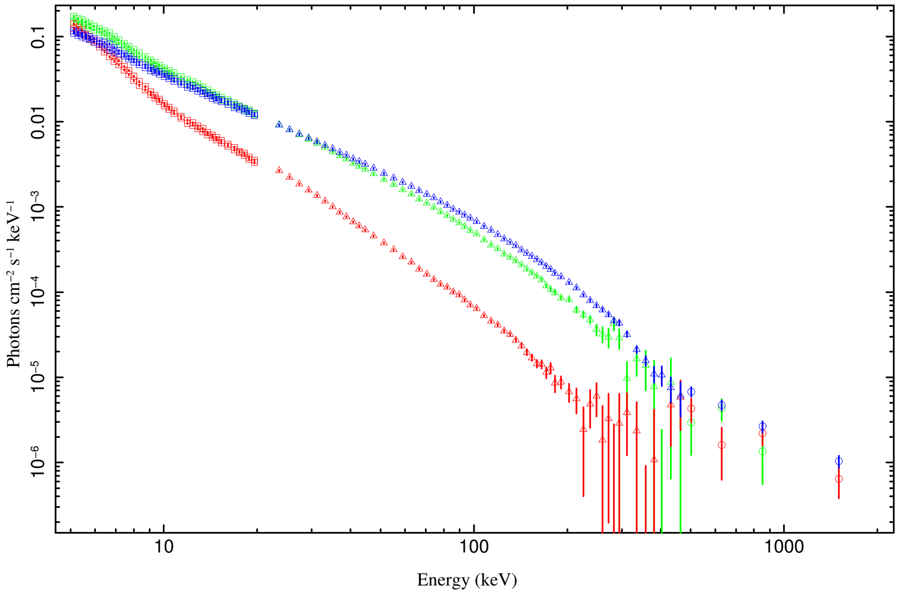

Figure 6.5: Preliminary state-resolved INTEGRAL spectra (count rate space) of all observations of Cyg X-1 available to date. The hard spectrum is shown in blue, the intermediate in green, the soft in red. IBIS/ISGRI data are shown as triangles, Compton mode data as circles, and Jem-X1 and Jem-X2 data as squares. Jem-X and ISGRI Extractions courtesy of J. Rodriguez, Compton mode data courtesy of P. Laurent.

Where Jem-X observations were available, they were classified according to simultaneous IBIS observations. While no polarimetry is possible with Jem-X and the spectra observed with this instrument are generally of rather poor quality compared to other instruments such as RXTE-PCA, they are still useful for constraining the spectral shape in the soft X-ray band in the different states in the data available here.

Table 6.1 gives an overview over the results of the classification of INTEGRAL-IBIS observations. While the hard state exposure is good with ~4.3 Ms exposure, we are clearly lacking exposure in the soft state (~2.11 Ms exposure), especially in the view of the lower hard X-ray flux in the soft state. Since Cyg X-1 entered a series of ongoing soft states in 2010 (Sect. 5.2.1), a proposal for more INTEGRAL observations of the source (2.3 Ms exposure) in the soft state was submitted and is approved for A011 (January to December 2014) to be carried out, unless Cyg X-1 transits into intermediate or hard state at the time of the planned observation.

Although the analysis of the state-resolved INTEGRAL data – especially the complex polarization analysis – is yet work in progress, some preliminary results exists. Figure 6.5 shows state-resolved spectra with IBIS-ISGRI, including Compton-mode data, and both Jem-X instruments. The differences in spectral shape are clearly visible by eye. Note especially the large difference of the soft state to both, the hard and the intermediate states. Final results of the state-resolved spectral and polarization analysis of INTEGRAL data will be presented by Rodriguez et al., 2013 (in prep).

While I am describing to you how Nature works, you won't understand why Nature works that way. But you see, nobody understands that.

(Richard P. Feynman)

7

Spectro-timing analysis

The first step to understanding the X-ray timing characteristics of a black gole is a fundamental overview of their evolution with the spectral shape that can only be achieved with a high number of high quality observations densely covering all states, including the elusive transitions. Most previous work on different sources concentrates on energy-independent evolution of rms and power spectral distributions (PSDs) with spectral state (e.g., Klein-Wolt & van der Klis, 2008), although further state-, energy-, and Fourier frequency-dependent correlations have been noted in individual observations and smaller samples (e.g., Cui et al., 1997; Böck et al., 2011; Muñoz-Darias et al., 2011; Cassatella et al., 2012a). Missing are consistent analyses of energy-resolved evolution of rms and PSDs, Fourier-frequency dependent evolution of cross-spectral quantities (coherence function and lags), and correlations of features in PSDs and Fourier-frequency dependent cross-spectral quantities over the full range of spectral shapes and over multiple transitions. In this Chapter, we address these questions with an extraordinarily long and well sampled observational campaign on the high mass black hole binary Cyg X-1, which enables us to conduct the most comprehensive spectro-timing analysis of a black hole binary to date.

We start Sect. 7.1 by introducing the data and the general behavior of the source during the analyzed time period and follow with a description of the spectral analysis and employed X-ray timing techniques. In Sect. 7.2, we discuss the energy independent and dependent evolution of the rms and the PSDs with spectral shape. In Sect. 7.3, we discuss the evolution of cross-spectral quantities with spectral shape. We address the implication of our results for the analysis of other sources in Sect. 7.4 and to theory in Sect. 7.5. Sect. 7.6 is a summary of the results of our spectro-timing approach.

7.1 Data Analysis

The data analyzed here are mostly from the bi-weekly observational campaign with RXTE that was initiated in 1999 and continued until the demise of RXTE at the end of 2011. Parts of the data have been analyzed in the previous papers in the 'Long term variability of Cyg X-1'-series (Pottschmidt et al., 2003; Gleissner et al., 2004a,b; Wilms et al., 2006; Grinberg et al., 2013, see also Chapter 5) and by other authors (e.g., Axelsson et al., 2005, 2006; Shaposhnikov & Titarchuk, 2006). For all pointed RXTE observations of Cyg X-1 made during the lifetime of the RXTE satellite (MJD 50071–55931), we extracted spectral data from Proportional Counter Unit 2 of RXTE's Proportional Counter Array (PCA, Jahoda et al., 2006) and from RXTE's High Energy X-ray Timing Experiment (HEXTE, Rothschild et al., 1998) on an orbit-by-orbit basis. The data reduction was performed with HEASOFT 6.11 as described in Sect. 5.1.2 and resulted in a total of 2741 spectra. At the time of writing, there had been no changes to relevant pieces of HEASOFT since this release. We stress the importance of the orbit-wise approach, as spectral and timing properties of Cyg X-1 can change on timescales of less than a few hours (Axelsson et al., 2005; Böck et al., 2011; Grinberg et al., 2013, and Chapter 5).

7.1.1 Long-term source behavior

The general behavior of Cyg X-1 during the lifetime of RXTE has been discussed in Chapter 5. Figure 7.1 presents an overview of the evolution of the RXTE All Sky Monitor (ASM, Levine et al., 1996) count rate, the spectral shape and a choice of typically used X-ray timing parameters.

The data used here cover periods of different source behavior such as pronounced, long hard and soft states, and multiple failed and full state transitions. The strict use of the same data mode means that we do not cover some of the observations included in previous long-term monitoring analyzes by Pottschmidt et al. (2003), Axelsson et al. (2005, 2006), or Shaposhnikov & Titarchuk (2006), especially the data from the very hard state before 1998 May. The large time span covered in this work that includes of the extraordinarily long, hard state of ~MJD 53900–55375 (mid-2006 to mid-2010) and the following series of stable soft states represents, however, a major improvement over all previous analyses.

7.1.2 Spectral analysis

The extraction of spectral data and the spectral analysis presented here is the same as described in Chapter 4. However, there are seven observations where the χ^2 criterion for the model selection from Sect. 5.2.2 gives an unphysical result and can be clearly seen as outliers in the tight correlation between rms-ratio and Γ_1 discussed in Sect. 7.2.1. When modeling these seven observations without a disk all have pronounced residuals at ~5 keV due to the Xe L-edge (Wilms et al., 2006), no signature of a strong disk in the residuals and an acceptable reduced $\chi^2 < 1.3$. Despite this behavior, with a disk, χ^2_{red}

improves, but the disk is peculiarly strong and the power law component is very steep, making these observations outliers in the very tight correlation of Γ_1 with $\Delta\Gamma = \Gamma_1 - \Gamma_2$ (Wilms et al., 2006). This behavior indicates that the strong disk component and the steep power law slope compensate the instrumental Xe L-edge and are not an adequate description of the source spectrum. We therefore accept the model without a disk as the best fit model for these observations[1]. A good fit with $\chi^2_{\mathrm{red}} < 1.2$ can be achieved for 1721 out of the 1980 observations with the right data mode for timing analysis. Our fits yield $\chi^2_{\mathrm{red}} < 2.5$ for all 1980 observations. In the following, we will again use Γ_1 as a proxy for the spectral state (see also Sect. 5.2.2).

7.1.3 Calculation of X-ray timing quantities

We extracted light curves that are strictly simultaneous to the spectral data. For a consistent treatment of the timing properties, we strictly adhered to the same data mode and only used observations in the `B_2ms_8B_0_35_Q` mode, i.e., binned data with 8 channels bands (channels 0–10, 11–13, 14–16, 17–19, 20–22, 23–26, 27–30, and 31–35) and with an intrinsic time resolution of $2^{-9}\,\mathrm{s} \approx 2\,\mathrm{ms}$, resulting in a reduced number of 1980 RXTE orbits. Because this data mode does not include PCU information, light curves can only be extracted from all PCU units that were operating during a particular observation together. Since dead time effects depend on the number of active detectors, we treat each combination of PCUs separately. This approach results in an increase of the number of light curves to 2015, some of them associated with the same spectrum.

In Table 7.1, we list the channel and energy ranges for the four energy bands that are used throughout this Chapter for the calculation of the timing properties (band 3 and band 4 combine three channel bands each in order to obtain higher count rates). The energy range covered by the bands is slightly time dependent because of changes in the high voltage of the PCA:

- Band 1 (2.1–4.5 keV) covers the range with a significant contribution from the accretion disk and can be dominated by it in the soft states. At the high soft count rates of the soft states this band can suffer from telemetry overflow (Gleissner et al., 2004b; Gierliński et al., 2008), resulting in artifacts at high frequencies.
- Band 2 (4.5–5.7 keV) covers the soft part of the spectrum above the main contribution of the disk but below the prominent Fe Kα-line at ~6.4 keV (Wilms et al., 2006; Shaposhnikov & Titarchuk, 2006; Duro et al., 2011).
- Band 3 (5.7–9.4 keV) includes the region of the Fe Kα-line and covers the spectrum up until about the spectral break at ~10 keV.
- Band 4 (9.4–15 keV) mainly covers the spectrum above the spectral break at ~10 keV and below the high-energy cut-off.

---

[1] In the previous study (Grinberg et al., 2013, see also Chapter 4 and Chapter 5), these seven observations did not receive any special treatment, however, this does not influence any of our earlier results.

We calculated all timing properties (power spectra [power spectral densities, PSD], cross power spectra, coherence and time lags) following Nowak et al. (1999) and Pottschmidt et al. (2003).

For the timing analysis each light curve was split into segments of $n_{\mathrm{bins}} = 4096$ bins, i.e., 8 s length. Timing properties were calculated for each segment and then averaged over all segments of a given light curve using the appropriate statistics. The mean number of segments used was ∼225 and the mean light curve length ∼30 min. Before rebinning, the values of all timing properties were calculated for discrete Fourier frequencies f_i linearly spaced every $\Delta f = 1/(n_{\mathrm{bins}}\Delta t) = 0.125\,\mathrm{Hz}$. The Nyquist frequency of the data is $f_{\max} = 1/(2\Delta t) = 256\,\mathrm{Hz}$. The lowest frequency accessible is $f_{\min} = 1/(n_{\mathrm{bins}}\Delta t) = 0.125\,\mathrm{Hz}$. As shown by Nowak et al. (1999), for a source such as Cyg X-1 and using the approach described above, the dead time corrected, noise-subtracted PSDs are reliable to at least 100 Hz. The systematic uncertainties for the coherence function are negligible below 30 Hz and the phase and time lags are detectable in the 0.1–30 Hz range (Nowak et al., 1999).

Longer individual segments would enable us to probe lower Fourier frequencies. The lower number of averaged segments per observation would in such case mean a lower but still good signal to noise ratio in the case of PSDs. Coherence function and lags are, however, higher order derivative statistics and therefore more sensitive to uncertainties. Thus a large number of segments to be averaged, i.e., short individual segments, is necessary to constrain them well, motivating our choice of 8 s long segments.

For PSDs we choose the normalization of Belloni & Hasinger (1990) and Miyamoto et al. (1991), where the PSD is given in units of the squared fractional rms variability per frequency interval. Since the variance that each frequency contributes is given in units of average signal count rate, this normalization is most suitable for comparing PSD shapes independently of source brightness (Pottschmidt, 2002). In order to illustrate the contribution of the variability at a given frequency, f_i, to the total variability, we show the PSDs in units of PSD times frequency, $\mathrm{PSD}(f_i) \times f_i$ (Belloni et al., 1997; Nowak et al., 1999). We calculated the fractional rms directly from the PSDs without employing any fits for the PSD shape; all rms values are in the range 0.125–256 Hz.

Our sign convention chosen for the calculation of the cross-spectral quantities is such that the hard light curve lags the soft for a positive lag. Since the phase lag, ϕ, is defined on the interval $[-\pi, \pi[$ there is an upper limit for absolute value of the time lag. Experience shows that the lags are below this limit in the considered frequency range in objects such as Cyg X-1 (e.g., Nowak et al., 1999; Pottschmidt et al., 2000, 2003; Böck et al., 2011), Swift J1753.5−0127 (Cassatella et al., 2012a), or XTE J1752−223 (Muñoz-Darias et al., 2010).

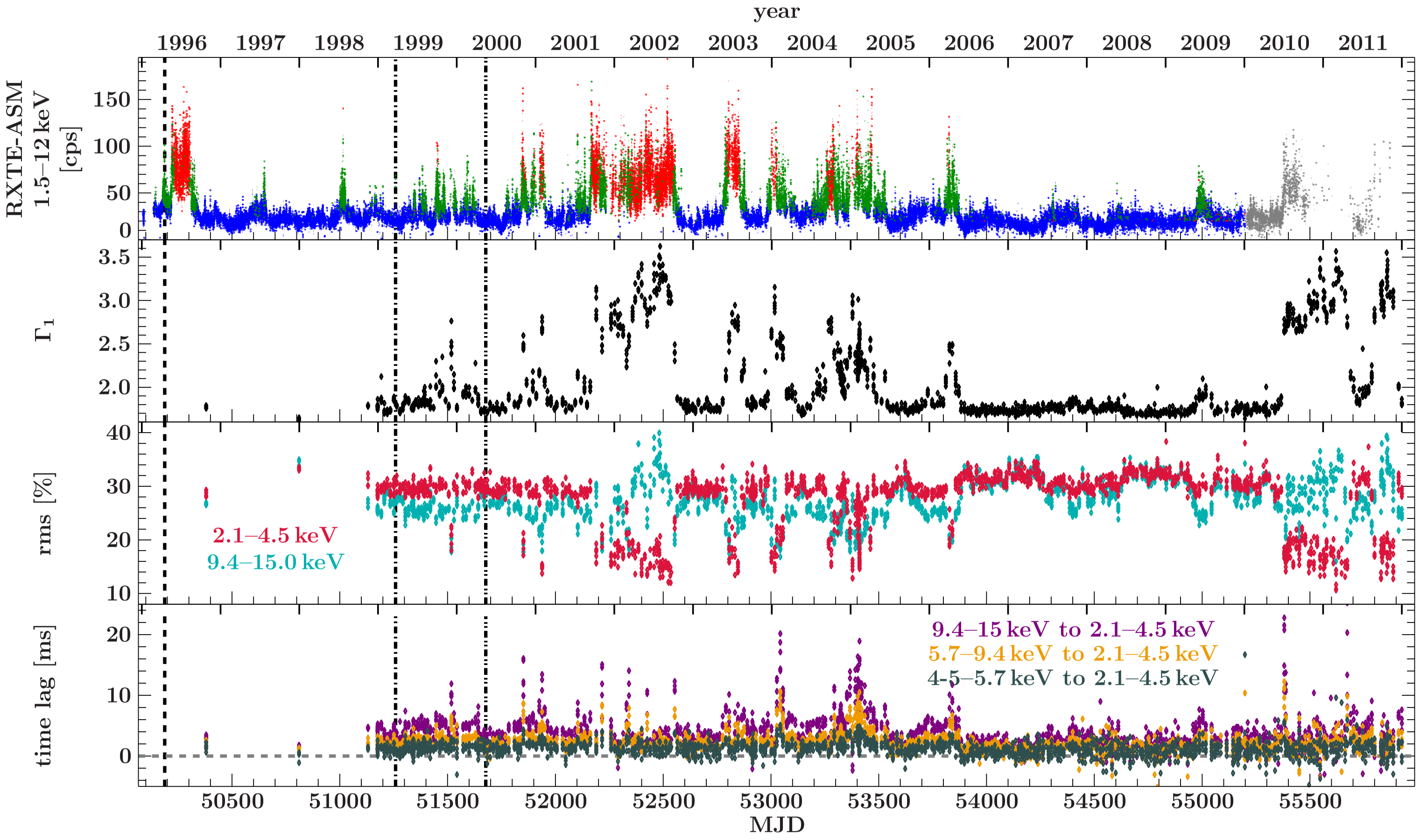

Figure 7.1: Evolution of Cyg X-1 over the RXTE lifetime. Vertical lines represent the starting times of the RXTE calibration epochs used in this work: dashed line epoch 3, dot-dashed line epoch 4 and dot-dot-dashed line epoch 5. The total ASM count rate is color-coded according to ASM-based state definition of Grinberg et al. (2013), which uses both ASM count rate and hardness of a given measurement: blue represents the hard state, green the intermediate state, and red the soft state. The soft photon index Γ_1 is shown only for those 1980 RXTE observations that were conducted in the `B_2ms_8B_0_35_Q` binned data mode, see Sect. 7.1.3.

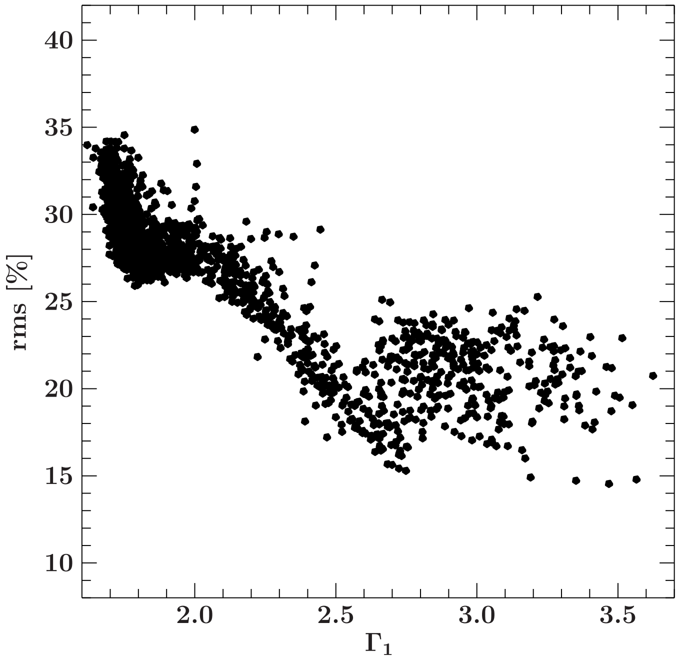

Figure 7.2: Fractional rms in the 2.1–15 keV band vs. soft photon index Γ_1.

7.2 rms and power spectra

7.2.1 Evolution of fractional rms with spectral shape

We start with the most basic quantity, the rms variability of the source. As we have previously shown in Sect. 5.2.2, the total fractional rms in the 0.125–256 Hz frequency band strongly depends on the spectral state and on the energy band. Here, we analyze this behavior in more detail.

Energy independent vs. energy dependent evolution of rms

Figure 7.2 shows how the fractional rms in the 2.1–15 keV band depends on the spectral shape. The rms reaches its largest values of ~34% at the lowest Γ_1 of ~1.6. The Γ_1-rms correlation is negative below $\Gamma_1 \approx 1.8$, then flat until $\Gamma_1 \approx 2.0$, again negative until $\Gamma_1 \approx 2.5$–2.7, and finally flattens out at an rms of ~20% but with a larger scatter.

The energy dependent fractional rms reveals where most of this variability in the total 2.1–15 keV band comes from in the different spectral states. Figure 7.1 shows the evolution of the fractional rms in the soft band 1 and the hard band 4 (2.1–4.5 keV and 9.4–15 keV). During hard states, the variability is high at about ~30% in both bands. In the soft state, the rms drops to 10–20% in band 1 but is slightly larger than in the hard state in band 4. The intermediate state is associated with a decrease of rms in both bands. This behavior is better visualized in Fig. 7.3, where we plot rms as a function of Γ_1 for bands 1–4. By eye, we identify four Γ_1 ranges with different behavior (see Table 7.2 for correlation coefficients for bands 1–4 and the total band):

Table 7.1: Energy bands used for different RXTE calibration epochs.

epoch	band 1 energy [keV] (channels)	band 2 energy [keV] (channels)	band 3 energy [keV] (channels)	band 4 energy [keV] (channels)
3	$\sim$1.9[b]–4.1 (0–10)	$\sim$4.1–5.1 (11–13)	$\sim$5.1–8.3 (14–22)	$\sim$8.3–13.0 (23–35)
4	$\sim$2.1[b]–4.6 (0–10)	$\sim$4.6–5.9 (11–13)	$\sim$5.9–9.7 (14–22)	$\sim$9.7–15.2 (23–35)
5[a] (PCU 0)	$\sim$2.0[b]–4.6 (0–10)	$\sim$4.6–5.8 (11–13)	$\sim$5.8–9.7 (14–22)	$\sim$9.7–15.4 (23–35)
5[a] (PCU 1,2,3,4)	$\sim$2.1[b]–4.5 (0–10)	$\sim$4.5–5.7 (11–13)	$\sim$5.7–9.4 (14–22)	$\sim$9.4–14.8 (23–35)

Values from `http://heasarc.nasa.gov/docs/xte/e-c_table.html`. Starting times of epochs are shown in Fig. 7.1. Since the majority of the data is from epoch 5, we cite the band energies throughout this paper as 2.1–4.5 keV for band 1, 4.5–5.7 keV for band 2, 5.7–9.4 keV for band 3, and 9.4–15 keV for band 4. [a]Epoch 5 is defined by loss of the propane layer in PCU 0 due to a micrometeorite impact. [b]Nominally the 0th channel extends to $\sim$0 keV, but the effective area is negligible below 2 keV (Jahoda et al., 2006).

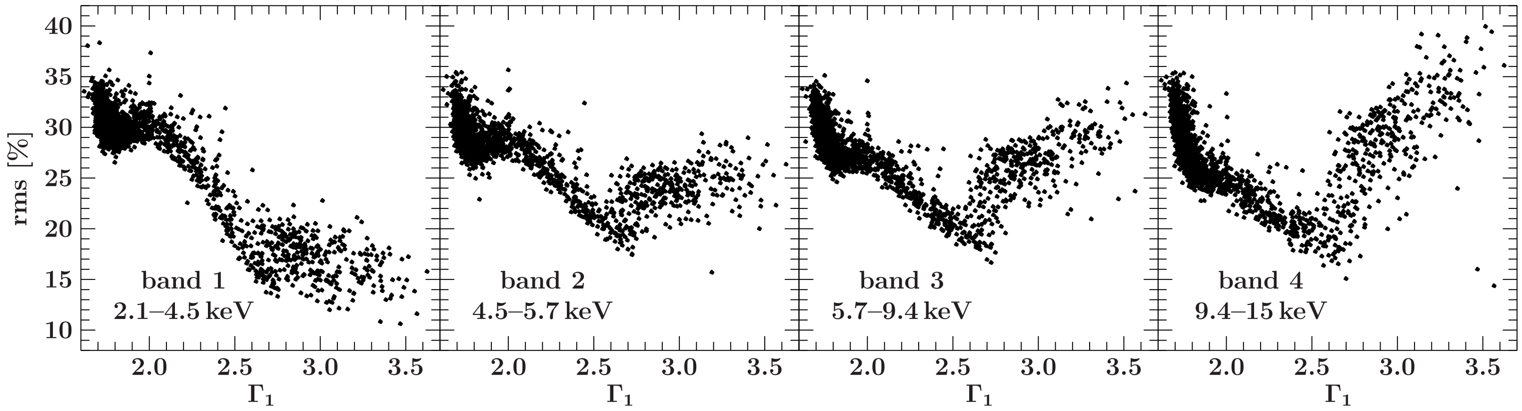

Figure 7.3: Fractional rms in the 0.125–256 Hz frequency band for different energy bands vs. the soft photon index, Γ_1, of the broken power law fits.

Table 7.2: Spearmann ρ correlation coefficients for Γ_1-rms correlation.

band	$\rho_{\Gamma_1<1.8}$	$\rho_{1.8<\Gamma_1<2.0}$	$\rho_{2.0<\Gamma_1<2.65}$	$\rho_{2.65<\Gamma_1}$
2.1–15 keV	−0.61	0.21^b	−0.89	0.02^c
1	−0.50	0.25	−0.89	−0.28
2	−0.55	0.19	−0.88	0.43
3	−0.62	-0.064^a	−0.84	0.65
4	−0.64	−0.31	−0.70	0.68

All null hypothesis probabilities $P < 10^{-4}$ except for [a]with $P = 0.18$, [b]with $P = 0.21$, and [c]with $P = 0.66$

- $\Gamma_1 < 1.8$: the Γ_1-rms correlation is negative and becomes stronger at higher energies in the individual and the total bands;
- $1.8 \leq \Gamma_1 < 2.0$: the correlation is positive for band 1 and 2 and negative for band 4. In band 3, the rms values are consistent with being uncorrelated with Γ_1, an understandable behavior given the change of sign in adjacent bands. In the total band, there is no correlation.
- $2.0 \leq \Gamma_1 < 2.65$: the correlation is strong and negative in all bands including the total, though it becomes less steep with increasing energy;
- $2.65 \leq \Gamma_1$: the correlation changes from negative in band 1 to positive in bands 2–4 and becomes stronger with increasing energy. The total rms in the 2.1–15 keV band shows no correlation with spectral state.

The changes in slope of the rms-Γ_1 relationship at $\Gamma_1 \sim 1.8$ and $\Gamma_1 \sim 2$ are present both when considering only observations that do not require a disk and only observations that do require a disk. They are therefore not artifacts of the choice of spectral model used to measure Γ_1. For $\Gamma_1 > 2$, the number of observations which do not require a disk is negligible.

A compact representation of the rms behavior is given by the ratio of the rms values between the different bands (Fig. 7.4). The relation is tight enough that it can serve as a simple proxy for the spectral shape of the source without any model assumptions. We used it, e.g., to check our broken power law fits for outliers as described above in Sect. 7.1.2. We emphasize that because of the strong energy dependency of the rms, the total fractional rms in the 2.1–15 keV band (Fig. 7.2) cannot be used to determine the depth of the soft state, while the rms at energies above ~6 keV or the ratio of rms at different energies (Fig. 7.4) can.

The energy-independent analyses of RXTE of Pottschmidt et al. (2003, 2.1–15 keV range) and Axelsson et al. (2006, 2–9 keV range) are consistent with the rms evolution presented here, although we partly covered different time ranges. A decrease of the rms as the source softens was also observed at higher energies, namely by Torii et al. (2011, *Suzaku*; 10–200 keV) and Cabanac et al. (2011, INTEGRAL-SPI; 27–49 keV), though neither of them observes a full soft state with $\Gamma_1 > 2.5$–2.7, where our analysis shows an increase of rms above ~6 keV

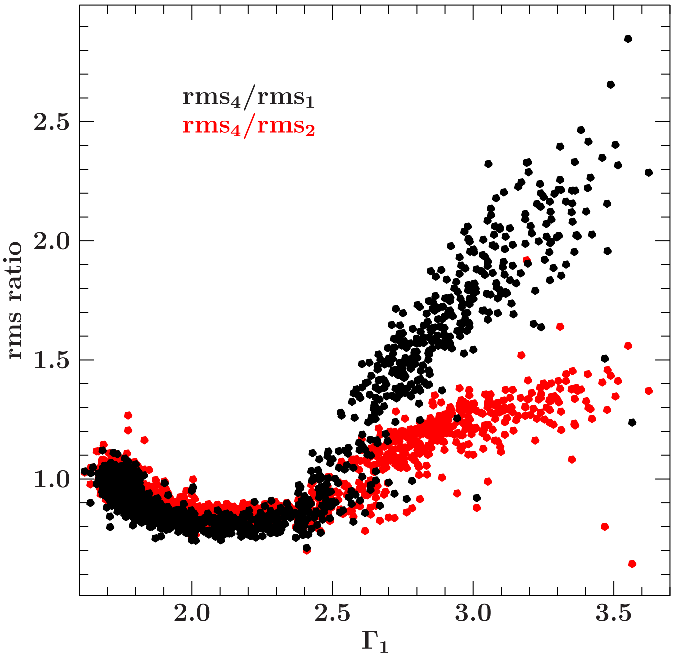

Figure 7.4: Ratio of fractional rms in different energy bands (band 1 – rms_1, band 2 – rms_2, band 4 – rms_4,) vs. the soft photon index Γ_1.

rms spectra

To understand the behavior of rms with both energy and spectral shape better, we look at the behavior of these quantities in the eight bands of the `B_2ms_8B_0_35_Q` mode. For each energy band, we determine the average fractional rms from all observations during which a similar spectral shape was found. Two spectra are considered similar if their respective Γ_1 values fall into the same bin of a linear grid with steps of $\Delta\Gamma_1 = 0.01$ between $\Gamma_{1,\mathrm{min}} = 1.64$ and $\Gamma_{1,\mathrm{max}} = 3.6$. The trends shown in Fig. 7.3 and Table 7.2 are confirmed. The higher energy resolution allows us to see the gradual increase of fractional rms for $\Gamma_1 \gtrsim 2.7$ at all energies above 4.5 keV. The increase steepens at higher energies. For $1.8 < \Gamma_1 < 2.3$ there is also indication for slightly lower variability above 4.5 keV than below, although the decrease does not appear smooth but rather shows an indication of recovery above 11 keV.

Examples of rms spectra shown by Gierliński et al. (2010) agree with Fig. 7.5, but they do not observe an increase of the rms above 11 keV for $1.8 < \Gamma_1 < 2.3$. Such an increase is present (but not pointed out) in the only Cyg X-1 rms spectrum shown by Muñoz-Darias et al. (2010). In the 10–200 keV range, Torii et al. (2011) show that the fractional rms spectra remain largely flat in hard and intermediate[2] states and that the intermediate state shows less variability than the hard state, i.e., the behavior presented here for the 2.1–15 keV range continues at higher energies.

---

[2] Torii et al. (2011) speak only of hard states with high ASM count rates; a comparison with ASM-HID-based state definition of Grinberg et al. (2013) shows that these states are intermediate.

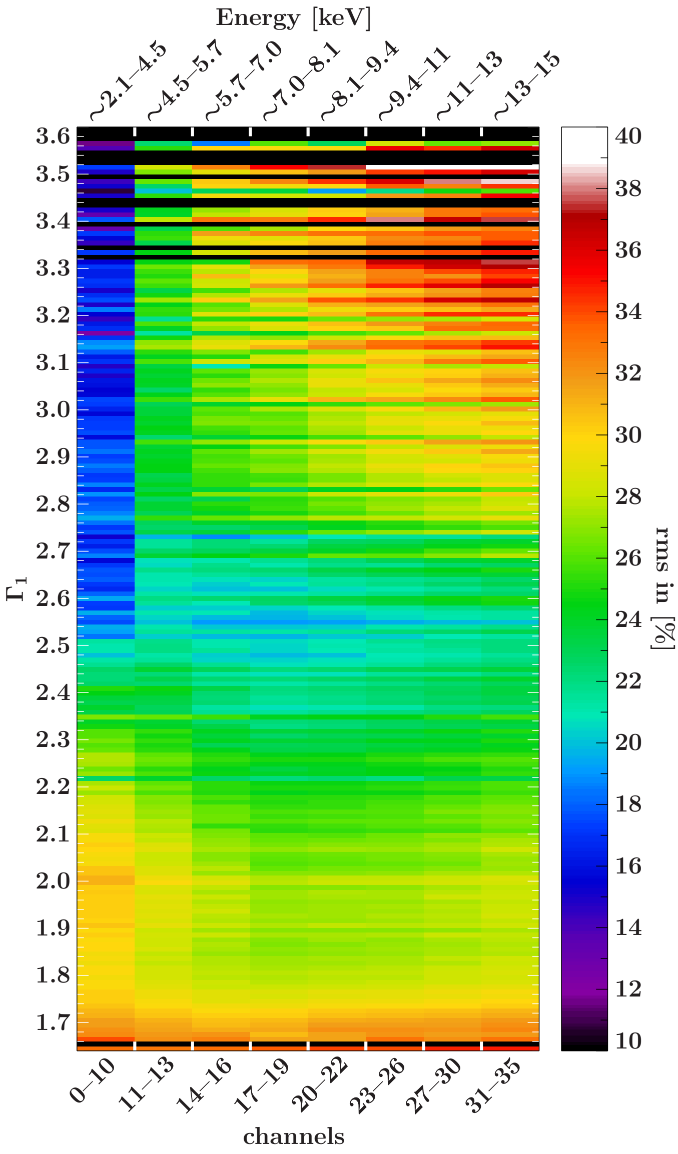

Figure 7.5: Evolution of fractional rms between 0.125–256 Hz in the eight binned channels of the `B_2ms_8B_0_35_Q` mode with the X-ray spectral shape represented by the soft photon index Γ_1. Black horizontal lines are photon indices for which no data are available.

7.2.2 Evolution of PSDs with spectral shape

Having discussed the overall source variability by studying the rms, we now turn to the Fourier frequency dependent variability. For our analysis of the change of PSD shapes with spectral state, we choose an approach that does not require us to model the PSDs and thus does not introduce any assumptions on identification of possible components in individual PSDs and their evolution. For possible pitfalls of such assumptions, see Sect. 7.4.1.

We visualize the evolution of the PSD components as a color map in f_i-Γ_1-space following an idea of Böck et al. (2011). As in the analysis of the rms behavior we define a grid with steps of $\Delta\Gamma_1 = 0.01$ between $\Gamma_{1,\mathrm{min}} = 1.64$ and $\Gamma_{1,\mathrm{max}} = 3.59$ and 100 equally spaced steps in logarithmic frequency between 0.125 Hz and 256 Hz. When mapping linear Fourier

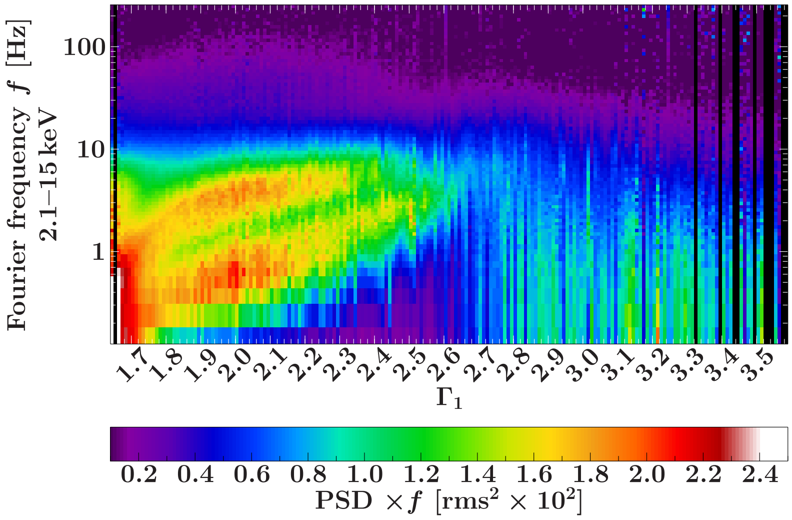

Figure 7.6: Evolution of PSDs in 2.1–15 keV band (sum of bands 1–4 and full energy range of the `B_2ms_8B_0_35_Q` mode) with spectral shape. In this and in all following figures, black vertical lines are photon indices for which no data are available.

frequencies to a logarithmic grid, some bins remain empty. We allocate these to adjacent bins containing at least one Fourier frequency, equally divided between higher and lower bins.

Energy-independent evolution of PSDs with spectral shape

Most previous work addresses the timing quantities in an energy-independent way. Because of the strong changes in spectral shape (see Nowak et al., 2012, for examples of broadband spectra of Cyg X-1 in hard and soft states) and hence count rate ratios at different energies, extrapolation from energy-band dependent quantities to the full energy range across all spectral states is non-trivial, so that we first address the full 2.1–15 keV range and show the evolution of these PSDs with spectral shape in Fig. 7.6.

For $1.75 < \Gamma \lesssim 2.7$, two strong variability components are present. We label the lower frequency variability component as component 1 and the higher frequency variability component as component 2. By visual comparison one can identify the components with the two Lorentzians of Böck et al. (2011) and with the two lowest frequency Lorentzian components of Pottschmidt et al. (2003). Both components shift to higher frequencies as Γ_1 grows, consistent with previous work (Cui et al., 1997; Gilfanov et al., 1999; Pottschmidt et al., 2003; Axelsson et al., 2005; Shaposhnikov & Titarchuk, 2006; Böck et al., 2011). The two components appear of roughly similar strength. Component 2 disappears at $\Gamma_1 \approx 2.5$, so that the PSD for $2.5 < \Gamma_1 < 2.7$ is dominated by component 1. Note also the low variability at the lowest frequencies in the $\Gamma_1 \sim 2.3$–2.6 range.

For $\Gamma_1 \lesssim 1.75$, we see additional power at frequencies higher than the evolution of components 1 and 2 with Γ_1 would indicate for them. This is consistent with the appearance of the third Lorentzian component in the very hard observations analyzed by Pottschmidt et al. (2003) and Axelsson et al. (2005). We note that the hardest observations analyzed by these authors are from before 1998 April, i.e., during a time not covered by the data mode we use, while the hardest spectra analyzed here were observed during the long hard state between mid-2006 and mid-2010 (Nowak et al., 2011; Grinberg et al., 2013). Interestingly, the overall variability amplitude increases in this Γ_1-range at all f_i below $\sim$10 Hz.

Above $\Gamma_1 \approx 2.7$, the variability is generally low, consistent with low total rms in this range (Fig. 7.2), and continuous, without strong component. It is strongest at the lowest frequencies and decreases towards higher frequencies.

Energy-dependent evolution of PSDs with spectral shape

The energy-dependent evolution of the fractional rms (Sect. 7.2.1) hints that the PSDs are highly dependent on the energy band considered, especially in the soft spectral state. The shape of the PSDs in all four energy bands is shown on Fig. 7.7. These maps emphasize the dominant components and use a linear color scale for the $\mathrm{PSD}(f_i) \times f_i$ values, while usually individual power spectra are presented on a logarithmic $\mathrm{PSD}(f_i) \times f_i$-axis (see Fig. 7.8).

For $1.75 \lesssim \Gamma_1 \lesssim 2.7$ we see the same two variability components as in the energy-independent PSDs. Both components become weaker with increasing energy. The amplitude of component 1 decreases quicker than the amplitude of component 2: component 1 is stronger than component 2 in band 1 (4.5–5.7 keV), in band 4 (9.4–15 keV) component 2 is more pronounced. Especially in the $\Gamma_1 \approx 2.4$–2.6 range, component 1 dominates the lower bands, but component 2 the higher.

For $\Gamma_1 \lesssim 1.75$, the shape of the PSDs appears energy-independent, as opposed to the softer observations. The additional higher frequency component discussed for the energy-independent case is present in all bands.

For $\Gamma_1 \gtrsim 2.7$, the variability shows a behavior fundamentally different from the behavior of the two components in the $1.75 \lesssim \Gamma_1 \lesssim 2.7$ range, as indicated by the different behavior of the rms (Sect. 7.2.1). In band 1, the overall variability is low, consistent with the evolution of the total rms. What variability there is, seems to show a slight trend towards lower frequencies with increasing Γ_1. In bands 2 to 4, the variability increases strongly with increasing energy of the band and within an energy band with increasing Γ_1.

Figure 7.8 presents examples of average PSDs at different spectral shapes to facilitate comparison with previous work. The sharp increase of the PSD values for $\Gamma_1 \sim 2.85$ and 3.25 for the 2.1–4.5 keV band is an artifact of the telemetry saturation at the high soft count rates associated with the soft states (Gleissner et al., 2004b; Gierliński et al., 2008). While the continuous change in the PSD is better illustrated in the approach of Fig. 7.7, two effects are better represented in this view. First, in the frequency range considered here the shape of the power spectra at the higher energies is similar for $\Gamma_1 > 3.15$ and $\Gamma_1 < 1.75$. Secondly, there are indications of a weak third hump above 10 Hz for $1.75 \lesssim \Gamma_1 \lesssim 2.15$ that is not visible in this range on Fig. 7.7 and that corresponds to the higher frequency Lorentzian component L_3 modeled by Pottschmidt et al. (2003).

An energy-dependent approach to both rms and PSDs is clearly decisive to understand the variability components in different states as they show strikingly different behavior with

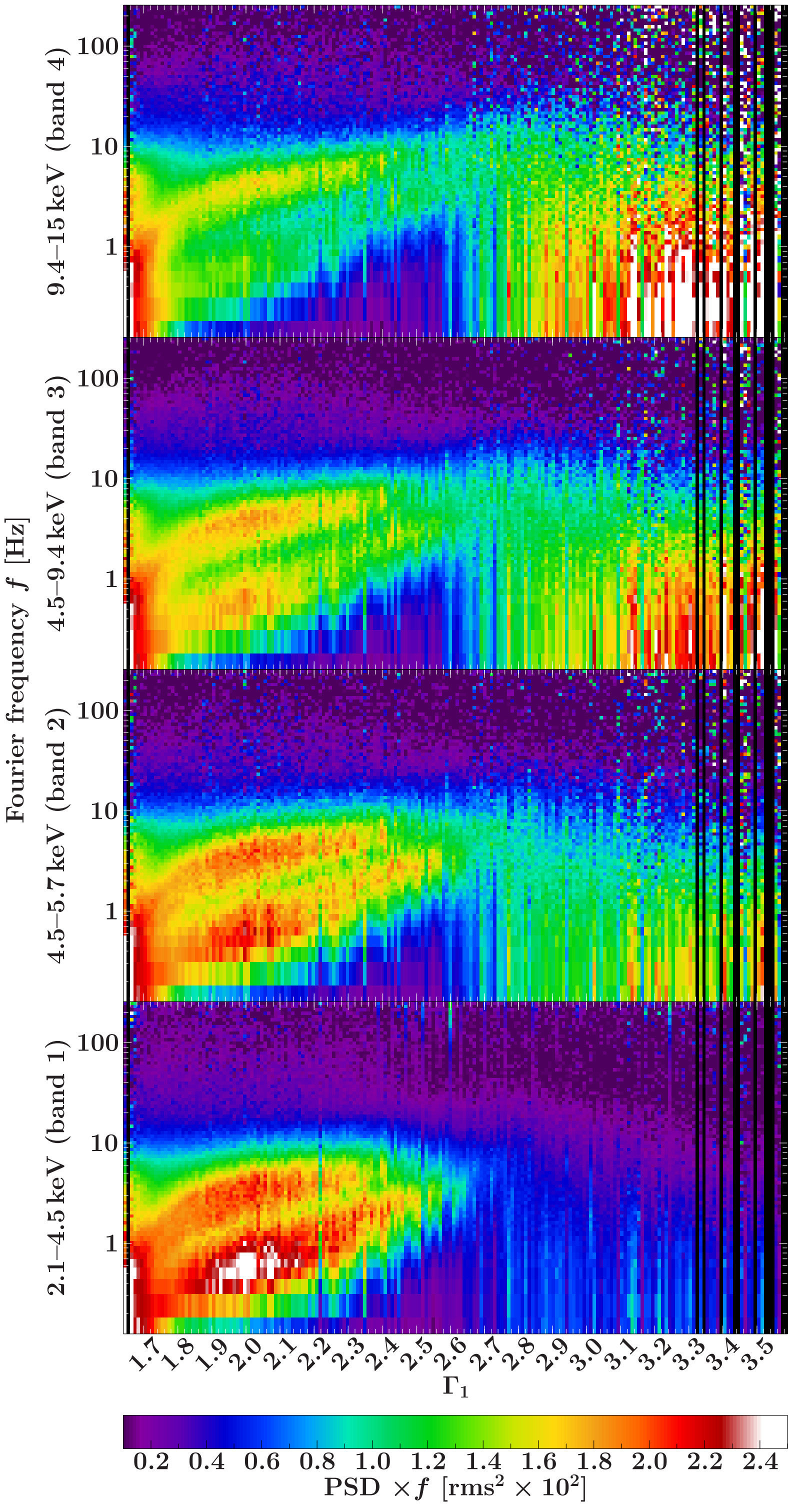

Figure 7.7: Evolution of the PSDs with spectral shape represented by the soft photon index Γ_1 of the broken power law fit in four energy bands (see Table 7.1). Color scale represents averaged PSD(f_i) $\times$ f_i values at individual Fourier frequencies f_i.

changing energy that is otherwise missed. This may be especially important when comparing black hole binaries to AGN and cataclysmic variables, where at the same energy we probe different parts of the emission.

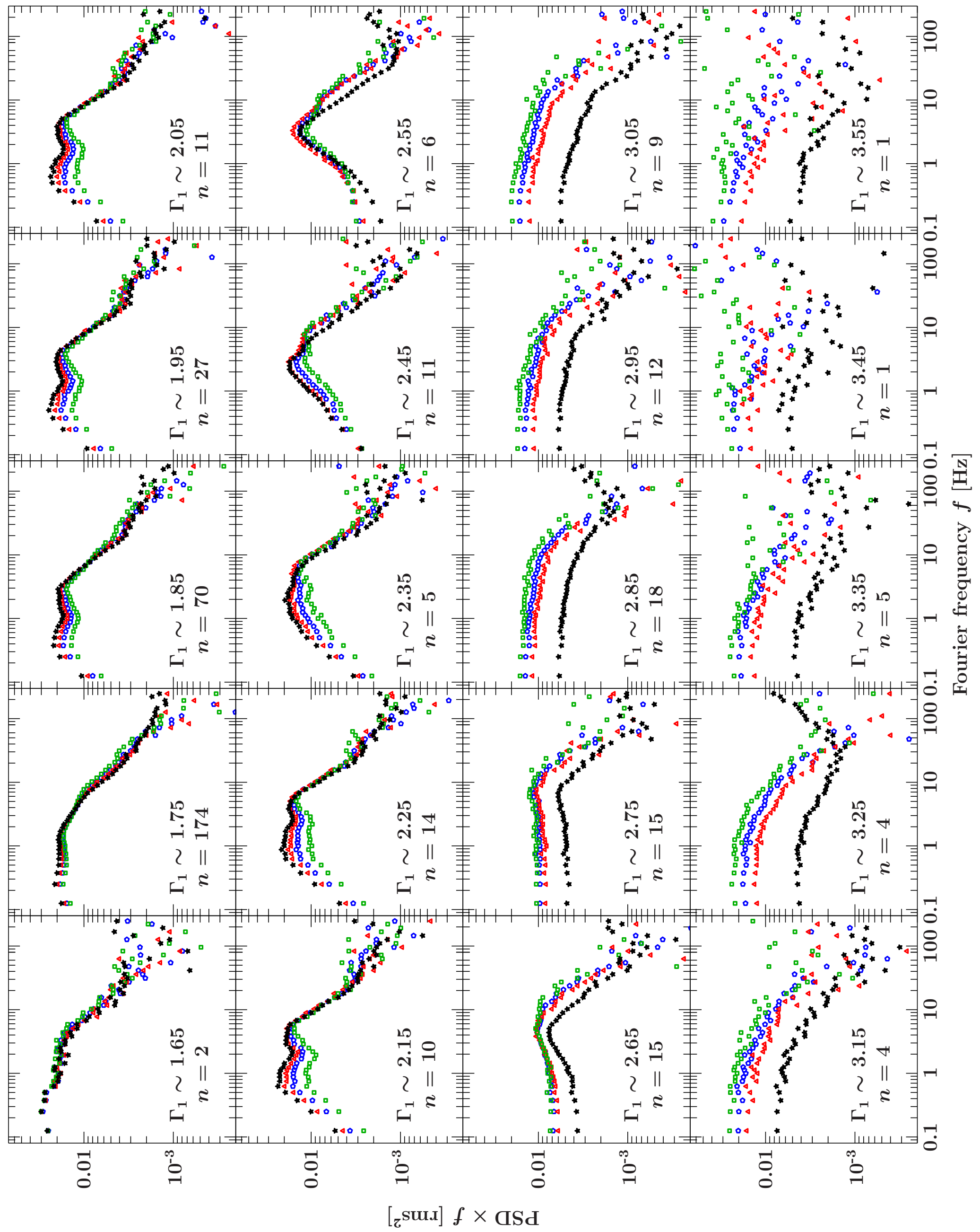

Figure 7.8: Overview of the average PSDs at different spectral shapes. PSDs are binned on a logarithmically binned grid with $\mathrm{d}f/f = 0.15$. Each PSD is the average of all n PSDs falling within the $\Gamma_1 \pm 0.01$ interval for the given Γ_1 values. Black stars show PSDs in the 2.1–4.5 keV band, red triangles in the 4.5–5.7 keV band, blue circles in the 5.7–9.4 keV, and green squares in the 9.4–15 keV band.

Discussion of PSD shapes

The frequency shift of the variability components of the PSDs in the RXTE range with the softening of the source in the hard and intermediate state continues at higher energies (Cui et al., 1997; Pottschmidt et al., 2006; Cabanac et al., 2011) up to ~200 keV (Torii et al., 2011), even though such high energy analyses are rare. The different energy dependency of the components has been previously noted for individual observations, both for the presented energy range and above (Cui et al., 1997; Nowak et al., 1999; Pottschmidt et al., 2006; Böck et al., 2011), but never shown for such a comprehensive data set as presented here.

Intermediate state are often modeled with a combination of Lorentzian components with (cut-off) power law, while the $\sim 1/f$-variability of the soft state PSDs can mostly be described by a power law only (e.g., Cui et al., 1997; Axelsson et al., 2005, 2006). Cui et al. (1997) have noted that the power law component becomes stronger with increasing energy for individual soft state observations up to 60 keV; we observe this effect up to our maximal energy of 15 keV. We also clearly see that at energies above 4.5 keV, the variability grows with increasing Γ_1 for $\Gamma_1 > 2.7$, but shows a slight decreasing trend in the 2.1–4.5 keV band.

Our approach does not allow us to track weak power law in the intermediate state, especially given our lowest accessible frequency of 0.125 Hz. However, we see that the power law dominates the PSDs for $\Gamma_1 \gtrsim 2.7$ – the abrupt change can also be seen in the cross spectral quantities presented in the next Section (Sect. 7.3). In particular, for $\Gamma_1 \gtrsim 2.7$, the coherence, which has shows a dip for $2.5 < \Gamma_1 < 2.7$, recovers (Sect. 7.3.1); the time lag spectra lack the previously present structure (Sect. 7.3.2); and the averaged time lags show an abrupt drop and no correlation with Γ_1 for $\Gamma_1 \gtrsim 2.65$ (Sect. 7.3.3). Cross-spectral quantities are clearly crucial to better understand the variability of the source.

7.3 Coherence and time lags

7.3.1 Evolution of Fourier-dependent coherence with spectral shape

We calculate maps of the coherence function, $\gamma^2_{h,s}$ where $h \in \{4, 3, 2\}$ is the harder band and $s \in \{3, 2, 1\}$ is the respective softer band, using the same grid as in our analysis of the power spectra (Sect. 7.2.2). Figure 7.9 shows maps of the coherence function between band 4 and bands 1, 2, and 3.

All maps show a rather well-defined envelope that follows the outlines of the dominant variability components of the power spectra (Sect. 7.2.2). The coherence fluctuates strongly outside of the envelope. We visualize this envelope by a simple approach: for each point that is not a border point of the total grid, we calculate the variance on the 3×3 map pixels centered on that point and show the result for bands 4 and 1 (9.4–15 and 2.1–4.5 keV) in Fig. 7.9, last panel. The variance of neighboring points is not independent, but our aim here is not a rigorous treatment, but rather pointing out a visible pattern. While we have chosen a cut at a variance of 1, the actual shape of the envelope

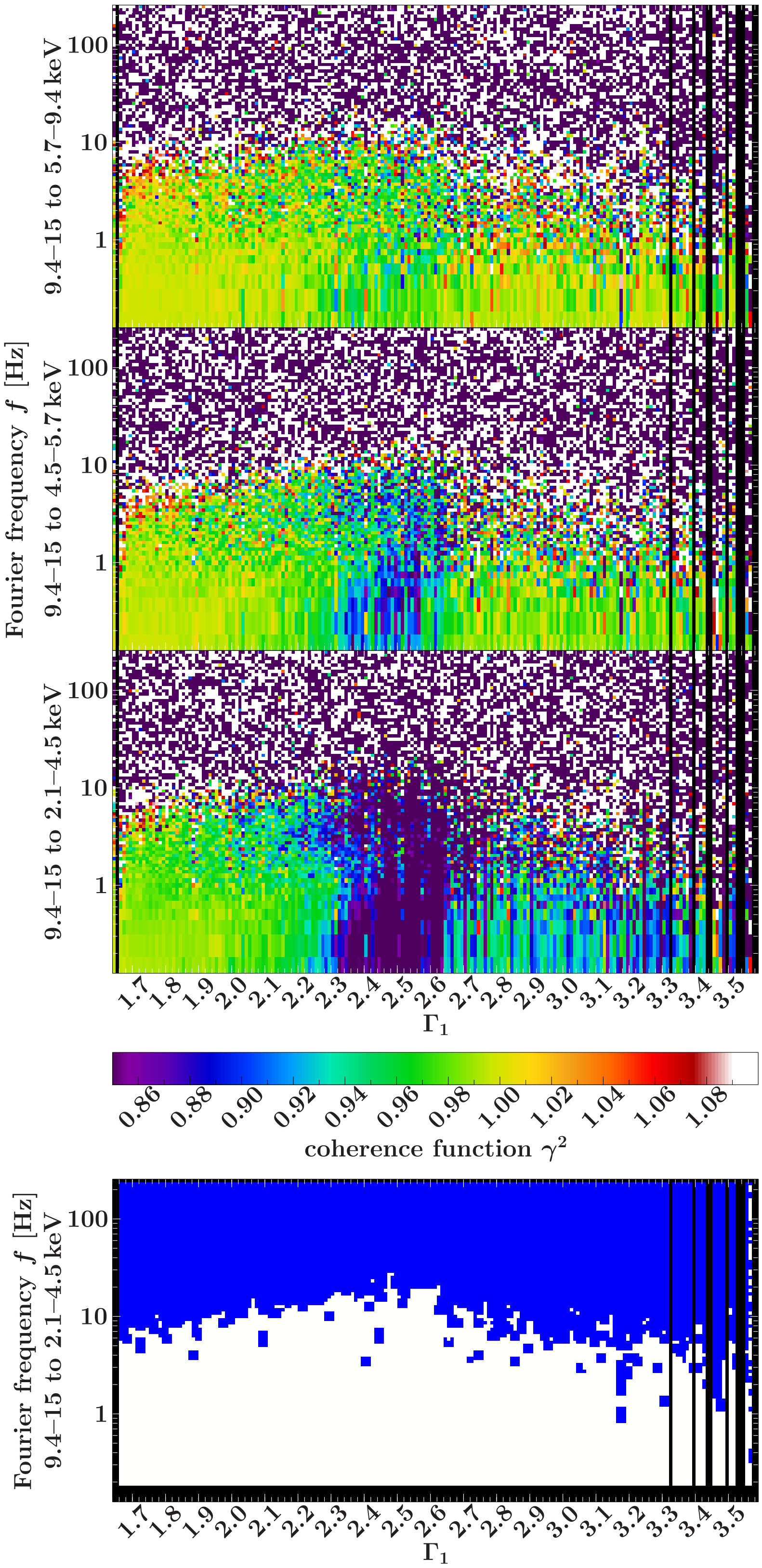

Figure 7.9: *Upper three panels*: Evolution of the coherence, γ^2, with spectral shape represented by the soft photon index Γ_1 of the broken power law. Color scale represents averaged γ^2 values at individual Fourier frequencies f_i. *Lower panel*: The variance of the coherence map between the 9.4–15 and 2.1–4.5 keV energy bands. For calculation see text. White represents variance < 1, blue variance > 1.

hardly changes except for a light shift to higher frequencies for higher values of the cut or to lower frequencies for lower values of the cut for a range of cut-variances as wide as 0.5–10.

The signal at the higher frequencies of the envelope is not coherent. Such a behavior is consistent with the previous finding of a sharp decrease of coherence for Cyg X-1 above a threshold frequency for individual observation (Vaughan & Nowak, 1997; Nowak et al., 1999). Within the envelope, the coherence is, as expected, higher for bands closer in energy.

An interesting feature is the decrease in coherence for $2.35 \lesssim \Gamma_1 \lesssim 2.65$ in a region which seems to follow the shape of the PSD components 1 and 2. This decrease is most evident in $\gamma^2_{4,1}$, where the coherence values drop below 0.85, but is also well visible in $\gamma^2_{4,2}$ and indicated in $\gamma^2_{4,3}$. The variance in this region is low, indicating that the coherence is well defined, in spite of the low values.

For $\Gamma_1 \gtrsim 2.65$, the coherence recovers, although the values between the 9.4–15 keV and 2.5–4.5 keV bands remain significantly lower (~0.92–0.94) than between 9.4–15 keV and the 4.5–5.7 keV and 5.7–9.4 keV bands. The coherence seems noisier, though this may be due to the lower number of observations in the soft state.

7.3.2 Evolution of Fourier-dependent time lags with spectral shape

The time lags show a strong power law dependency on the Fourier frequency with $\delta t(f_i) \propto f_i^{-0.7}$ (Nowak et al., 1999, and references therein), so that we consider the fraction $\delta t(f_i)/f_i^{-0.7} := \Delta\delta t$ to visualize structures in the time lag spectra and again follow the approach from Sect. 7.2.2. We present maps of $\Delta\delta t$ for band combinations showing the largest lags, i.e., bands with largest separation in energy (band 4 and 1, band 4 and 2, and band 3 and 1) in Fig. 7.10. In the phase lag representation, the largest lags between the 2.1–4.5 keV and 9.4–15 keV bands do not exceed ~0.5 rad, so that the time lags are well defined and the features in Fig. 7.10 are not due to the phase lag to time lag conversion (see Sect. 7.1.3).

If the lags followed strictly $\delta t(f_i) \propto f_i^{-0.7}$, then the only structure $\Delta\delta t$ would show would be a gradient with changing Γ_1, corresponding to the known changes in average lag with state (e.g., Pottschmidt et al., 2003). Such a gradient is indeed visible, with the lags obtaining highest values at $\Gamma_1 \sim 2.5$–2.6. For $\Gamma_1 \lesssim 2.7$, however, there is a Fourier frequency-dependent structure which seems to track the two components 1 and 2 of the PSDs (see Sect. 7.2.2) overlaid onto the Γ_1-dependent gradient. This structure is visible for all energy band combinations, but the amplitude of the variation differs and is larger between bands further apart in energy. Such a correlation between the features of the PSDs and of time lag spectra has been suggested in Cyg X-1 by Nowak (2000), but to our knowledge has not been shown for a wide range of spectral states and therefore PSD shapes for any black hole binary previously.

For $\Gamma_1 \gtrsim 2.7$, $\Delta\delta t$ shows no structure and has smaller values than for harder Γ_1. No evolution with Γ_1 can be distinguished in the soft state.

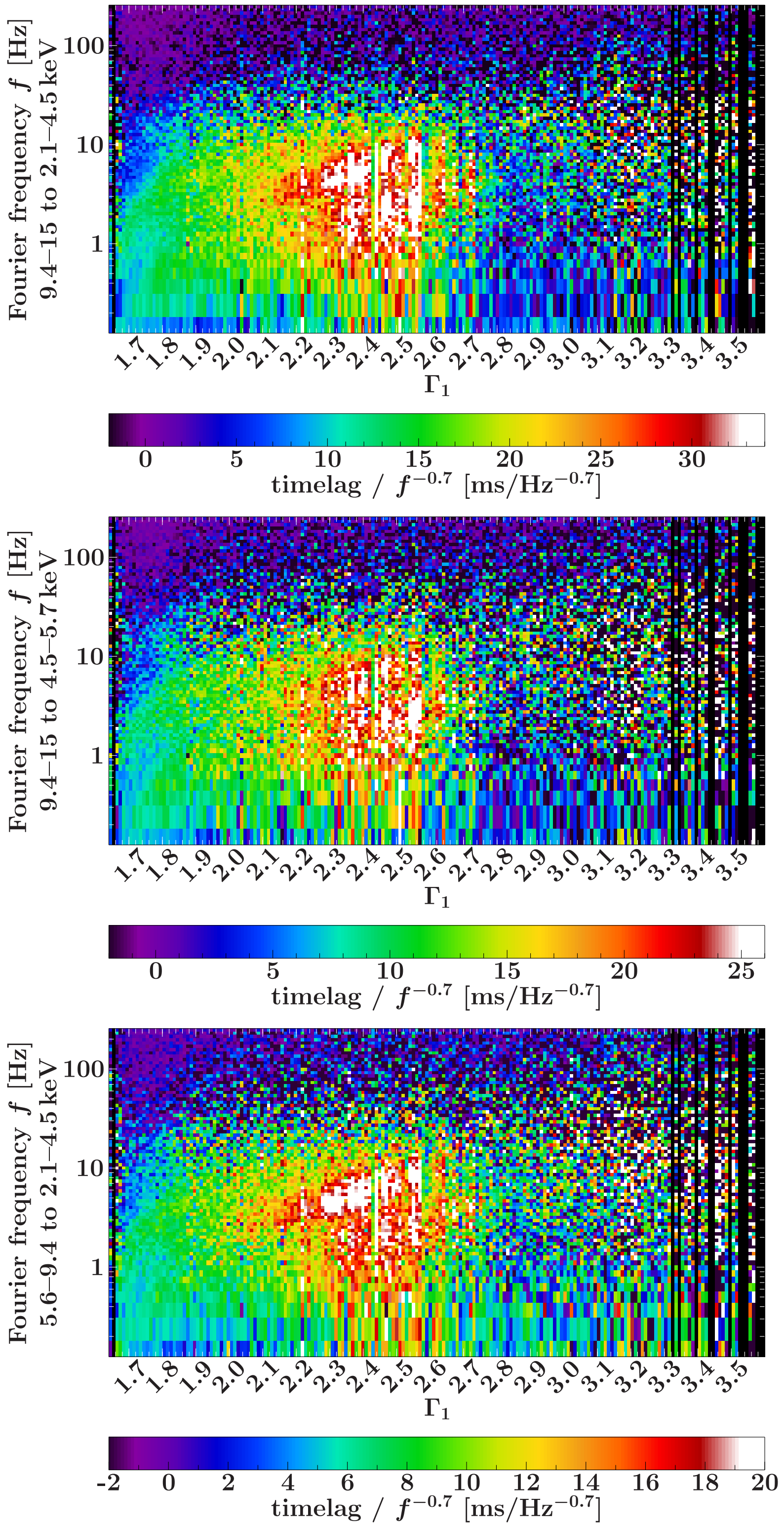

Figure 7.10: Evolution of time lags δt in the $\delta t(f_i)/f_i := \Delta\delta t$ representation with spectral shape represented by the soft photon index Γ_1 of the broken power law. Color scale (note the different scales for the presented bands) represents averaged $\Delta\delta t$ values at individual Fourier frequencies f_i.

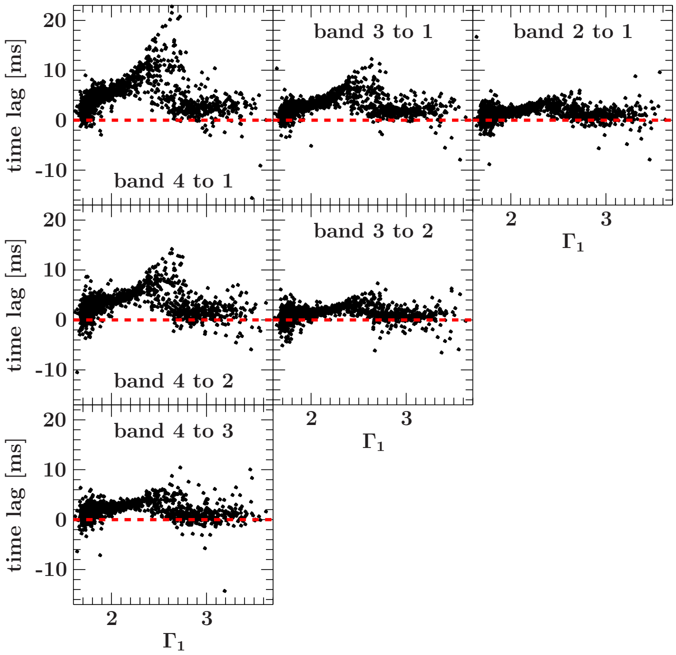

Figure 7.11: Averaged time lag in the 3.2–10 Hz range vs. soft photon index of the broken power law fits Γ_1 for all possible combinations of energy bands (band 1: 2.1–4.5 keV, band 2: 4.5–5.7 keV, band 3: 5.7–9.4 keV, band 4: 9.4–15 keV). Zero time lag is represented by the red dashed line.

Interestingly, at $\Gamma_1 < 1.75$, where the PSDs show increased variability and a possible additional component at higher frequencies, no corresponding changes can be seen in the $\Delta\delta t$ maps. The two components 1 and 2 of the hard and intermediate state PSDs are, however, clearly visible in the time lag maps.

7.3.3 Evolution of average time lag with spectral shape

The usual measure for time lags in the literature are averaged lags δt_{avg} in the 3.2–10 Hz band (e.g., Pottschmidt et al., 2003; Böck et al., 2011). To facilitate comparisons, we follow the approach of the previous work: we rebin each raw time lag spectrum to a logarithmically spaced frequency grid with $\mathrm{d}f/f = 0.15$ and then calculate an average value for the 3.2–10 Hz band.

The average time lags (Fig. 7.11) are larger for bands with a greater difference in energy, but all combinations of energy bands show the same non-linear trends with Γ_1: a strong increase of the time lags from hard to intermediate states and an abrupt drop at $\Gamma_1 \sim 2.65$. The return to low lags in the soft state was already noted by Pottschmidt et al. (2000) as well as in some subsequent work in both Cyg X-1 and other sources.

Spearman rank coefficients for the correlations for $\Gamma_1 < 2.65$ and $\Gamma_1 \geq 2.65$ are listed in Table 7.3. In all bands, δt_{avg} is strongly positively correlated with Γ_1 for $\Gamma_1 < 2.65$ and not correlated or weakly negatively correlated for $\Gamma_1 \geq 2.65$. The weak negative correlation can result from the uncertainties in our determination of the Γ_1 values. Spearman rank coefficients and their low null hypothesis probabilities do, however, not imply a linear correlation: in fact, the correlation for $\Gamma_1 < 2.65$ appears strongly non-linear, with a bend at $\Gamma_1 \sim 1.8$–1.9 and a stronger than linear increase towards higher Γ_1, clearly visible for the lags between band 4 and band 1, i.e., the strongest lags.

Table 7.3: Spearman correlation coefficients ρ and null hypothesis probabilities P for the correlation of averaged time lags in the 3.2–10 Hz band with Γ_1 for different Γ_1 ranges (see also Fig. 7.11).

	band 4 to 1		band 4 to 2		band 4 to 3	
	ρ	P	ρ	P	ρ	P
$\Gamma_1 < 2.65$	0.79	0.00[a]	0.72	0.00[a]	0.65	0.00[a]
$\Gamma_1 \geq 2.65$	−0.14	0.01	−0.12	0.03	−0.06	0.30

	band 3 to 1		band 3 to 2		band 2 to 1	
	ρ	P	ρ	P	ρ	P
$\Gamma_1 < 2.65$	0.3	0.00[a]	0.52	0.00[a]	0.52	0.00[a]
$\Gamma_1 \geq 2.65$	−0.09	0.10	−0.10	0.06	−0.09	0.11

[a] within numerical accuracy

7.3.4 Comparison with previous results for coherence and lags

Cross-spectral analysis is generally less present in the literature and an analysis of the Fourier-dependent coherence function and time lags for Cyg X-1 across the full range of spectral states of the source is undertaken here for the first time. However, the available previous results agree well with the long-term evolution presented here.

Nowak et al. (1999) have observed a loss of coherence above ~10 Hz in the hard state, coincident with the outline of the envelope in our coherence maps (Fig. 7.9). Pottschmidt et al. (2003) and Böck et al. (2011) observed a drop in average coherence in the 3.2–10 Hz range when the source softens, but neither cover soft states with $\Gamma_1 > 2.7$. Cui et al. (1997) observed the Fourier-dependent coherence function for $f_i \lesssim 10$ Hz to have values of ~0.8–0.9 during the transition and to recover to ~1 in the soft state.

An increase of the averaged time lag, δt_{avg}, in the 3.2–10 keV band is well established as a sign for the intermediate state (Pottschmidt et al., 2003; Böck et al., 2011). The return to low values in the soft state has been noted before, but the abruptness of the change can only be seen for an extensive data set such as the one presented.

In a different approach, Skipper et al. (2013) compute the cross correlation function between the photon index and the 3–20 keV count rate and find different shapes in dim hard states, bright hard states and soft states. The hard state CCF can only be explained by a part of the hard count rate lagging the soft, consistent with our observations of a hard lag. The dim hard states correspond to the hardest states observed by Pottschmidt et al. (2003) in 1998, which show, as also our later observations of very hard hard states do, a third variability components in the PSD and correspond to the data before the first bend of the δt_{avg}-Γ_1 correlation at $\Gamma_1 \approx 1.8$ (Sect. 7.3.3). At higher energies, Torii et al. (2011) calculate the cross correlation function between Suzaku light curves in the 10–60 keV and 60–200 keV bands that show evidence of growing hard lags as the source goes from hard into intermediate state.

Miyamoto & Kitamoto (1989) observe a double-humped structure in the phase lag spectra of Cyg X-1, independent of the energy bands in the 1.2–37 keV range used. Correlated features in the PSDs and time lag spectra have been noted for individual observations (Cui et al., 1997; Nowak, 2000), but the systematic evolution of the features with the spectral state has not been addressed before. The importance of this approach becomes apparent when comparing our results to those of Pottschmidt et al. (2000), who discuss time lag spectra for individual observations in different state and argue on their basis for a similar shape of the time lag spectra in hard and soft states. While the $f^{-0.7}$-shape is indeed dominant in both states and individual hard and soft observations therefore appear similar, we see features correlated with PSD components in the hard and but no in the soft state (Fig. 7.10), where the power spectra also do not show pronounced structure.

7.4 A broader view: Cyg X-1 and other sources

7.4.1 Examples of other black hole binaries

The assumption that the variability components in Cyg X-1 trace an underlying pattern common to all black hole binaries or perhaps even all accreting sources, allow to explain some puzzling previous results for sources where no long-term monitoring comparable to Cyg X-1 is available. In the following, we address two examples from the literature, where using the results obtained in Sect. 7.2 as a template for variability leads to alternative interpretation of observations, in particular of features modeled by Lorentzians (for a technical discussion of modeling PSDs with Lorentzian components see Pottschmidt, 2002; Böck, 2008).

XTE J1650−500

Kalemci et al. (2003) report on XTE J1650−500 in outburst decay as it transits from the soft state into the hard state and model the energy-resolved PSDs of the source with Lorentzian components. In their only observation in a deep transitional state, they observe peak frequency of the only Lorenztian component they need to describe their measurements to shift 3.50 ± 0.42 Hz in the 2–6 keV band to 9.70 ± 2.16 Hz in the 6–15 keV band. They identify the Lorentzians in both bands with the same variability component.

However, in Sect. 7.2.2, we have observed that for Cyg X-1 the different energy dependency of the PSD components 1 and 2 may lead, especially at rather soft Γ_1 of 2.5–2.7, to component 1 dominating the soft and component 2 dominating the hard bands. Such a behavior of XTE J1650−500 would explain the results of Kalemci et al. (2003), by invoking two components with different strength in the two energy bands. The poor quality of the PSDs would then allow to satisfactory describe them with the dominant component only.

Swift J1753.5−0127

Cassatella et al. (2012a) discuss XMM observations of Swift J1753.5−0127 in a dim and a bright hard state in the 0.3–0.6 keV, 0.6–1.0 keV, 1.0–2.5 keV, 2.5–4.0 keV, and 4.0–10 keV energy bands, i.e., covering softer energies than accessible with RXTE. Still, the behavior they observe is consistent with the behavior of Cyg X-1 in the RXTE range: in the dim hard state, the power spectra in the different energy bands have about the same normalization and show no clear humps – this is consistent with the behavior of Cyg X-1 in the hardest and at the same time dimmest states (see Fig. 5.4). The bright hard state shows a double humped structure with the same energy dependency as discussed in Sect. 7.2.1: the first hump decreases quicker than the second hump with increasing energy. A step-like structure in the lag spectra is seen coincident with the structure in the PSD and is most pronounces between the bands covering mainly the disk (i.e., below 2.5 keV) and the bands covering mainly the power law (i.e., above 2.5 keV). The similarities between the XMM observations of Swift J1753.5−0127 and RXTE observation of Cyg X-1 lead to the expectation that the both sources should also show similar behavior when both are observed with RXTE.

Soleri et al. (2013) analyze RXTE-PCA data of Swift J1753.5−0127 and fit their PSDs (calculated for the full PCA energy range, i.e., channels 0–249 and ∼2–50 keV) with two Lorentzians. They conclude that the frequency of the Lorentzians is negatively correlated with hardness for all except for the hardest states where the frequency increases without an apparent correlation with hardness. Comparing this behavior with both our analysis of Cyg X-1 and the results of Cassatella et al. (2012a), a misidentification of the component is the likely reasons: a third variability components appears in Cyg X-1 when components 1 and 2 move to lower frequencies and become less pronounces relative to the overall high variability. If Swift J1753.5−0127 shows the same behavior, the sudden frequency shift of the Lorentzians used by Soleri et al. (2013) would mean that they describe different variability components in the hardest states.

7.4.2 AGN

Because of their dimness and the much larger variability timescales and therefore an irregular sampling (see, e.g., Markowitz et al., 2003, for how this problems are addressed), the X-ray timing of AGN is much less well understood than the X-ray timing of black hole binaries. Among the few examples that show the double humped structure typical of hard and intermediate state of BHBs is the Narrow Line Seyfert galaxy Ark 564 that also shows a step in the time lags spectrum at the same frequencies where the dominant component of the power spectra change (McHardy et al., 2007).

Most AGN do, however, not show such a structure (McHardy, 2010). Indeed, the popular notion is that most AGN that are spectroscopically supposed to be hard state sources show PSDs that are more comparable to the soft state PSDs in BHBs. Our results from Sect. 7.2.2 – the strong energy-dependency of the PSD shapes for most except the hardest states (Fig. 7.7) and the similarity of the PSD shapes at higher energies for the hardest states and the soft states (Fig. 7.8) – may challenge this idea, although a more detailed analysis is required. In particular, any comparison between AGN and black hole binaries has to take the mass-scaling into account and therefore the fact that the same energies probe different processes in sources of different mass. An energy-resolved approach to power spectra (although complicated for AGN because of their low signal) is therefore crucial.

7.5 Physical models for X-ray variability

A number of different physical models for X-ray variability exists in literature, partly based on fundamentally different assumptions on X-ray emitting geometry (see, e.g. Cassatella et al., 2012b, and references therein for an overview). Most of the models can, however, either not be directly statistically compared to data yet or are known to be yet strongly limited by the underlying assumptions and the computational costs. The purpose of this Chapter is not to offer a valid model, but to summarize the spectro-timing evolution for an extraordinarily well studied source in order to create a template that models for X-ray timing variability can be tested against. In this Section, we therefore outline some of the theoretical approaches in the light of the presented observational results.

Körding & Falcke (2004) explain the Fourier-dependents time lags using a pivoting power law without explicit assumptions on its physical origin. Such a power law could easily originate in jets, but is also possible for corona models. They assume that the PSDs can be decomposed into individual Lorentzians and are so able to reproduce structures in time lag spectra that are correlated to structures in the PSDs. Their model is, to our knowledge, the only one that can reproduce the correlated structures, which we have shown to exist over the full range of hard and intermediate states (Sect. 7.3.2). However, it is only valid for hard state. State transitions and soft states have not yet been addressed.

A jet and the time photons spend within the jet is the basis of the model introduced by Reig et al. (2003) and further developed by Giannios et al. (2004) and Kylafis et al. (2008). Their work does not explicitly address power spectra, but can reproduce the $f^{-0.7}$ shape of the time lag spectrum (Reig et al., 2003); the hardening of the PSDs with increasing energy, which corresponds to the increased contribution of component 2 to the PSDs with increasing energy as observed in Sect 7.2.2 (Giannios et al., 2004); and the shape and normalization of the δt_{avg}-Γ correlation in Cyg X-1 of Pottschmidt et al. (2003) in hard and intermediate states. This jet model can only be applied to the soft state if the jet still exists and only its radio emission is strongly suppressed. However, the lacking structure in the time lags in the soft state in Cyg X-1 (see Fig. 7.10) and the abrupt changes of the absolute lag values at the intermediate to soft state (see Fig. 7.10 and Fig. 7.11) transition make it probable that at least a part of the time lags have a different origin in the hard than in the soft state. Additional problems of this model, i.e., its inability to explain the soft lags at timescales of >1 s at soft energies that are dominated by the accretion disk and not accessible with RXTE, are discussed by Uttley et al. (2011).

In a different approach building on the work of Psaltis & Norman (2000), Ingram &

Done (2011, 2012) and Ingram & van der Klis (2013) assume the truncated disk model for states (see Fig. 1.2) and consider mass accretion rate fluctuations that are stirred up far away from the black hole and propagate close to the black hole. The model can roughly reproduce the PSD shapes in the hard state and the shape of the time lag spectra – however, the power spectra are smooth and the double humped structure and accordingly also the correlated structure in the time lags are missing. Such effects could be incorporated by including the disk variability (Wilkinson & Uttley, 2009) or further magneto-rotational instability effects (Ingram & van der Klis, 2013).

None of the discussed models can explain the full bandwidth of the X-ray timing phenomena. While individual observations showing, e.g., correlated structure in the power spectra and time lags, could be seen as special cases, the systematic analysis presented in this work hints that the complexity of the behavior and the interrelations of the different spectral and timing-quantities are basic features of the underlying physical processes and have to be addressed by any model to be successful in describing BHBs.

7.6 Summary

Using 13 years of RXTE bi-weekly monitoring of Cyg X-1 we have provided the most comprehensive X-ray timing study of a black hole binary to date and provided a template for detailed evolution of rms, power spectra, Fourier-resolved coherence and time lags and well as averaged time lags across all spectral state. The so gained detailed knowledge of the evolution of variability with spectral shape can be used to better understand individual observations (Sect. 7.4) and theoretical models (Sect. 7.5) not only for Cyg X-1, but for all BHBs.

In particular, we have shown that the fractional rms and components of the power spectra depend strongly on the energy band used (Sect. 7.2), a fact that needs to be taken into account when comparing these quantities across different object types and that has to be incorporated into theoretical models explaining the origin of X-ray variability. In Sect. 7.2.2, we have shown that the model-independent approach we choose enables us to track variability components in the PSDs as they change with the spectral shape and avoid the pitfalls of component confusion (Sect. 7.4.1). We stress the different behavior of the PSDs in the hardest observations: the third variability component, the similarity of the shapes in the presented energy bands, and a generally less pronounced structure. We were able to track the correlations between the shapes of time lag spectra and PSDs that have so far been noted only for individual cases (Sect. 7.3.2). This behavior hints on a fundamental relation between both properties. We have also shown that at a soft photon index Γ_1 of $\sim$2.6–2.7 all X-ray timing quantities show strong changes, indicating a transition in the dominant source of X-rays with the considered energies.

The analysis presented here stresses that a holistic empirical approach that takes spectral and timing evolution of the source into account, is imperative for the understanding of black hole binaries, both from an observational and from a theoretical perspective.

It is impossible, by the way, when picking one example of anything, to avoid picking one which is atypical in some sense.

(Richard P. Feynman)

8 Summary and outlook

In this work, we have addressed the long term evolution of black hole binaries using Cyg X-1 as a representative for the whole class of objects. In the following, we summarize the main results and point out directions for possible future investigation, both using Cyg X-1 and transferring methods and ideas developed in this thesis to other sources.

- In Chapter 3 we have shown that timing and spectral data can be used to recognize state transitions and outbursts in both persistent (Cyg X-1) and transient (H1743−322) sources. The near real time analysis presented in this Chapter is crucial for enabling follow up observations. While RXTE is now defunct, INTEGRAL is alive and well and thus can and will be used to continue the monitoring of black hole binaries.
- In Chapter 4, we have used 16 years of RXTE observations of Cyg X-1 for an analysis of the long-term evolution of spectral properties, with a focus on the orbital variability of absorption. We have used empirical models and have confirmed previous results on correlations between spectral features using a higher number of observations with a better coverage of intermediate and soft states. The orbital variability of absorption that we see confirms the clumpy wind paradigm for the stellar wind of HDE 226868, the companion star of the black hole.
- The empirical spectral models of Chapter 4 are the basis for a future analysis of the campaign with more complex and therefore more computationally intensive physically motivated models, especially with Comptonization models such as `comptt` (Titarchuk, 1994; Titarchuk & Lyubarskij, 1995; Titarchuk & Hua, 1995) and `eqpair` (Coppi, 1999, 2004), and the `agnjet` jet model (Markoff et al., 2005; Maitra et al., 2009). While both, the corona- and the jet-based models, can explain individual observations, systematic analysis of long term evolution may favor the one or the other model.

- The findings of Chapter 4 are a first step towards a more detailed analysis of the orbital modulations of wind with RXTE. While RXTE-based spectral and timing studies mainly probe the vicinity of the black hole, here we can use the black hole as a probe for the stellar wind of an O-type super giant and contribute to the understanding not only of the accretion/ejection in black holes, but also of high mass stars and their mass loss. Planned are statistical comparisons of the long-term variability of absorption with detailed simulations of clumpy stellar winds. This approach is complimentary to the high resolution snapshot observations with current missions like Chandra and future missions like the planned Athena+ (Nandra et al., 2013), a contender for the L2 and L3 launching spots in the ESA Science program.
- In Chapter 5, we have developed a novel method to classify all sky monitor observations of black hole binaries by mapping X-ray spectral states obtained from detailed modeling of pointed RXTE observations on RXTE-ASM, MAXI, and Fermi-GBM hardness-intensity-diagrams as well as Swift-BAT light curves (Sect. 5.2). This method has allowed us to analyze the occurrence and stability of states in Cyg X-1 over more than 17 years (Sect. 5.3), including periods of different source activity. Generally, we find that the intermediate state is much less stable than both hard and soft states. A detailed listing of state occurrences in different activity periods of the source is presented in Table 5.3.
- An important advantage of the classification presented in Chapter 5 is its usability: states are defined as simple cuts in hardness-intensity parameter space in publicly available data (Table 5.2) and therefore easily accessible. It was already utilized by, e.g., Bodaghee et al. (2013) for a state-classification of the times of γ-ray detections of Cyg X-1 with the Fermi-LAT instrument. The classification can help observers and operators of relevant missions to easily propose for and assess the value of target of opportunity observations of Cyg X-1 and, once developed, other sources.
- The methodology of analyzing, comparing, and interpreting the data from different all sky monitors presented in great detail in Chapter 5 will help to jump-start similar investigations for other sources than Cyg X-1, with galactic (both, black hole and neutron star binaries) and extragalactic sources (AGN) as possible targets. The approach may further prove useful for future missions, e.g., the planned eROSITA instrument and its years-long all-sky survey (Merloni et al., 2012) or the MIRAX mission and its hard X-ray survey (Braga et al., 2012).
- In Chapter 6, we have used the method of Chapter 5 to classify individual XMM and Chandra observations of Cyg X-1 in order to be able to place them in a greater context of source behavior (Sect. 6.1). In Sect. 6.2, we have used this approach to classify over 3300 individual INTEGRAL Science Windows of Cyg X-1 observations into hard, intermediate and soft states in order to be able to carry out state-resolved polarization analysis. This analysis will shed light on the behavior of the polarized hard tail in different spectral states. We have presented the preliminary INTEGRAL-IBIS spectra we obtained; further spectral and polarization analysis is work in progress and shall be published by Rodriguez et al., 2013.

- In Chapter 7, we have used a unique RXTE data set of Cyg X-1 spanning 13 years of bi-weekly observations and conducted the most comprehensive X-ray timing study of any black hole binary to date. Especially, we addressed three questions. First, we analyzed the energy-dependent evolution of rms and power spectra with spectral shape, where we have shown that an energy-dependent approach is crucial for disentangling the variability of sources at different spectral shapes. Secondly, we considered the Fourier-dependent evolution of the coherence and time lags with spectral shape, where we have shown that both quantities show strong changes at $\Gamma_1 \approx 2.7$, possibly indicative of changes in the geometry of the accretion and ejection flows. Thirdly, we examined the correlations between features in Fourier-dependent cross-spectral quantities and in the power spectra at different spectral shapes, which previously have been indicated for individual observations and which we have shown to exist across a wide range of observation and to strongly depend on spectral shape.
- We have additionally shown how the knowledge gained on the example of Cyg X-1 in Chapter 7 can be used to interpret some puzzling results obtained previously for other sources and have addressed questions it poses for the theoretical models that try to explain the X-ray variability of black hole binaries by assuming different accretion and ejection geometries. Our results emphasize the need for long-term studies as a basis for the interpretation of snapshot observations.
- The results of Chapter 7 also highlight the importance of the proper treatment of the energy-dependency of the variability when comparing sources of different mass, especially black hole binaries and AGN, since the same energies may probe different processes in such sources. A systematic comparison taking into account the energy-dependency remains to be attempted in the future.
- While the data set of Cyg X-1 used in Chapter 7 is unique in its length and quality, some RXTE coverage in modes that enable energy-resolved timing analysis exists also for other sources such as GX 339−4. An analysis of these data with a focus on differences and similarities to Cyg X-1 is a logical next step towards a holistic description of the variability of black hole binaries in different spectral states. Such a detailed analysis of archival data will serve as a step stone for future missions focused on X-ray timing, particularly the LOFT satellite (e.g., Bozzo & LOFT Consortium, 2012)[1] that is currently competing for a launching spot within ESA's Cosmic Vision Programme.

The focus of this work was on the interrelations of different properties from the spectral, timing and polarization domains, which are not yet well understood even observationally for one of the prime targets of black hole binary research. We made important steps towards a holistic description, even though many questions still remain open. And while, to address the wise words of Richard P. Feynman starting this summary, Cygnus X-1, the example picked out for most of the presented work, may be an atypical one in some regards – for example being a system fed by a focused wind –, it is surely a typical example for the complexity of this, and perhaps any, astrophysical problem. And for the

---

[1] For current information on LOFT see also `http://www.isdc.unige.ch/loft`

plethora or questions and wonders still awaiting us among the stars (and dead stars, i.e., back holes).

References

Arnaud K., Smith R., Siemiginowska A., 2011, Handbook of X-ray Astronomy, Cambridge Observing Handbooks for Research Astronomers, Vol. 7, Cambridge University Press

Arnaud K.A., 1996, In: Jacoby G.H., Barnes J. (eds.) Astronomical Data Analysis Software and Systems V. Astronomical Society of the Pacific Conference Series, Vol. 101, p. 17

Axelsson M., Borgonovo L., Larsson S., 2005, A&A 438, 999

Axelsson M., Borgonovo L., Larsson S., 2006, A&A 452, 975

Balbus S.A., Hawley J.F., 1991, ApJ 376, 214

Balbus S.A., Hawley J.F., 1992, ApJ 400, 610

Bałucińska-Church M., Church M.J., Charles P.A., et al., 2000, MNRAS 311, 861

Barlow R., 1989, Statistics. A Guide to the Use of Statistical Methods in the Physical Sciences, The Manchester Physics Series, New York, Wiley

Barthelmy S.D., Barbier L.M., Cummings J.R., et al., 2005, Space Sci. Rev. 120, 143

Baumgartner W.H., Tueller J., Markwardt C.B., et al., 2013, ApJS 207, 19

Becker W., Bernhardt M.G., Jessner A., 2013, arXiv:1305.4842, to be published in the proceedings of the workshop ‘Relativistic Positioning Systems and their Scientific Applications’

Belloni T., Cadolle Bel M., Casella P., et al., 2012, ATel 4450

Belloni T., Hasinger G., 1990, A&A 227, L33

Belloni T., van der Klis M., Lewin W.H.G., et al., 1997, A&A 322, 857

Belloni T.M., 2010, In: T. Belloni (ed.) The Jet Paradigm: From Microquasars to Quasars, Lecture Notes in Physics, Berlin Springer Verlag, Vol. 794., p. 53

Beloborodov A.M., 1999, ApJ 510, L123

Bendat J.S., Piersol A.G., 2010, Random Data, Analysis and Measurements Procedures, Fourth Edition, John Wiley & Sons, Inc., Hoboken

Benlloch S., Pottschmidt K., Wilms J., et al., 2004, In: Kaaret P., Lamb F.K., Swank J.H. (eds.) X-ray Timing 2003: Rossi and Beyond. AIP Conf. Ser. 714, p.61

Bird A.J., Bazzano A., Bassani L., et al., 2010, ApJS 186, 1

Bissaldi E., von Kienlin A., Lichti G., et al., 2009, Experimental Astronomy 24, 47

Blaes O., 2013, Space Sci. Rev.

Blandford R.D., Payne D.G., 1982, MNRAS 199, 883

Blandford R.D., Znajek R.L., 1977, MNRAS 179, 433

Böck M., 2008, Diploma thesis, Universität Erlangen-Nürnberg

Böck M., Grinberg V., Pottschmidt K., et al., 2011, A&A 533, A8

Böck M., Wilms J., Markoff S., et al., 2008, In: VII Microquasar Workshop: Microquasars and Beyond, PoS, p. 89.

Bodaghee A., Tomsick J.A., Pottschmidt K., et al., 2013, ApJ in press

Bolton C.T., 1972, Nat 235, 271

Bondi H., 1952, MNRAS 112, 195

Bondi H., Hoyle F., 1944, MNRAS 104, 273

Boroson B., Vrtilek S.D., 2010, ApJ 710, 197

Bowyer S., Byram E.T., Chubb T.A., Friedman H., 1965, Science 147, 394

Box G.E.P., Draper N.R., 1987, Empirical Model Building and Response Surfaces, John Wiley & Sons, New York, NY.

Bozzo E., LOFT Consortium 2012, In: Proceedings of ”An INTEGRAL view of the high-energy sky (the first 10 years)” - 9th INTEGRAL Workshop, PoS, id.141.

Bradt H.V., Rothschild R.E., Swank J.H., 1993, A&AS 97, 355

Braga J., Grindlay J., Rothschild R., et al., 2012, In: Half a Century of X-ray Astronomy.

Brocksopp C., Fender R.P., Larionov V., et al., 1999a, MNRAS 309, 1063

Brocksopp C., Tarasov A.E., Lyuty V.M., Roche P., 1999b, A&A 343, 861

Bulgarelli A., Pittori C., Lucarelli F., et al., 2010, ATel 2512

Cabanac C., Roques J.P., Jourdain E., 2011, ApJ 739, 58

Cadolle Bel M., Sizun P., Goldwurm A., et al., 2006, A&A 446, 591

Canizares C.R., Davis J.E., Dewey D., et al., 2005, PASP 117, 1144

Carroll B.W., Ostlie D.A., 2007, An Introduction to Modern Astrophysics and Cosmology, Second Edition, Pearson Education, Addison Weasley, San Francisco

Carter B., 1971, Phys. Rev. Lett. 26, 331

Case G.L., Cherry M.L., Wilson-Hodge C.A., et al. 2011, ApJ 729, 105

Cassatella P., Uttley P., Maccarone T.J., 2012a, MNRAS 427, 2985

Cassatella P., Uttley P., Wilms J., Poutanen J., 2012b, MNRAS 422, 2407

Castor J.I., Abbott D.C., Klein R.I., 1975, ApJ 195, 157

Chernyakova M., Neronov A., Pavan L., Türler M., 2012, IBIS Analysis User Manual 10.0

Coe M.J., 2000, In: Smith M.A., Henrichs H.F., Fabregat J. (eds.) IAU Colloq. 175: The Be Phenomenon in Early-Type Stars. Astronomical Society of the Pacific Conference Series, Vol. 214, p. 656

Coe M.J., Engel A.R., Quenby J.J., 1976, Nat 259, 544

Conti P.S., 1978, A&A 63, 225

Coppi P., 2004, In: Kaaret P., Lamb F.K., Swank J.H. (eds.) X-ray Timing 2003: Rossi and Beyond, Vol. 714. American Institute of Physics Conference Series, p.79

Coppi P.S., 1999, In: J. Poutanen & R. Svensson (ed.) High Energy Processes in Accreting Black Holes. Astronomical Society of the Pacific Conference Series, Vol. 161, p.375

Coriat M., Corbel S., Prat L., et al., 2011, MNRAS 414, 677

Courvoisier T., Walter R., Beckmann V., et al., 2003, A&A 411, L53

Cui W., Zhang S.N., Focke W., Swank J.H., 1997, ApJ 484, 383

Dauser T., Wilms J., Reynolds C.S., Brenneman L.W., 2010, MNRAS 409, 1534

Del Santo M., Malzac J., Belmont R., et al., 2013, MNRAS 430, 209

Dove J.B., Wilms J., Maisack M., Begelman M.C., 1997, ApJ 487, 759

Droulans R., Belmont R., Malzac J., Jourdain E., 2010, ApJ 717

Dunn R.J.H., Fender R.P., Körding E.G., et al., 2010, MNRAS 403, 61

Dunn R.J.H., Fender R.P., Körding E.G., et al., 2011, MNRAS 411, 337

Duro R., Dauser T., Grinberg V., et al., 2013, A&A , to be submitted

Duro R., Dauser T., Wilms J., et al., 2011, A&A 533, L3

Evangelista Y., Campana R., Del Monte E., et al., 2010, ATel 2724

Fabian A.C., Wilkins D.R., Miller J.M., et al., 2012, MNRAS 424, 217

Falcke H., Körding E., Markoff S., 2004, A&A 414, 895

Fender R., 2006, In: Lewin W.H.G., van der Klis M. (eds.) Compact stellar X-ray sources. Cambridge Astrophysics Series, Vol. 39, Cambridge University Press, p.381

Fender R., 2010, In: T. Belloni (ed.) The Jet Paradigm: From Microquasars to Quasars, Lecture Notes in Physics, Berlin Springer Verlag, Vol. 794., p.115

Fender R.P., 2001, MNRAS 322, 31

Fender R.P., Belloni T.M., Gallo E., 2004, MNRAS 355, 1105

Fender R.P., Gallo E., Russell D., 2010, MNRAS 406, 1425

Fender R.P., Homan J., Belloni T.M., 2009, MNRAS 396, 1370

Fender R.P., Maccarone T.J., Heywood I., 2013, MNRAS 430, 1538

Ferrarese L., Merritt D., 2000, ApJ 539, L9

Ferreira J., Petrucci P.O., Henri G., et al., 2006, A&A 447, 813

Forot M., Laurent P., Grenier I.A., et al., 2008, ApJ 688, L29

Forot M., Laurent P., Lebrun F., Limousin O., 2007, ApJ 668, 1259

Fragile P.C., 2013, Space Sci. Rev.

Fragile P.C., Meier D.L., 2009, ApJ 693, 771

Frank J., King A., Raine D.J., 2002, Accretion Power in Astrophysics: Third Edition, Cambridge University Press

Friend D.B., Castor J.I., 1982, ApJ 261, 293

Fritz S., 2008, Ph.D. thesis, Universität Tübingen

Fürst F., 2011, Ph.D. thesis, Universität Erlangen-Nürnberg

Fürst F., Kreykenbohm I., Pottschmidt K., et al., 2010, A&A 519

Fürst F., Wilms J., Rothschild R.E., et al., 2009, Earth and Planetary Science Letters 281, 125

Gallo E., 2010, In: T. Belloni (ed.) The Jet Paradigm: From Microquasars to Quasars, Lecture Notes in Physics, Berlin Springer Verlag, Vol. 794., p.85

Gallo E., Fender R., Kaiser C., et al., 2005, Nat 436, 819

Gallo E., Marolf D., 2009, American Journal of Physics 77, 294

Gebhardt K., Bender R., Bower G., et al., 2000, ApJ 539, L13

Gehrels N., 1986, ApJ 303, 336

Gehrels N., Chincarini G., Giommi P., et al., 2004, ApJ 611, 1005

Giannios D., Kylafis N.D., Psaltis D., 2004, A&A 425, 163

Gierliński M., Nikołajuk M., Czerny B., 2008, MNRAS 383, 741

Gierliński M., Zdziarski A.A., Done C., 2010, In: Giovannelli F., Mannocchi G. (eds.) Frontier Objects in Astrophysics and Particle Physics, Vol. 203. Italian Physical Soc. Conf. Proc., p.299

Gies D.R., Bolton C.T., 1982, ApJ 260, 240

Gies D.R., Bolton C.T., 1986a, ApJ 304, 371

Gies D.R., Bolton C.T., 1986b, ApJ 304, 389

Gies D.R., Bolton C.T., Blake R.M., et al., 2008, ApJ 678, 1237

Gies D.R., Bolton C.T., Thomson J.R., et al., 2003, ApJ 583, 424

Gilfanov M., Churazov E., Revnivtsev M., 1999, A&A 352, 182

Gleissner T., Wilms J., Pooley G.G., et al., 2004a, A&A 425, 1061

Gleissner T., Wilms J., Pottschmidt K., et al., 2004b, A&A 414, 1091

Goldwurm A., David P., Foschini L., et al., 2003, A&A 411, L223

Götz D., Covino S., Fernández-Soto A., et al., 2013, MNRAS 431, 3550

Götz D., Laurent P., Lebrun F., et al., 2009, ApJ 695, L208

Gou L., McClintock J.E., Reid M.J., et al., 2011, ApJ 742, 85

Grainge K., Alexander P., Battye R., et al., 2012, AMI white paper, arXiv:1208.1966

Grinberg V., 2010, Diploma thesis, Ludwig-Maximilians-Universität, München

Grinberg V., Böck M., Pottschmidt K., et al., 2010, ATel 2751

Grinberg V., Böck M., Pottschmidt K., et al., 2011a, ATel 3307

Grinberg V., Böck M., Pottschmidt K., et al., 2011b, ATel 3616

Grinberg V., Hell N., Pottschmidt K., et al., 2013, A&A 554, A88

Grinberg V., Kreykenbohm I., Fürst F., et al., 2011c, Acta Polytechnica 51/2, 33

Grinberg V., Rodriguez J., Wilms J., et al., 2012, ATel 4418

Haardt F., Maraschi L., 1991, ApJ 380, L51

Hanke M., 2007, Diploma thesis, Universität Erlangen-Nürnberg

Hanke M., 2011, Ph.D. thesis, Universität Erlangen-Nürnberg

Hanke M., Wilms J., Nowak M.A., et al., 2009, ApJ 690, 330

Harmon B.A., Fishman G.J., Wilson C.A., et al., 2002, ApJS 138, 149

Hawking S.W., 1972, Communications in Mathematical Physics 25, 152

Hawley J.F., Balbus S.A., 1991, ApJ 377, 233

Hawley J.F., Balbus S.A., 1992, ApJ 400, 595

Herrero A., Kudritzki R.P., Gabler R., et al., 1995, A&A 297, 556

Hjellming R.M., Wade C.M., 1971, ApJ 168, L21

Hoover A.S., Kippen R.M., Wallace M.S., et al., 2008, In: Galassi M., Palmer D., Fenimore E. (eds.) Gamma-ray bursts 2007: Proceedings of the Santa Fe Conference, AIP Conference Series, Vol. 1000., p.565

Horne J.H., Baliunas S.L., 1986, ApJ 302, 757

Houck J.C., 2002, In: G. Branduardi-Raymont (ed.) High Resolution X-ray Spectroscopy with XMM-Newton and Chandra.

Houck J.C., Denicola L.A., 2000, In: Manset N., Veillet C., Crabtree D. (eds.) Astronomical Data Analysis Software and Systems IX. ASP Conf. Ser. 216, p. 591

Ibragimov A., Poutanen J., Gilfanov M., et al., 2005, MNRAS 362, 1435

Ibragimov A., Zdziarski A.A., Poutanen J., 2007, MNRAS 381, 723

Ingram A., Done C., 2011, MNRAS 415, 2323

Ingram A., Done C., 2012, MNRAS 419, 2369

Ingram A., van der Klis M., 2013, MNRAS

in't Zand J.J.M., 1992, Ph.D. thesis, Space Research Organization Netherlands, Utrecht

Israel W., 1967, Phys. Rev. 164, 1776

Israel W., 1968, Communications in Mathematical Physics 8, 245

Jahoda K., Markwardt C.B., Radeva Y., et al., 2006, ApJS 163, 401

Jahoda K., Swank J.H., Giles A.B., et al., 1996, In: O. H. Siegmund & M. A. Gummin (ed.) EUV, X-Ray, and Gamma-Ray Instrumentation for Astronomy VII, SPIE Conference Series, Vol. 2808., p.59

Jourdain E., Roques J.P., Chauvin M., Clark D.J., 2012, ApJ 761, 27

Kalemci E., Tomsick J.A., Rothschild R.E., et al., 2003, ApJ 586, 419

Kerr R.P., 1963, Phys. Rev. Letters 11, 237

Kitamoto S., Miyamoto S., Tanaka Y., et al., 1984, PASJ 36, 731

Kitamoto S., Tsunemi H., Miyamoto S., Hayashida K., 1992, ApJ 394, 609

Klein-Wolt M., van der Klis M., 2008, ApJ 675, 1407

Körding E., Falcke H., 2004, A&A 414, 795

Körding E., Rupen M., Knigge C., et al., 2008, Science 320, 1318

Körding E.G., Jester S., Fender R., 2006, MNRAS 372, 1366

Krauss F., 2013, Master's thesis, Universität Erlangen-Nürnberg

Kreykenbohm I., 2004, Ph.D. thesis, Universität Tübingen

Krivonos R., Tsygankov S., Revnivtsev M., et al., 2010, A&A 523, A61

Kylafis N.D., Papadakis I.E., Reig P., et al., 2008, A&A 489, 481

Labanti C., Di Cocco G., Ferro G., et al., 2003, A&A 411, L149

Lagrange J.L., 1772, Prix de l'Académie Royale des Sciences de Paris tome IX

Laurent P., Götz D., Binétruy P., et al., 2011a, Phys. Rev. D 83, 121301

Laurent P., Götz D., Gouiffes C., et al., 2012, In: Proceedings of "An INTEGRAL view of the high-energy sky (the first 10 years)" - 9th INTEGRAL Workshop, PoS, id.5.

Laurent P., Limousin O., Cadolle-Bel M., et al., 2003, A&A 411, L185

Laurent P., Rodriguez J., Wilms J., et al., 2011b, Science 332, 438

Laurent P., Titarchuk L., 2007, ApJ 656, 1056

Learned J.G., Kudritzki R., Pakvasa S., Zee A., 2008, arXiv:0809.0339

Lebrun F., Leray J.P., Lavocat P., et al., 2003, A&A 411, L141

Lei F., Dean A.J., Hills G.L., 1997, Space Sci. Rev. 82, 309

Levine A.M., Bradt H., Cui W., et al., 1996, ApJ 469, L33

Li F.K., Clark G.W., 1974, ApJ 191, L27

Lund N., Budtz-Jørgensen C., Westergaard N.J., et al., 2003, A&A 411, L231

Maitra D., Markoff S., Brocksopp C., et al., 2009, MNRAS 398, 1638

Makishima K., Maejima Y., Mitsuda K., et al., 1986, ApJ 308, 635

Malzac J., Jourdain E., 2000, A&A 359, 843

Markoff S., 2010, In: T. Belloni (ed.) The Jet Paradigm: From Microquasars to Quasars, Lecture Notes in Physics, Berlin Springer Verlag, Vol. 794., p.143

Markoff S., Nowak M.A., Wilms J., 2005, ApJ 635, 1203

Markowitz A., Edelson R., Vaughan S., et al., 2003, ApJ 593, 96

Mas-Hesse J.M., Giménez A., Culhane J.L., et al., 2003, A&A 411, L261

Mason K.O., Hawkins F.J., Sanford P.W., et al., 1974, ApJ 192, L65

Matsuoka M., Kawasaki K., Ueno S., et al., 2009, PASJ 61, 999

McClintock J.E., Remillard R.A., 2006, In: Compact Stellar X-ray Sources., Cambridge University Press, p.157

McConnell M.L., Ryan J.M., Collmar W., et al., 2000, ApJ 543, 928

McConnell M.L., Zdziarski A.A., Bennett K., et al., 2002, ApJ 572

McHardy I., 2010, In: Belloni T. (ed.) Lecture Notes in Physics, Berlin Springer Verlag, Vol. 794. Lecture Notes in Physics, Berlin Springer Verlag, p. 203

McHardy I.M., Arévalo P., Uttley P., et al., 2007, MNRAS 382, 985

McHardy I.M., Koerding E., Knigge C., et al., 2006, Nat 444, 730

McKinney J.C., 2006, MNRAS 368, 1561

McKinney J.C., Blandford R.D., 2009, MNRAS 394, L126

Meegan C., Bhat N., Connaughton V., et al., 2007, In: Ritz S., Michelson P., Meegan C.A. (eds.) The First GLAST Symposium. AIP Conf. Ser. 921, p.13

Meegan C., Lichti G., Bhat P.N., et al., 2009, ApJ 702, 791

Merloni A., Heinz S., di Matteo T., 2003, MNRAS 345, 1057

Merloni A., Körding E., Heinz S., et al., 2006, New Astronomy 11, 567

Merloni A., Predehl P., Becker W., et al., 2012, "eROSITA Science Book: Mapping the Structure of the Energetic Universe", arXiv:1209.3114

Mihara T., Nakajima M., Sugizaki M., et al., 2011, PASJ 63, 623

Miller J.M., Fabian A.C., Wijnands R., et al., 2002, ApJ 578, 348

Mirabel I.F., Dijkstra M., Laurent P., et al., 2011, A&A 528, A149

Mitsuda K., Inoue H., Koyama K., et al., 1984, PASJ 36, 741

Miškovičová I., Hell N., Hanke M., et al., 2013, A&A , submitted

Miyamoto S., Kimura K., Kitamoto S., et al., 1991, ApJ 383, 784

Miyamoto S., Kitamoto S., 1989, Nat 342, 773

Moorcock M., Simonson W., Reeve M., Ridgway J., 1999, Michael Moorcock's Multiverse, DC Comics, New York

Motta S., Belloni T., Homan J., 2009, MNRAS 400, 1603

Muñoz-Darias T., Motta S., Belloni T.M., 2011, MNRAS 410, 679

Muñoz-Darias T., Motta S., Pawar D., et al., 2010, MNRAS 404, L94

Murdin P., Webster B.L., 1971, Nat 233, 110

Nandra K., Barret D., Barcons X., et al., 2013, Athena+ white paper; arXiv:1306.2307

Negoro H., Asada M., Sakakibara H., et al., 2011, ATel 3534

Negoro H., Kawai N., Kawasaki Y.U.K., et al., 2010, ATel 2711

Neilsen J., 2013, Advances in Space Research 52, 732

Ninkov Z., Walker G.A.H., Yang S., 1987, ApJ 321, 438

Noble M.S., Nowak M.A., 2008, PASP 120, 821

Nowak M.A., 2000, MNRAS 318, 361

Nowak M.A., 2008, In: VII Microquasar Workshop: Microquasars and Beyond, PoS, p. 30.

Nowak M.A., Hanke M., Trowbridge S.N., et al., 2011, ApJ 728, 13

Nowak M.A., Vaughan B.A., Wilms J., et al., 1999, ApJ 510, 874

Nowak M.A., Wilms J., Hanke M., et al., 2012, Workshop on Multifrequency Behaviour of

High Energy Cosmic Sources, Memorie della Societa Astronomica Italiana 83, 202

Nowak M.A., Wilms J., Heinz S., et al., 2005, ApJ 626, 1006

Oertel M., 2013, Diploma thesis, Universität Erlangen-Nürnberg

Oppenheimer J.R., Volkoff G.M., 1939, Phys. Rev. 55, 374

Orosz J.A., McClintock J.E., Aufdenberg J.P., et al., 2011, ApJ 742, 84

Oskinova L.M., Feldmeier A., Kretschmar P., 2012, MNRAS 421, 2820

Parsignault D.R., Epstein A., Grindlay J., et al., 1976, Ap&SS 42, 175

Petrucci P.O., Ferreira J., Henri G., et al., 2010, A&A 522, A38

Pirner S., 2009, Diploma thesis, Universität Erlangen-Nürnberg

Ponti G., Fender R.P., Begelman M.C., et al., 2012, MNRAS 422, L11

Pooley G.G., 2006, In: VI Microquasar Workshop: Microquasars and Beyond, PoS, p. 19-1.

Pooley G.G., 2011, ATel 3535

Pooley G.G., Fender R.P., Brocksopp C., 1999, MNRAS 302, L1

Popp A., 2011, Bachelor's thesis, Universität Erlangen-Nürnberg

Postnov K.A., Yungelson L.R., 2006, Living Reviews in Relativity 9, 6

Pottschmidt K., 2002, Ph.D. thesis, Universität Tübingen

Pottschmidt K., Wilms J., Nowak M.A., et al., 2000, A&A 357, L17

Pottschmidt K., Wilms J., Nowak M.A., et al., 2006, Advances in Space Research 38, 1350 Galactic and Extragalactic Astrophysics

Pottschmidt K., Wilms J., Nowak M.A., et al., 2003, A&A 407, 1039

Poutanen J., Vurm I., 2009, ApJ 690, L97

Poutanen J., Zdziarski A.A., Ibragimov A., 2008, MNRAS 389, 1427

Pravdo S.H., White N.E., Becker R.H., et al., 1980, ApJ 237, L71

Priedhorsky W.C., Terrell J., Holt S.S., 1983, ApJ 270, 233

Psaltis D., Norman C., 2000, arXiv:0001391

Rahoui F., Lee J.C., Heinz S., et al., 2011, ApJ 736, 63

Rappaport S., Zaumen W., Doxsey R., 1971, ApJ 168, L17+

Reid M.J., McClintock J.E., Narayan R., et al., 2011, ApJ 742, 83

Reig P., Kylafis N.D., Giannios D., 2003, A&A 403, L15

Remillard R.A., 2005, In: Chen P. (ed.) Texas@Stanford 2004. SLAC Electronic Conference Proceedings Archive, astro-ph/0504129

Remillard R.A., Canizares C.R., 1984, ApJ 278, 761

Roche É., 1849, Académie des sciences de Montpellier: Mémoires de la section des sciences 1, 243

Roche É., 1850, Académie des sciences de Montpellier: Mémoires de la section des sciences 1, 333

Roche É., 1851, Académie des sciences de Montpellier: Mémoires de la section des sciences 2, 21

Rodriguez J., Hannikainen D.C., Shaw S.E., et al., 2008a, ApJ 675, 1436

Rodriguez J., Shaw S.E., Hannikainen D.C., et al., 2008b, ApJ 675, 1449

Rothschild R.E., Blanco P.R., Gruber D.E., et al., 1998, ApJ 496, 538

Rushton A., Dhawan V., Fender R., et al., 2010a, ATel 2714

Rushton A., Evangelista Y., Paragi Z., et al., 2010b, ATel 2734

Rushton A., Miller-Jones J.C.A., Campana R., et al., 2012, MNRAS 419, 3194

Russell D.M., Gallo E., Fender R.P., 2013a, MNRAS 431, 405

Russell D.M., Lewis F., Munoz-Darias T., Kalemci E., 2013b, ATel 5084

Rybicki G.B., Lightman A.P., 1979, Radiative processes in astrophysics, New York, Wiley-Interscience

Sabatini S., Striani E., Verrecchia F., et al., 2010, ATel 2715

Scargle J.D., 1982, ApJ 263, 835

Shakura N.I., Sunyaev R.A., 1973, A&A 24, 337

Shapiro S.L., Teukolsky S.A., 1983, Black holes, white dwarfs, and neutron stars: The physics of compact objects, New York, Wiley-Interscience

Shaposhnikov N., Titarchuk L., 2006, ApJ 643, 1098

Skinner G.K., 1995, Experimental Astronomy 6, 1

Skinner G.K., 2004, New Astronomy Review 48, 205

Skipper C.J., McHardy I.M., Maccarone T.J., 2013, MNRAS

Soleri P., Muñoz-Darias T., Motta S., et al., 2013, MNRAS 429, 1244

Stirling A.M., Spencer R.E., de la Force C.J., et al., 2001, MNRAS 327, 1273

Strüder L., Briel U., Dennerl K., et al., 2001, A&A 365, L18

Suchy S., Pottschmidt K., Wilms J., et al., 2008, ApJ 675, 1487

Sugizaki M., Mihara T., Serino M., et al., 2011, PASJ 63, 635

Sundqvist J.O., Owocki S.P., 2013, MNRAS 428, 1837

Sundqvist J.O., Owocki S.P., Puls J., 2012, In: Drissen L., Rubert C., St-Louis N., Moffat A.F.J. (eds.) Proceedings of a Scientific Meeting in Honor of Anthony F. J. Moffat. Astronomical Society of the Pacific Conference Series, Vol. 465, p. 119

Tananbaum H., Gursky H., Kellogg E., et al., 1972, ApJ 177, L5

Tananbaum H., Kellogg E., Gursky H., et al., 1971, ApJ 165, L37

Tegmark M., 2007, Nat 448, 23

Thompson A., Attwood D., Gullikson E., et al., 2009, X-ray Data Booklet, Lawrence Berkeley National Laboratory, University of California, 3rd edition

Thompson A.R., Moran J.M., Swenson G.W., 2001, Interferometry and Synthesis in Radio Astronomy, 2nd Edition, Wiley, New York

Titarchuk L., 1994, ApJ 434, 570

Titarchuk L., Hua X.M., 1995, ApJ 452, 226

Titarchuk L., Lyubarskij Y., 1995, ApJ 450, 876

Tolman R.C., 1939, Phys. Rev. 55, 364

Tomida H., Tsunemi H., Kimura M., et al., 2011, PASJ 63, 397

Tomsick J.A., DelSanto M., Belloni T., 2012, ATel 4393

Torii S., Yamada S., Makishima K., et al., 2011, PASJ 63, 771

Trümper J.E., Hasinger G., 2008, The Universe in X-Rays, Springer Berlin Heidelberg

Trushkin S.A., Nizhelskij N.A., Zhekanis G.V., 2011, ATel 3546

Tsunemi H., Tomida H., Katayama H., et al., 2010, PASJ 62, 1371

Tudose V., Pooley G., Rushton A., et al., 2010, ATel 2755

Ubertini P., Lebrun F., Di Cocco G., et al., 2003, A&A 411, L131

Uttley P., Wilkinson T., Cassatella P., et al., 2011, MNRAS 414, L60

van der Klis M., 1989, In: Ögelman H., van den Heuvel E.P.J. (eds.) Timing Neutron Stars., p.27; Second, slightly updated version, May 1994

Vaughan B.A., Nowak M.A., 1997, ApJ 474, L43

Vedrenne G., Roques J.P., Schönfelder V., et al., 2003, A&A 411, L63

Veledina A., Poutanen J., Vurm I., 2013, MNRAS 430, 3196

Verner D.A., Ferland G.J., Korista K.T., Yakovlev D.G., 1996, ApJ 465, 487

von Kienlin A., Meegan C.A., Lichti G.G., et al., 2004, In: Hasinger G., Turner M.J.L. (eds.) UV and Gamma-Ray Space Telescope Systems. SPIE Conf. Ser. 5488, p.763

Vrtilek S.D., Boroson B.S., 2013, MNRAS 428, 3693

Walborn N.R., 1973, ApJ 179, L123

Wall J.V., Jenkins C.R., 2003, Practical Statistics for Astronomers, Cambridge Observing Handbooks for Research Astronomers, Vol. 3, Cambridge University Press

Westergaard N.J., Kretschmar P., Oxborrow C.A., et al., 2003, A&A 411, L257

Wilkinson T., Uttley P., 2009, MNRAS 397, 666

Wilms J., 2012a, Radiation Processes in Astrophysics, Lecture Notes at the Universität

Erlangen-Nürnberg

Wilms J., 2012b, X-ray Astronomy I, Lecture Notes at the Universität Erlangen-Nürnberg

Wilms J., Allen A., McCray R., 2000, ApJ 542, 914

Wilms J., Nowak M.A., Pottschmidt K., et al., 2006, A&A 447, 245

Wilms J., Pottschmidt K., Pooley G.G., et al., 2007, ApJ 663, L97

Wilson-Hodge C.A., Case G.L., 2010, ATel 2721

Wilson-Hodge C.A., Case G.L., Cherry M.L., et al., 2012, ApJS 201, 33

Wilson-Hodge C.A., Cherry M.L., Case G.L., et al., 2011, ApJ 727, L40

Winkler C., Courvoisier T.J.L., Di Cocco G., et al., 2003, A&A 411, L1

Wolter H., 1952, Ann. d. Phys. 10

Xiang J., Lee J.C., Nowak M.A., Wilms J., 2011, ApJ 738, 78

Zdziarski A.A., Lubiński P., Sikora M., 2012, MNRAS 423, 663

Zdziarski A.A., Pooley G.G., Skinner G.K., 2011a, MNRAS 412, 1985

Zdziarski A.A., Poutanen J., Paciesas W.S., Wen L., 2002, ApJ 578, 357

Zdziarski A.A., Skinner G.K., Pooley G.G., Lubiński P., 2011b, MNRAS 416, 1324

Zhang W., Jahoda K., Swank J.H., et al., 1995, ApJ 449, 930

Zhang W., Morgan E.H., Jahoda K., et al., 1996, ApJ 469, L29

Ziółkowski J., 2005, MNRAS 358, 851

Zschornack G., 2007, Handbook of X-ray Data, Springer Berlin Heidelberg

Acknowledgments

First of all: I would not be where I am now without my advisor, Jörn Wilms – thank you for being the best mentor I could imagine, for knowing when to push and when to leave things how they are, when just to listen, when to make suggestions and when to insist. Also: cats and half-dead squirrels, but I am more than thankful for that, too!

I gratefully acknowledge funding by the Bundesministerium für Wirtschaft und Technologie under Deutsches Zentrum für Luft- und Raumfahrt Grants 50 OR 1007 that made this PhD possible in the first place. I want to thank NASA's Goddard Space Flight Center, the MIT Kavli Institute for Astrophysics and Space Research, the Laboratoire AIM at CEA Saclay, and the European Space Astronomy Centre (ESAC) for their hospitality during the time when the research presented here was done, as well as the Faculty of the European Space Astronomy Centre (ESAC) for financial support. Special thank to the ARIADNE-Mentoring Programme and Prof. Dr. Gisela Anton.

This research has made use of the MAXI data provided by RIKEN, JAXA and the MAXI team and Fermi GBM Earth occultation results provided by the Fermi GBM Earth occultation Guest Investigation teams at NASA/MSFC and LSU.

This work would have been much harder and in parts impossible if not for the parallel computing routines with ISIS developed and implemented at the Remeis cluster by Thomas Dauser and Fritz Schwarz. All original figures in this work were prepared with the `slxfig` of John E. Davis'.

This research would not have happened without my wonderful collaborators and friends, quite often both in the same person. I want to thank you all!

Katja Pottschmidt – for the counsel, for housing me, for having answers to all my scientific question, for the wonderful conversations, for making me feel like I belong. Jérôme Rodriguez – for the wonderful science and for always making me feel like a collaborator, not a student. Natalie Hell – for understanding and the moral support and overall for never ever stopping making fun of me. Matthias Kühnel and Sebastian Müeller – for your great ideas and for always being there when I need help and for all the laughter. Marion Cadolle Bel – for the great invitation to ESAC. Ingo Kreykenbohm – for always being there for all my little and big computer problems and for great conversations we had. The black hole telecon gang (not yet mentioned by name: Arash Bodaghee, John A. Tomsick, Anne Lohfink, Refiz Duro, Ivica Miškovičová) – for your input and for the wonderful discussions. My office mates – for all the fun times we had and for bearing with me and Eugenia especially for taking over my duties around the coffee machine. Slawomir Suchy – for the phone calls which never failed to cheer me up and for the invitation to Tübingen. Mike Nowak – for the ego-push at the Bamberg conference and, together with Sera Markoff, for making my future happen. Wiebke Eikmann, Alexander Popp, and Macarena Sagredo – for helping me out with some of the uglier aspects of INTEGRAL. Fritz Schwarm – not only for torque (which rocks!), but also for the great

conversations. Felix – for saving me a lot of tex-worries. Guy Pooley – for the radio data. Lisa Zimmermann – for the great project and for the invitation to MPIfR. Diana Marcu – for the great time at GSFC. Philippe Laurent – for giving me a chance to be involved in the INTEGRAL polarization studies. Rick Rothschild – for hosting me in his group in San Diego and his scientific input in my work. Peter Kretschmar – for encouragement and great photos. Daniela Huppenkothen – for the amazing summer academy (let's do it again in a few years!).

And last, but absolutely not least and without any explanation because there not even the smallest chance to put your contribution into words: Flo.

Thank you.